# ABSTRACT

HOLMES, JESSE CURTIS. Monte Carlo Calculation of Thermal Neutron Inelastic Scattering Cross Section Uncertainties by Sampling Perturbed Phonon Spectra. (Under the direction of Dr. Ayman I. Hawari.)

Nuclear data libraries provide fundamental reaction information required by nuclear system simulation codes. The inclusion of data covariances in these libraries allows the user to assess uncertainties in system response parameters as a function of uncertainties in the nuclear data. Formats and procedures are currently established for representing covariances for various types of reaction data in ENDF libraries. This covariance data is typically generated utilizing experimental measurements and empirical models, consistent with the method of parent data production. However, ENDF File 7 thermal neutron scattering library data is, by convention, produced theoretically through fundamental scattering physics model calculations. Currently, there is no published covariance data for ENDF File 7 thermal libraries. Furthermore, no accepted methodology exists for quantifying or representing uncertainty information associated with this thermal library data.

The quality of thermal neutron inelastic scattering cross section data can be of high importance in reactor analysis and criticality safety applications. These cross sections depend on the material's structure and dynamics. The double-differential scattering law, $S(\alpha,\beta)$, tabulated in ENDF File 7 libraries contains this information. For crystalline solids, $S(\alpha,\beta)$ is primarily a function of the material's phonon density of states (DOS). Published ENDF File 7 libraries are commonly produced by calculation and processing codes, such as the LEAPR module of NJOY, which utilize the phonon DOS as the fundamental input for inelastic scattering calculations to directly output an $S(\alpha,\beta)$ matrix. To determine

covariances for the $S(\alpha,\beta)$ data generated by this process, information about uncertainties in the DOS is required.

The phonon DOS may be viewed as a probability density function of atomic vibrational energy states that exist in a material. Probable variation in the shape of this spectrum may be established that depends on uncertainties in the physics models and methodology employed to produce the DOS. Through Monte Carlo sampling of perturbations from the reference phonon spectrum, an $S(\alpha,\beta)$ covariance matrix may be generated. In this work, density functional theory and lattice dynamics in the harmonic approximation are used to calculate the phonon DOS for hexagonal crystalline graphite. This form of graphite is used as an example material for the purpose of demonstrating procedures for analyzing, calculating and processing thermal neutron inelastic scattering uncertainty information.

Several sources of uncertainty in thermal neutron inelastic scattering calculations are examined, including sources which cannot be directly characterized through a description of the phonon DOS uncertainty, and their impacts are evaluated. Covariances for hexagonal crystalline graphite $S(\alpha,\beta)$ data are quantified by coupling the standard methodology of LEAPR with a Monte Carlo sampling process. The mechanics of efficiently representing and processing this covariance information is also examined.

Finally, with appropriate sensitivity information, it is shown that an $S(\alpha,\beta)$ covariance matrix can be propagated to generate covariance data for integrated cross sections, secondary energy distributions, and coupled energy-angle distributions. This approach enables a complete description of thermal neutron inelastic scattering cross section uncertainties which may be employed to improve the simulation of nuclear systems.

# Monte Carlo Calculation of Thermal Neutron Inelastic Scattering Cross Section Uncertainties by Sampling Perturbed Phonon Spectra

by
Jesse Curtis Holmes

A dissertation submitted to the Graduate Faculty of
North Carolina State University
in partial fulfillment of the
requirements for the Degree of
Doctor of Philosophy

Nuclear Engineering

Raleigh, North Carolina

2014

APPROVED BY:

Dr. Ayman I. Hawari
Committee Chair

Dr. Paul R. Huffman

Dr. John K. Mattingly

Dr. Bernard W. Wehring

Dr. Michael L. Zerkle

# BIOGRAPHY

Jesse Holmes was born in 1977 near Blytheville, Arkansas. His parents are James and Andrea Holmes, and he has a younger brother, Wesley. Jesse and his wife, Becky, have two daughters, Lydia and Zyra.

Jesse moved many times throughout several states growing up. He graduated from Fayetteville High School in 1995 in Fayetteville, Arkansas. In 1998, Jesse joined the U.S. Navy and entered into the Naval Nuclear Propulsion Program as a nuclear reactor operator trainee. Jesse then completed nearly two years of nuclear power school and training to qualify as a nuclear reactor operator and electronics technician. In 2000, he was assigned to the aircraft carrier USS Harry S. Truman (CVN-75) based in Norfolk, Virginia, where he was responsible for the direct operation of the ship's nuclear reactors and maintenance of nuclear electronics systems. During his more than four years serving onboard the Truman, Jesse spent a combined total of about 24 months at sea (including two six-month overseas deployments), participated in combat operations, and had the opportunity to visit 11 foreign countries. In 2004, Jesse was transferred to Charleston, South Carolina, to serve for three years as an instructor at the Navy's Nuclear Power Training Unit. While living in the Charleston area, Jesse met his wife, Becky. They married in 2006. Jesse also completed his Associate of Science degree in 2007 at Trident Technical College in Charleston. After almost ten years of service, Jesse left the Navy in 2007 to further pursue his college education.

In 2007, Jesse and his wife moved to Raleigh, North Carolina, where Jesse enrolled as an undergraduate at North Carolina State University. He completed his Bachelor of Science in Nuclear Engineering and Bachelor of Arts in Physics in 2010. He also qualified as a licensed nuclear reactor operator at North Carolina State University's PULSTAR research reactor. In the summer of 2010, Jesse interned at Oak Ridge National Laboratory in Oak Ridge, Tennessee, in the Nuclear Data and Criticality Safety Group and began working in the field of thermal neutron scattering. Continuing as a nuclear engineering graduate student at North Carolina State University under the advisement of Dr. Ayman Hawari, Jesse was a recipient of two Department of Energy research fellowships – the Nuclear Energy University Programs Fellowship and the Rickover Fellowship in Nuclear Engineering. He completed his Master of Nuclear Engineering degree in 2011 and Ph.D. in Nuclear Engineering in 2014. Upon receiving his Ph.D., Jesse accepted a position as a senior nuclear engineer at Bettis Atomic Power Laboratory near Pittsburgh, Pennsylvania. Bettis Atomic Power Laboratory conducts reactor plant research and design for the Naval Nuclear Propulsion Program.

# ACKNOWLEDGMENTS

I would first like to thank Dr. Hawari for convincing me to get my Ph.D. against my determined insistence that I had no intention of continuing beyond a master's degree. Through these past few years, Dr. Hawari has provided insightful technical, scientific and philosophical guidance that has served me well and that I will carry with me professionally and personally. He has broadened my view of science, motivated me to set my sights high, and helped set me on the path where I am today. It has been a rewarding experience having Dr. Hawari as my graduate advisor.

I am honored to have been supported by two U.S. Department of Energy research fellowships throughout my graduate career. I was a Nuclear Energy University Programs Fellow sponsored by the Office of Nuclear Energy from 2010 – 2013, and I have been a Rickover Fellow sponsored by the Division of Naval Reactors from 2013 to the present. My fellowship tenures have provided invaluable academic and financial support and have undoubtedly opened professional opportunities for me.

I want to thank Dr. Paul Huffman, Dr. John Mattingly, Dr. Bernard Wehring and Dr. Michael Zerkle for dedicating their time to review my dissertation and to serve as members of my committee. Dr. Zerkle has also served as my advisor under the Rickover Fellowship Program. He has provided helpful support and guidance in the final stages of my graduate career and in my transition to a professional career with Bettis Atomic Power Laboratory.

Without the support of my wife Becky, I would never have made it this far. She has been patient, encouraging, appreciative and loving. During the countless days, evenings, nights and weekends I spent practically living at my office, she had the much more challenging task of managing our two wonderful but very “spirited” daughters. Now, untold gallons of coffee later (for both of us), we finally made it through!

# TABLE OF CONTENTS

# LIST OF TABLES

# LIST OF FIGURES

# Chapter 1

# Introduction and Historical Perspective

## 1.1 The ENDF Nuclear Data Library

The modeling and simulation of nuclear systems requires the input of large quantities of nuclear data to provide information about reactions that take place between transported particles and the material nuclides present. This reaction information is energy dependent and can include reaction cross sections, resonance parameters, fission neutron multiplicities, particle emission distributions in energy and angle, as well as other data. The process of analyzing experimentally measured reaction data and nuclear model predictions together to assemble a specific set of best-known values refers to the production of an evaluated nuclear data set, or an evaluation. The need to prepare formatted libraries of evaluated nuclear data that could be processed by modeling and simulation codes was recognized early in the nuclear age. By 1963, there were many detailed libraries available in different formats developed by various laboratories around the world for their own use. However, it was known that these libraries could produce different results in reactor calculations. The Evaluated Nuclear Data File (ENDF) format was introduced at Brookhaven National Laboratory in 1964 in response to the need for a flexible link between processing codes and data libraries of different formats. The first version, ENDF/A, served as a standard format repository for evaluated data libraries from different laboratories, facilitating the comparison of reactor calculations on a common basis [1].

The United States Atomic Energy Commission formed the Cross Section Evaluation Working Group (CSEWG) in 1966 to address concerns about standardization in the production and processing of evaluated neutron cross section data sets for reactor calculations [2]. CSEWG would undertake development of a new ENDF/B format. In contrast with the multiple (and sometimes fragmentary) evaluated data sets of ENDF/A, this new format would provide a single complete evaluated data library for each chemical element and/or isotope of interest [3]. ENDF/B contained a much more rigid structure, was more mathematically rigorous [1], and quickly gained widespread international use. Although other nuclear data library formats exist, the ENDF/B format is currently the predominant format used both in the United States and internationally [4]. It is the only format that is considered in this work.

The ENDF project is managed by the National Nuclear Data Center at Brookhaven National Laboratory. Over time, the responsibilities of CSEWG expanded to include development of automated methods for processing ENDF library data and maintenance of the ENDF project. In particular, CSEWG is now responsible for proposing, reviewing and approving new ENDF data formats and procedures [3]. Several ENDF releases have been published over the project's history, and many data types beyond neutron reaction data have been added. The current release, ENDF/B-VII.1, was published in December 2011. The major release number, or version number for ENDF/B, is given by the Roman numeral "VII". The minor release number, also known simply as the release number, is given by the extension ".1", and it follows the initial ".0" release. It is also important to note that

ENDF/B-VII is in the ENDF-6 format which is defined by Ref. [1]. This is the format of ENDF/B that is incorporated in this work.

ENDF libraries are divided into data blocks, or files, given by an MF number. Each file is associated with a particular data type. For example, MF = 1 contains library documentation, MF = 2 contains resonance parameters, MF = 3 contains reaction cross sections, etc. The MF blocks are further subdivided into MT sections which, in general, contain data for specific reaction types. The major focus of this work is on thermal neutron inelastic scattering law data associated with MF = 7 (thermal neutron scattering data), MT = 4 (incoherent inelastic scattering) [1]. Details of the format for ENDF File 7, MT = 4, are provided in Appendix A.

## 1.2 ENDF Nuclear Data Covariances

It has long been understood that nuclear data uncertainties can contribute significantly to uncertainties in most neutronics calculations. In the early versions of ENDF/B, evaluators of nuclear data sets provided uncertainty information, as available, through in-file documentation. However, there were inconsistencies in the reporting methodologies and there was no convenient way to provide data correlations (or covariances). During the development process for ENDF/B-IV, it was proposed by CSEWG to incorporate a format providing covariance information in separate covariance files associated with the parent data files. These would be numbered File 3x, where ‘x’ is the MF for the parent file. For example, File 32 provides covariance information for the resonance parameter data given in File 2.

Several factors led to the decision to add covariance data files to ENDF/B-IV [5]. Evaluated nuclear data is commonly produced using empirical nuclear models with parameters that are fitted to experimental measurements. This process, using a least-squares approach, generates library data with covariances that depend on both the nuclear model and uncertainty information for the measurements. It is also common to generate adjusted cross section libraries, where the adjusted cross sections provide a best fit to the original evaluated cross sections and new experimental integral measurements. When differential measurements are available, these often have high uncertainties compared to integral measurements. In this case, uncertainty information for the differential measurements carries little weight in determining covariances for the integral cross sections [6]. As a result of the fitting procedure, the off-diagonal elements of the generated covariance matrix are often a dominant feature in the quantification of nuclear data uncertainties, and they must be considered in any forward uncertainty propagation calculations. Additionally, it is often the case that the calculation of uncertainties in quantities of interest requires cross section uncertainty information to be processed together with differential data and, when available, its uncertainty information. This could not be easily carried out without standardized library formats tabulating the covariance data associated with each data type.

Early sensitivity and uncertainty analysis work largely considered only integrated cross section uncertainties to be significant and deemphasized or ignored uncertainties in the emission spectra of secondary particles [7]. However, the great majority of tabulated data in published libraries is generally associated with secondary distribution information. In such cases, any uncertainty analysis which does not consider uncertainties in the secondary distribution data is incomplete [8].

Consideration of secondary particle distribution data covariances has been found to be particularly valuable in fusion reactor design, where it is critical that the accuracy of neutron transport calculations be well known. Files 34 and 35 tabulate covariances for angular distributions and energy distributions of secondary particles, respectively. A File 36 format is proposed to tabulate coupled energy-angle distributions of secondary particles [9]. Still, very little published covariance data for secondary distributions exists today, and few sensitivity and uncertainty analysis codes are capable of processing multi-dimensional covariances. The SENSIT-2D code [10] was designed to process uncertainty information for both cross section and secondary distribution data for use with the TRIDENT-CTR transport code [11]. Both of these codes were developed specifically for fusion reactor analysis. The TSUNAMI module of the SCALE transport code is one of the most widely used sensitivity and uncertainty analysis codes for fission reactor and criticality safety applications today, and it does not have the capability to treat secondary distribution data uncertainties [12].

The production of large detailed sets of evaluated nuclear data is an expensive endeavor and should be justified by real benefits to the applications of end users. One fundamental obstacle in providing detailed covariance data is that, in principle, the number of entries in the covariance matrix is equal to the square of the number of evaluated data points. This can result in massive storage requirements. This concern is greatly amplified when considering covariances for secondary distributions in energy and angle. As a result, much of the history of calculating and representing covariance data has focused on the need to optimize the resolution of covariances necessary for a desired quality of specific end-use calculations. This makes it difficult for the traditional evaluation of covariance data to be application-independent [7].

One method commonly employed to reduce the quantity of covariance data is to overlay a coarse multigroup energy bin structure to the problem. This principle is utilized in File 35 and in the proposed File 36. Up to now, almost all published ENDF covariance data focuses on events in the resolved and unresolved resonance energy regions. Bin structure has the highest resolution in the resonance regions. For energies below this (such as in the thermal energy range), a single broad energy bin is used. Only bin-to-bin covariance data is provided. All within-bin data is assumed to be perfectly correlated. This representation precludes the user from re-binning the covariance information to match a finer multigroup structure because the required within-bin covariances are not provided. Covariance data associated with each bin is already integrated over energy and angle (or over angle in the case of energy distribution data), and this differential information cannot be extracted [7]. As an example, Figure 1.1 displays the published ENDF/B-VII total cross section correlation matrix for natural carbon. Figures 1.2 and 1.3 display plots of the associated total cross section and the relative uncertainty in the total cross section for natural carbon, respectively [13].

An alternative method of representing very large quantities of covariance data associated with secondary distributions is provided by ENDF File 30, which is a general format describing data covariances obtained from parameter covariances and sensitivities. The use of File 30 is ideal for evaluated data produced entirely by nuclear model codes when

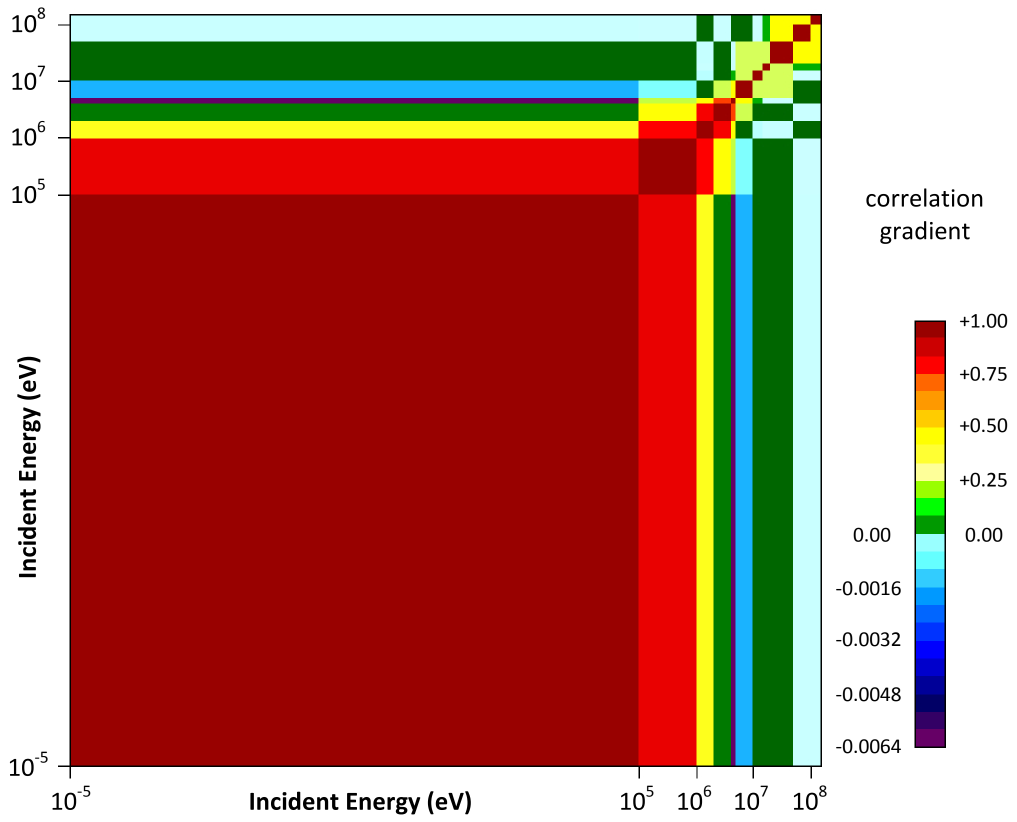

**Figure 1.1 ENDF/B-VII total cross section correlation matrix for natural carbon [13].**

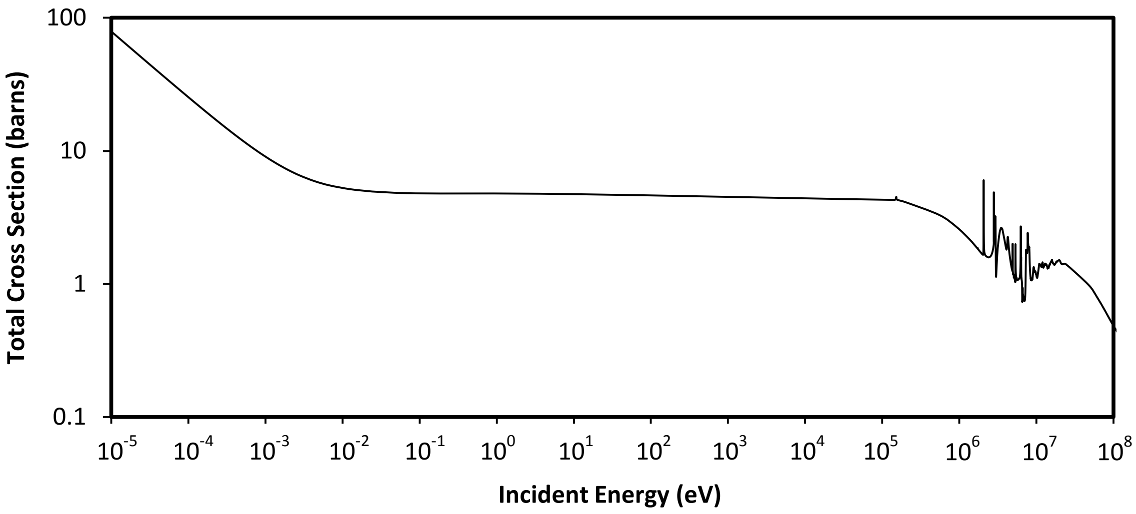

**Figure 1.2 ENDF/B-VII total cross section for natural carbon [13].**

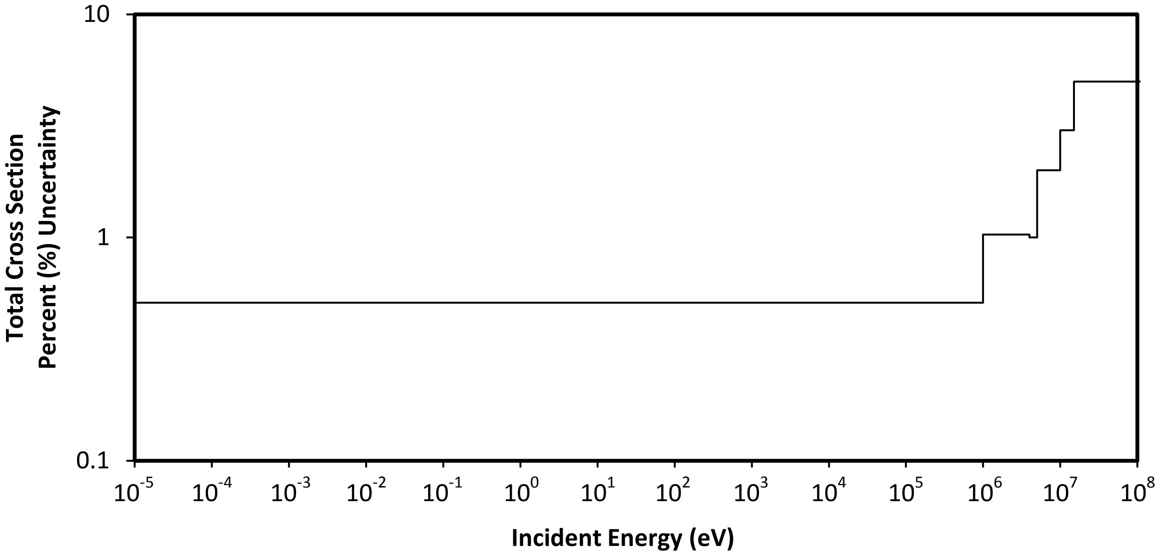

**Figure 1.3 ENDF/B-VII total cross section uncertainty for natural carbon [13].**

covariances among the model parameters are well defined. This is exactly the case for the majority of emission data in the unresolved resonance energy region where the emission spectra are the most complicated and experimental data may be limited. The great advantage of the parameter-based File 30 format is the ability to provide emission covariance data in a highly compact form that allows much finer resolution. Section 3.1.3 provides the mathematical basis for the File 30 format. For further details, see Ref. [1].

ENDF File 7, also known as a thermal library, contains double-differential thermal neutron inelastic scattering data associated with the bound structure and dynamics of a material. Elastic scattering data is also tabulated. Typically, thermal scattering data in File 7 is tabulated for incident energies ≤ 5 eV. Since thermal elastic scattering is generally not of great importance in reactor analysis and criticality safety applications, this work considers only thermal inelastic scattering. Most nuclear data libraries are nuclide specific, not material specific, and do not contain any File 7 information. Thermal neutron scattering is simply treated in the free-gas approximation in these situations. For the material-based thermal libraries that do exist, no covariance information has yet been published, and no File 37 format has been proposed.

The availability of structure-based thermal libraries in neutronics codes can be highly important in accurately simulating systems with a significant thermal neutron flux. This importance can be especially great for heterogeneous systems and systems with significant temperature gradients. Dynamic structure may impose a considerable modification to the free-gas scattering cross section and produces inelastically scattered neutron distributions coupled in energy and angle that are specific to the excitation modes present in the molecular structure. These effects are also temperature dependent. The emission spectra for secondary neutrons can play a significant role in the calculation of system response parameters for thermal systems. As such, it is expected that uncertainty information for both integrated cross sections and differential cross sections in energy could have a tangible impact on the calculation of response parameter uncertainties in thermal systems. Reviewing Figures 1.1 and 1.3, it is clear that no consideration is given to thermal scattering physics in the traditional calculation of covariances and uncertainties. Indeed, one of the recommendations given to CSEWG in the International Atomic Energy Agency Technical Meeting on Neutron Cross-Section Covariances in 2010 was, specifically, to develop the ability to provide covariances for the thermal scattering law data in ENDF File 7 [14].

ENDF File 7 thermal libraries are traditionally produced entirely from fundamental scattering physics model calculations without adjustment or fitting to experimental data. In particular, double-differential measurements often do not exist or are very limited in scope. In a sense, these thermal libraries are not "evaluated" libraries but are theoretical libraries, although the label "evaluator" is traditionally retained for the author. This purely theoretical approach is considered acceptable because the theory of thermal neutron scattering is well understood, not dependent upon empirical modeling, and theoretical calculations have been demonstrated to be consistent with experimental results for many materials. In any case, the character of this type of double-differential data demands a careful uncertainty analysis that will necessarily differ from historical methodologies.

The theme of this work is to investigate the sources of uncertainty present in the theoretical calculation of ENDF File 7 double-differential thermal neutron inelastic scattering data, develop a mathematical framework to describe these uncertainties, and demonstrate the ability to produce a representative covariance matrix for the double-differential data. Finally, procedures for propagating this covariance information to produce covariance and uncertainty information for differential and integrated cross sections are demonstrated.

# Chapter 2

# Thermal Neutron Inelastic Scattering Theory

## 2.1 Development of Thermal Neutron Scattering Theory

Neutron scattering cross sections at thermal energies are a function of both nuclear cross sections and a material's molecular structure. The energy below which the cross sections become appreciably sensitive to molecular structure is on the order of 1 eV to 10 eV. For thermal neutrons below this threshold, the de Broglie wavelengths will be on the order of the interatomic spacing in the material and neutrons may scatter with an aggregate of atoms instead of only with individual nuclei. Thermal neutron energies will also be on the same order as the available excitation modes that exist in a material's molecular structure. These can include vibrational, translational and rotational (or spin) modes. The vibrational modes, known as phonons, are typically of chief concern for thermal neutron scattering in solids.

Neutron energy transfer in the thermal energy region is distinct from the processes at higher energies. When neutrons with kinetic energy less than interatomic bonding energy scatter, the free translation of individual nuclei does not occur. During the neutron scattering process at thermal energies, nuclear excitations are not possible for most isotopes. However, potential scattering will be accompanied by interactions with excitation modes in the material structure. These interactions will be a function of material temperature. For most solid crystals, the discrete creation or annihilation of one or more phonons is the only consequential mechanism for energy exchange. The phonon density of states (DOS) is a dynamic property of the material structure and is typically the fundamental input in thermal neutron inelastic scattering cross section calculations. Scattering may also occur elastically, with effectively no energy transfer. Both inelastic and elastic scattering can take place incoherently or coherently. Consequently, secondary thermal neutron emission spectra have complex structure coupled in energy and angle. This can result in significant modification to integrated scattering cross sections compared to a free-gas model.

A phonon may be conceptualized as a coordinated wave of atomic vibrations in reciprocal space. Figure 2.1 gives a graphical representation of a transverse phonon wave. The phonon wave vector $\boldsymbol{q}$ is always in the direction of propagation of the wave. Three orthogonal polarization vectors $\boldsymbol{e}_j$, defined based on crystal symmetry, are associated with the components of atomic vibrations parallel to each $\boldsymbol{e}_j$. Each phonon mode $\boldsymbol{q}_m$ will have a frequency $\omega$ and polarization $j$ associated with it, where the subscript $m$ represents a specific $\omega$ and $j$. This relationship is defined by the dispersion relations $\omega(\boldsymbol{q})$ for the crystal.

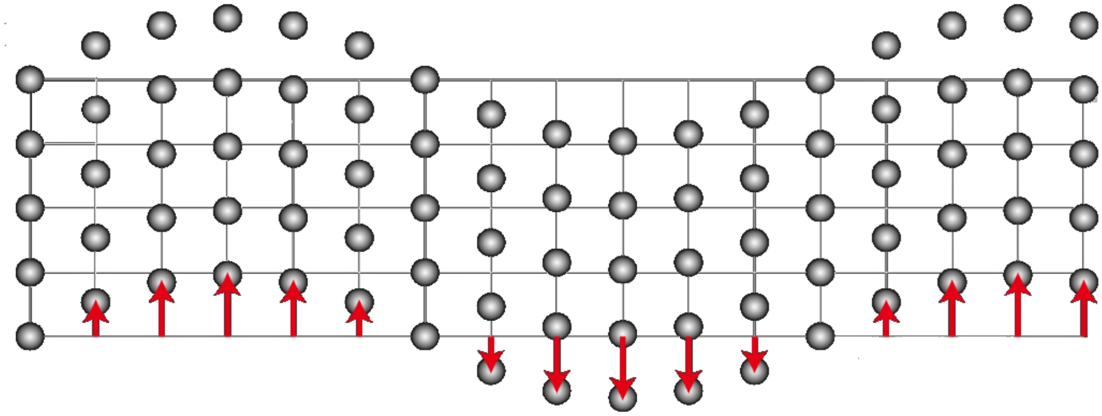

**Figure 2.1 Graphical representation of a transverse phonon wave among atoms in reciprocal space. A transverse phonon wave has perpendicular propagation and polarization directions. Longitudinal phonon waves have parallel propagation and polarization directions.**

The terms “phonon frequency” and “phonon energy” will often be used interchangeably based on the relationship $E = \hbar\omega$. Both terms are common in literature. For clarity, it is pointed out that “frequency” in this context refers to the angular frequency of the phonon wave vector in reciprocal space and not the classical (or mechanical) oscillation frequency of an atom in real space, although they are related. Likewise, “energy” in this context refers to the total energy stored in the crystal that is associated with the phonon mode and not the energy state of an individual atom.

The double-differential thermal neutron scattering cross section may be written as

$$\frac{d^2\sigma(E)}{d\Omega dE'} = \frac{1}{4\pi}\left(\frac{k'}{k}\right)\left[\sigma_{\mathrm{coh}}S(\boldsymbol{Q},\omega) + \sigma_{\mathrm{incoh}}S_s(\boldsymbol{Q},\omega)\right] \tag{2.1}$$

using the first-order Born approximation and Fermi pseudopotential [15]. The Born approximation in this context is the assumption that, in a neutron scattering process, the total scattering wave function of the system is nearly equivalent to the plane wave of the incident neutron, or that scattering is weak. Since the scattering lengths of nuclei are orders of magnitude less than interatomic distances, this assumption is nearly always valid. The Fermi pseudopotential treats the nuclear scattering potential as a δ-function about the nucleus, consistent with the pointlike nature of the nucleus with respect to thermal neutron wavelengths. With the Born approximation, it produces the required isotropic scattering about a fixed nucleus [16]. In Eq. (2.1),

$$\boldsymbol{Q} = \boldsymbol{k} - \boldsymbol{k}' \tag{2.2}$$

is the neutron scattering vector, where $\boldsymbol{k}$ and $\boldsymbol{k}'$ are the incident and scattered neutron wave vectors, respectively. The quantity $\hbar(\boldsymbol{k} - \boldsymbol{k}')$ represents the momentum transferred by the neutron to the scattering system, where $\hbar$ is the reduced Planck constant. The terms $E$ and $E'$ denote the incident and scattered neutron energy, respectively. Therefore,

$$\omega = \left(E - E'\right) / \hbar \tag{2.3}$$

represents, in terms of the change in angular frequency of the neutron wave vector, the energy transferred by the neutron to the scattering system. The coherent and incoherent nuclear cross sections are given by $\sigma_{\mathrm{coh}}$ and $\sigma_{\mathrm{incoh}}$, respectively. The term $S(\boldsymbol{Q},\omega)$ is known as the dynamic structure factor. It has units of inverse energy and consists of a self component and a distinct component, or

$$S(\boldsymbol{Q},\omega) = S_{\mathrm{s}}(\boldsymbol{Q},\omega) + S_{\mathrm{d}}(\boldsymbol{Q},\omega). \tag{2.4}$$

The dynamic structure factor contains information about correlations in the positions of the same nucleus ($S_{\mathrm{s}}$) and distinct nuclei ($S_{\mathrm{d}}$) vs. time. Only the latter gives rise to interference effects. These correlations describe atomic motions that are a function of the interatomic forces present in the material structure.

In most criticality safety and reactor applications, the scattering material has randomly oriented microcrystal structure. That is, there will generally not be large oriented crystals present. For these applications, the orientation-averaged dynamic structure factor

$$S(Q,\omega) = S_{\mathrm{s}}(Q,\omega) + S_{\mathrm{d}}(Q,\omega) \tag{2.5}$$

is of interest. For $k_{\mathrm{B}}T \ll \hbar\omega_{\mathrm{max}}$, where $k_{\mathrm{B}}$ is Boltzmann's constant, $T$ is temperature and $\omega_{\mathrm{max}}$ is the maximum frequency of the phonon DOS, it is generally a very good approximation that the thermal displacements of atoms from their equilibrium positions are small and that interatomic forces may be considered harmonic [17]. In this case, the $S_{\mathrm{s}}$ and $S_{\mathrm{d}}$ terms can be expanded in terms of phonon order as

$$S_{\mathrm{s}} = {}^{0}S_{\mathrm{s}} + {}^{1}S_{\mathrm{s}} + {}^{2}S_{\mathrm{s}} + \cdots \text{ and } S_{\mathrm{d}} = {}^{0}S_{\mathrm{d}} + {}^{1}S_{\mathrm{d}} + {}^{2}S_{\mathrm{d}} + \cdots . \tag{2.6}$$

The superscripts designate the number of phonons excited or deexcited. The zero-phonon terms are associated with elastic scattering and all other terms account for inelastic scattering [18]. Henceforth, $S(Q,\omega)$ will be defined to be associated with only inelastic scattering, and the zero-phonon terms (which may be treated separately) will be dropped.

For an interaction between a neutron and more than one phonon, combinations of phonons can almost always be found such that their wave vectors and frequencies satisfy conservation of momentum and energy. There are essentially no interference effects in this situation, and the distinct multiphonon terms of Eq. (2.6) can be considered to be zero [15]. The exact one-phonon dynamic structure factor, ${}^{1}S(Q,\omega) = {}^{1}S_{\mathrm{s}} + {}^{1}S_{\mathrm{d}}$, can be calculated from the dispersion relations $\omega(\boldsymbol{q})$ [19] or by other methods. The ${}^{1}S_{\mathrm{d}}$ term can be conceptualized as the interference-induced modification to $S_{\mathrm{s}}$, where $S_{\mathrm{s}}$ represents the value the dynamic structure factor would have if all scattering were incoherent. The terms of $S_{\mathrm{s}}$ are always positive or zero, while the ${}^{1}S_{\mathrm{d}}$ term may be positive, negative or zero. Both ${}^{1}S_{\mathrm{s}}$ and ${}^{1}S_{\mathrm{d}}$ will be zero for $\omega$ greater than $\omega_{\mathrm{max}}$. In cases where coherent interference from crystal structure prohibits one-phonon scattering for a particular $Q$ and $\omega$ combination, then ${}^{1}S_{\mathrm{d}} = -\,{}^{1}S_{\mathrm{s}}$. The value of ${}^{1}S_{\mathrm{d}}$ can vary significantly over the range of $Q$ and $\omega$. However, for most reactor analysis and criticality safety applications, the scattering distributions of thermal neutrons in energy are of much more concern than the distributions in angle. In general, the magnitude of ${}^{1}S_{\mathrm{d}}$ will be small compared to $\sum_{n}({}^{n}S_{\mathrm{s}})$ when each is averaged over all scattering angles (or over the corresponding ranges of $Q$). In particular, the contribution of $^1S_\mathrm{d}$ to the integrated scattering cross section is generally negligible in many materials at temperatures of concern. If the above generalizations apply, the impact of coherent interference in inelastic scattering may be neglected entirely, yielding

$$S(Q,\omega) \approx S_\mathrm{s}(Q,\omega). \tag{2.7}$$

Eq. (2.7) is known as the *incoherent approximation*, and it allows Eq. (2.1) to be rewritten as

$$\frac{d^2\sigma(E)}{d\Omega dE'} = \frac{\sigma_\mathrm{b}}{4\pi}\left(\frac{k'}{k}\right) S_\mathrm{s}(Q,\omega), \tag{2.8}$$

where the bound nuclear cross section is given by

$$\sigma_\mathrm{b} = \sigma_\mathrm{coh} + \sigma_\mathrm{incoh}. \tag{2.9}$$

Incorporating the incoherent approximation is a common practice in the theoretical calculation of thermal neutron scattering kernels. It is physically valid in many nuclear engineering applications and it allows the calculation of cross sections to proceed analytically with ease. Cases where coherent interference in inelastic scattering is not negligible, such as for graphite, will be discussed separately in Sections 3.7.4 and 4.1.

Scattering in a Bravais crystal with one atom per unit cell will be considered. Recall that, under the harmonic approximation, $S_\mathrm{s}(Q,\omega)$ may be expanded into terms corresponding to inelastic scattering with $n = 1, 2, \ldots$ phonon(s) such that

$$S_\mathrm{s}(Q,\omega) = \sum_{n=1}^{\infty}[^nS_\mathrm{s}(Q,\omega)]. \tag{2.10}$$

In this case, the one-phonon term may be expressed in the form

$$^1S_\mathrm{s}(Q,\omega) = \frac{e^{-2W}Q^2\rho(\omega)\left[\coth\left(\frac{\hbar|\omega|}{2k_\mathrm{B}T}\right) \pm 1\right]}{4M|\omega|}, \tag{2.11}$$

where $\rho(\omega)$ is the normalized phonon DOS for the scattering nuclide and $M$ is the mass of the nuclide. The DOS is considered to be an even function. The ± corresponds to phonon emission (+) or absorption (–). The term $e^{-2W}$ is the Debye-Waller factor and is a function of the mean square displacement of the atom. For phonons with frequency $\omega$, the value $\frac{1}{2}\left[\coth\left(\frac{\hbar\omega}{2k_{\mathrm{B}}T}\right)-1\right]$ is the thermal average of the phonon occupation number. The only potential dependence of $S_{\mathrm{s}}(\boldsymbol{Q},\omega)$ on the direction of $\boldsymbol{Q}$ lies in the anisotropy of the Debye-Waller factor due to the directional distribution of atomic vibrations. For a cubic crystal, the partial phonon DOS for any three orthogonal vectors is equivalent, $S_{\mathrm{s}}(\boldsymbol{Q},\omega)=S_{\mathrm{s}}(Q,\omega)$ and $2W$ is expressed as

$$2W=\frac{\hbar Q^2}{2M}\int_0^\infty \frac{\coth\left(\frac{\hbar\omega}{2k_{\mathrm{B}}T}\right)\rho(\omega)}{\omega}\,d\omega. \tag{2.12}$$

Assuming randomly oriented microcrystal structure, the partial phonon DOS will be the same for any chosen vector when averaged over all crystal orientations, regardless of the crystal lattice. Therefore, under this condition, the form of Eq. (2.12) can be safely applied even for non-cubic lattices. Regarding Eqs. (2.11) and (2.12), the Debye-Waller factor is considered an isotropic function of the total phonon DOS only [15].

## 2.2 The $S(\alpha,\beta)$ Thermal Scattering Law

The ENDF File 7 thermal library format tabulates inelastic double-differential cross section information in terms of the thermal scattering law, $S(\alpha,\beta)$ [1]. Although the term “thermal scattering law” may be generalized to include both elastic and inelastic scattering, the inelastic definition will be observed. The thermal scattering law is a function of the dimensionless momentum and energy transfer factors $\alpha$ and $\beta$, respectively. Essentially, the thermal scattering law is an alternative representation of the $S(\boldsymbol{Q},\omega)$ dynamic structure factor for the case of randomly oriented microcrystal structure. See Appendix A for a detailed description of the ENDF File 7, MT = 4, format for tabulating the thermal scattering law.

Eqs. (2.11) and (2.12) can be rewritten in terms of $\alpha$ and $\beta$ as

$$^{1}S_{\mathrm{s}}(Q,\omega) = (k_{\mathrm{B}}T)^{-1}S_1(\alpha,\beta), \tag{2.13}$$

where

$$S_1(\alpha,\beta) = \frac{\alpha\, e^{-\alpha\lambda}e^{-\beta/2}\rho(\beta)}{2\beta\,\sinh(\beta/2)}, \tag{2.14}$$

and

$$2W = \alpha \times \lambda, \tag{2.15}$$

where

$$\lambda = \int_{-\infty}^{\infty} \frac{e^{-\beta/2}\rho(\beta)}{2\beta\,\sinh(\beta/2)}\,d\beta. \tag{2.16}$$

See Appendix B for a step-by-step derivation of this transformation. The parameters $\alpha$ and $\beta$ are given by

$$\alpha = \frac{E'+E-2\mu\sqrt{EE'}}{Ak_{\mathrm{B}}T} \tag{2.17}$$

and

$$\beta = \frac{\varepsilon}{k_{\mathrm{B}}T}. \tag{2.18}$$

The normalized phonon DOS is now expressed as $\rho(\beta)$, and

$$\varepsilon = E' - E \tag{2.19}$$

represents energy gained by the neutron in the scattering process. The terms $\mu$ and $A$ represent the scattering angle cosine in the laboratory frame and the nuclide to neutron mass ratio, respectively. For phonons with energy $\varepsilon$, the value $\frac{1}{2}\left[\frac{e^{-\beta/2}}{\sinh(\beta/2)}\right]$ is the thermal average of the phonon occupation number.

The $S(\alpha,\beta)$ thermal scattering law can be expressed as

$$S(\alpha,\beta) = \sum_{n=1}^{\infty} S_n(\alpha,\beta) = k_\mathrm{B}T \times S_\mathrm{s}(Q,\omega). \tag{2.20}$$

Similar to Eq. (2.13), the relationship

$$S_n(\alpha,\beta) = k_\mathrm{B}T \times {}^{n}S_\mathrm{s}(Q,\omega) \tag{2.21}$$

holds for all $n$. Continuing with the harmonic assumption, the $n$-phonon terms of the scattering law are separable in momentum and energy, or into the form

$$S_n(\alpha,\beta) = f_n(\alpha)g_n(\beta), \tag{2.22}$$

where

$$f_n(\alpha) = e^{-\alpha\lambda}\alpha^n(n!)^{-1} \tag{2.23}$$

and

$$g_n(\beta) = \int_{-\infty}^{\infty} g_1(\beta')g_{n-1}(\beta-\beta')\,d\beta', \text{ for } n \geq 2. \tag{2.24}$$

From Eq. (2.14),

$$g_1(\beta) = \frac{e^{-\beta/2}\rho(\beta)}{2\beta\sinh(\beta/2)}. \tag{2.25}$$

Examining Eq. (2.20), it is clear that $S(\alpha,\beta)$ itself is not separable in momentum and energy. Eq. (2.24) describes the progressive convolution of $g_n(\beta)$ over the phonon DOS [20]. Physically, the sensitivity of multiphonon scattering to the structure of the DOS lessens with increasing phonon order.

As $E \rightarrow 0$, one-phonon scattering becomes increasingly dominant as the neutron has progressively less energy with which to excite phonons. As $E$ increases, and the average momentum transfer (or $\alpha$) increases, multiphonon scattering becomes more prevalent. As material temperature $T \rightarrow 0$, the phonon occupation number is reduced and one-phonon scattering becomes increasingly dominant. As $T$ rises, an increase in the phonon occupation number induces more multiphonon scattering.

The effect of chemical binding on thermal neutron scattering is to discretize the momentum and energy transfer process based on the excitation modes available in the particular molecular structure. In general, the inelastic thermal scattering cross section will be suppressed from the free-gas cross section. When one-phonon scattering is dominant, the secondary neutron energy distribution closely resembles the structure of the phonon DOS. Physically, this is because $S_1(\alpha, \beta)$ is essentially linear with respect to the DOS. As the proportion and order of multiphonon scattering increases, the effect is lessened. In this case, secondary neutron energy distributions become more widely distributed, increasingly featureless, and approach the Maxwell-Boltzmann distribution. The integrated inelastic thermal scattering cross section will then approach the free-gas cross section. In the high-energy limit, as the sensitivity to molecular structure vanishes, the thermal scattering cross section will converge with the free cross section. The free cross section is given by

$$\sigma_{\text{free}} = \sigma_{\text{b}} \left(\frac{A}{A+1}\right)^2 \tag{2.26}$$

and is equivalent to the bound cross section in the zero-momentum frame.

The analytical form of $S(\alpha, \beta)$ discussed above is based on several conditions stated thus far in the development of the theory. In particular, it is based on the incoherent approximation given by Eq. (2.7). The $S(\alpha, \beta)$ data given in File 7 is typically generated with the LEAPR module of the NJOY Nuclear Data Processing System [20] for specified $T$ over $\alpha$ and $\beta$ grids defined by the evaluator. The same methodology will be assumed in the upcoming uncertainty analysis. The phonon DOS in the form of $\rho(\varepsilon)$ is the fundamental input supplied to LEAPR for calculation of the scattering law, where

$$\rho(\beta) = k_{\mathrm{B}}T \times \rho(\varepsilon). \tag{2.27}$$

LEAPR utilizes the incoherent approximation and calculates the $S(\alpha,\beta)$ matrix to a user-specified phonon order via the phonon expansion method outlined previously. However, the format of File 7, MT = 4, is independent of the definition of $S(\alpha,\beta)$ and the method of data production. In principle, $S(\alpha,\beta)$ could be defined either to include the coherent one-phonon scattering term or to include only multiphonon scattering. Experimentally measured or experimentally adjusted $S(\alpha,\beta)$ data could also be incorporated. These choices would have no impact on the manner in which the $S(\alpha,\beta)$ data would be processed.

By noting that

$$k = \frac{\sqrt{2mE}}{\hbar} \text{ and } k' = \frac{\sqrt{2mE'}}{\hbar}, \tag{2.28}$$

where $m$ is the mass of a neutron, and that scattering has no azimuthal angle dependence for randomly oriented microcrystal structure, Eq. (2.8) may now be rewritten in the LEAPR format as

$$\frac{d^2\sigma(E)}{d\mu dE'} = \frac{\sigma_{\mathrm{b}}}{2k_{\mathrm{B}}T}\sqrt{\frac{E'}{E}}S(\alpha,\beta). \tag{2.29}$$

This may be integrated over $\alpha$ to arrive at differential cross sections in energy, or the integration may be carried out over both $\alpha$ and $\beta$ to arrive at the inelastic scattering cross section. To facilitate integration, it is instructive to rewrite Eq. (2.29) as

$$\frac{d^2\sigma(E)}{d\alpha\, d\beta} = \frac{Ak_{\mathrm{B}}T\sigma_{\mathrm{b}}}{4E} S(\alpha,\beta) \tag{2.30}$$

by multiplying by the derivatives $\frac{d\mu}{d\alpha} = \frac{-Ak_{\mathrm{B}}T}{2\sqrt{EE'}}$ and $\frac{dE'}{d\beta} = k_{\mathrm{B}}T$. The negative sign is dropped since the direction of integration is reversed after the transformation from $\mu \rightarrow \alpha$. Eq. (2.17) may be rewritten as

$$\alpha = \frac{2E+\beta k_{\mathrm{B}}T-2\mu\sqrt{E^2+\beta k_{\mathrm{B}}TE}}{Ak_{\mathrm{B}}T}. \tag{2.31}$$

Therefore, any three of the four variables $E$, $\mu$, $\alpha$, and $\beta$ (within their valid ranges) specify the fourth. $S(\alpha,\beta)$ may be calculated, independent of $E$, for any positive $\alpha$ and for any positive or negative $\beta$. However, there is a specified range of $E$ over which the particular $S(\alpha,\beta)$ is physically meaningful. In other words, for any particular $E$, there are physical ranges of $\alpha$ and $\beta$. The range of $E$ is $(0,\infty)$, although structural effects are typically negligible beyond an upper limit of about 5 eV. The range of $\mu$ is $[-1.0,+1.0]$. The physical range of $\beta$ is $[-\frac{E}{k_{\mathrm{B}}T},\infty)$ and the physical range of $\alpha$, as a function of $E$ and $\beta$, is $\left[\frac{2E+\beta k_{\mathrm{B}}T-2\sqrt{E^2+\beta k_{\mathrm{B}}TE}}{Ak_{\mathrm{B}}T},\frac{2E+\beta k_{\mathrm{B}}T+2\sqrt{E^2+\beta k_{\mathrm{B}}TE}}{Ak_{\mathrm{B}}T}\right]$. When integrating Eq. (2.30), these physical limits of integration must be adhered to. Figure 2.2 compares the physical ranges of $\alpha$ with respect to positive $\beta$ for natural carbon ($A$ = 11.908) at temperatures of 293.6 K and 1000 K for incident neutron energies of 0.001 eV and 0.1 eV.

Figure 2.3 presents the phonon DOS, $\rho(\varepsilon)$, used in the ENDF/B-VII File 7 thermal scattering law evaluation for graphite [20, 21]. The spectrum is taken from the work of Young and Koppel (YK) [22], where the lattice dynamics of hexagonal crystalline graphite is represented by four force constants fitted to thermodynamic data for reactor grade graphite.

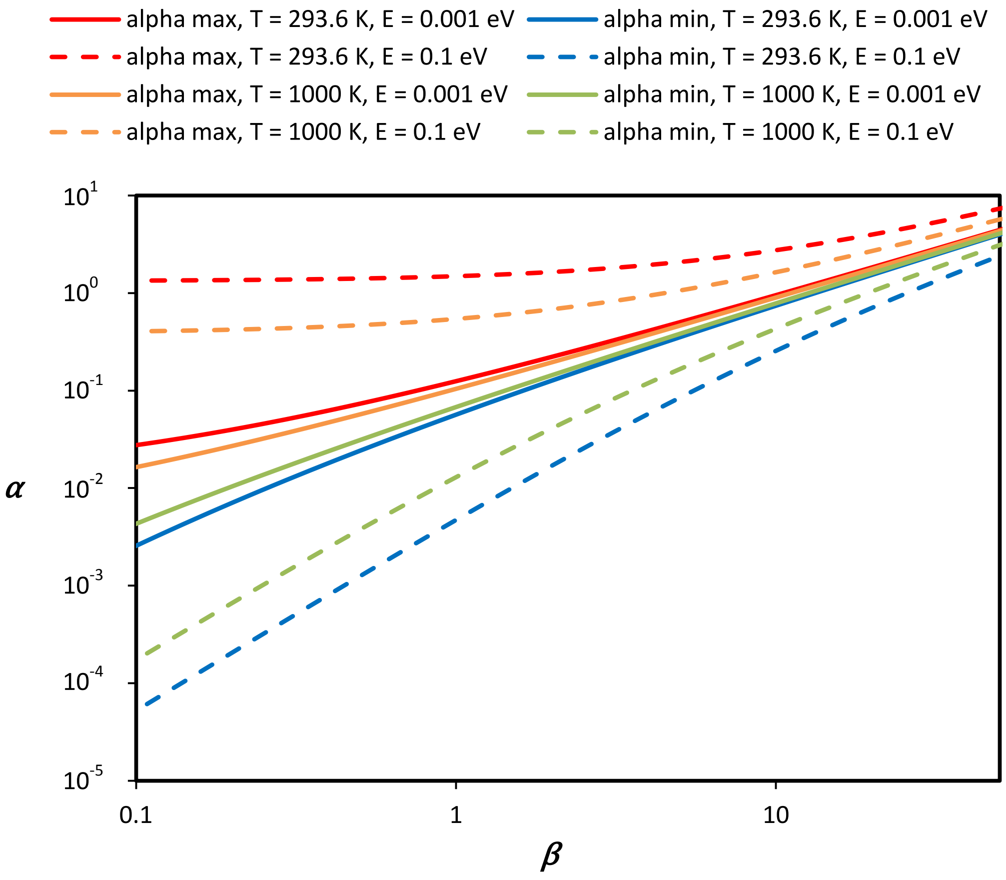

**Figure 2.2 Physical limits of momentum transfer factor $\alpha$ as a function of positive $\beta$ for natural carbon ($A$ = 11.908). Solid lines are associated with $E$ = 0.001 eV. Dashed lines are associated with $E$ = 0.1 eV. Red/blue lines give the upper/lower bounds for $T$ = 293.6 K. Orange/green lines give the upper/lower bounds for $T$ = 1000 K.**

This $\rho(\varepsilon)$ spectrum is supplied to LEAPR to generate the File 7 $S(\alpha,\beta)$ data for graphite. This thermal scattering law data may then be supplied to the THERMR module of NJOY [20] to generate integrated inelastic cross sections and coupled differential cross sections in energy and angle. Figure 2.4 presents the angle-integrated secondary neutron energy distributions produced by THERMR at 293.6 K for incident neutron energies of 0.00016 eV and 0.1116 eV. The impact of the graphite phonon DOS spectral features, such as the peak

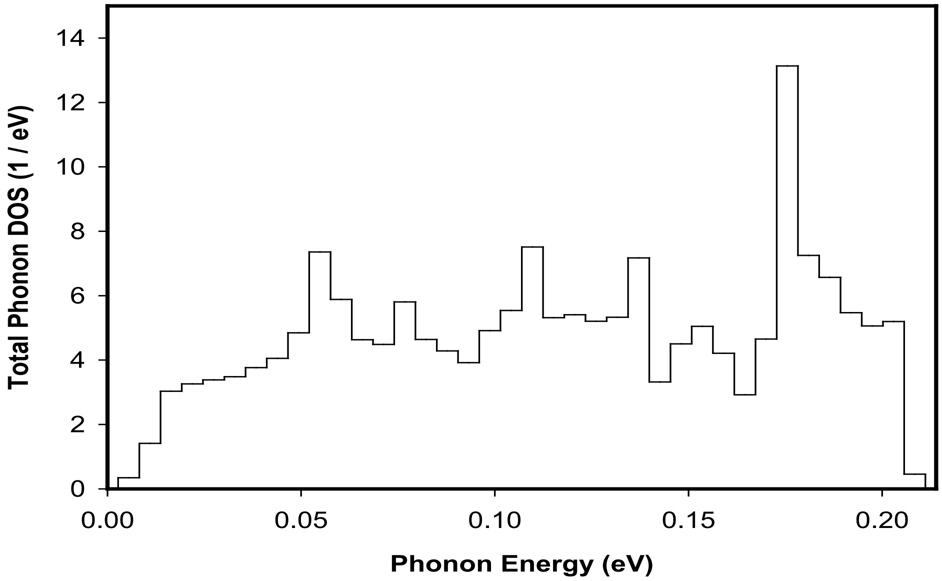

**Figure 2.3 Total phonon DOS, $\rho(\varepsilon)$, supplied to LEAPR to generate the ENDF/B-VII File 7 thermal scattering law evaluation for graphite at 293.6 K. The spectrum is taken from the work of Young and Koppel [22].**

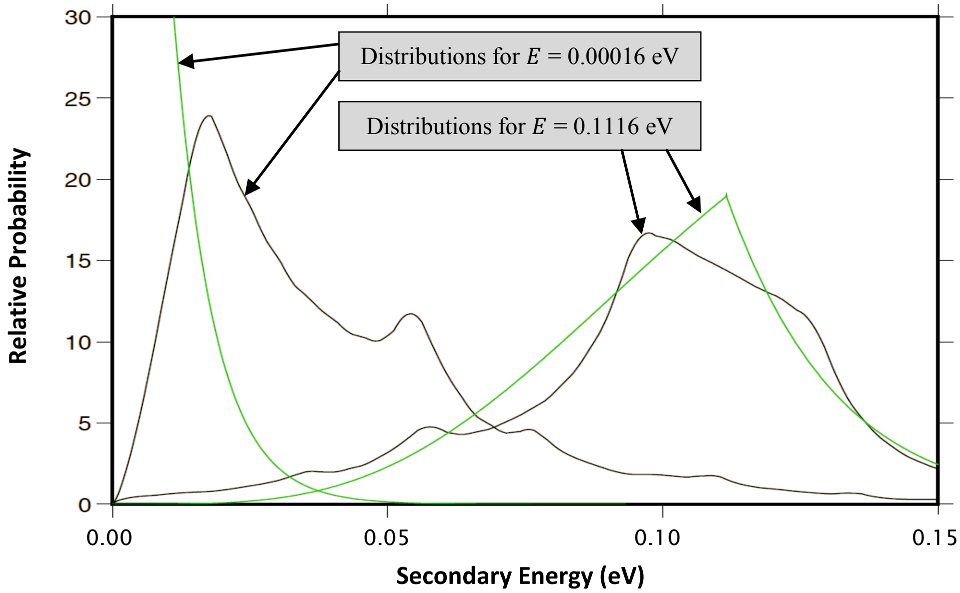

**Figure 2.4 Secondary neutron energy distributions for graphite at 293.6 K. Data is produced by THERMR using ENDF/B-VII File 7 thermal scattering law data (black) and the free-gas model (green) for $E = 0.00016$ eV and $E = 0.1116$ eV [20].**

near 55 meV, is clear. The results are compared to the Maxwell-Boltzmann distributions of a free-gas model for natural carbon [20].

The principle of detailed balance applies in general for scattering in materials consisting of only zero-spin nuclides. The result is $S(\alpha,\beta) = e^{-\beta}S(\alpha,-\beta)$. Most natural materials contain negligible fractions of nuclides with non-zero spin. In this case, a symmetric scattering law may be defined as

$$S_{\mathrm{sym}}(\alpha,\beta) = e^{\beta/2}S(\alpha,\beta) \tag{2.32}$$

such that $S_{\mathrm{sym}}(\alpha,\beta) = S_{\mathrm{sym}}(\alpha,-\beta)$. To reduce file size, this is the actual quantity conventionally tabulated (for positive $\beta$ only) in ENDF File 7 thermal neutron scattering libraries [20]. Eq. (2.30) may be rewritten in terms of $S_{\mathrm{sym}}(\alpha,\beta)$ as

$$\frac{d^2\sigma(E)}{d\alpha\, d\beta} = \frac{Ak_{\mathrm{B}}T\sigma_{\mathrm{b}}}{4E}e^{-\beta/2}S_{\mathrm{sym}}(\alpha,\beta). \tag{2.33}$$

For scattering in a crystal having more than one non-equivalent basis position per unit cell, the phonon DOS and Debye-Waller factor may be specified separately for each basis position. When a single chemical element is present, $S(\alpha,\beta)$ and cross sections may then be calculated as an average over all basis positions. However, in LEAPR, it is standard in this case to provide a single effective phonon DOS representing an average DOS over the basis positions. When different chemical elements populate the basis positions, $S(\alpha,\beta)$ and cross sections may be calculated based on the desired stoichiometry. Natural materials often have multiple randomly distributed elemental isotopes. The DOS, $S(\alpha,\beta)$ and calculated cross sections may be defined based on the isotopically weighted averages of $\sigma_{\mathrm{b}}$ and $A$ in this case.

# Chapter 3

# Thermal Neutron Inelastic Scattering Uncertainty

## 3.1 Principles and Methods of Uncertainty Quantification

The value assigned to any physical quantity will depend on the process by which the value is determined. This process may involve measurement, calculation, assessment of existing information regarding the value of the quantity, or some combination of these. With the exception of physical quantities having simply determined integer values, the true value of a physical quantity is very often unknown and cannot be determined exactly. In this case, to be complete, the value assigned to the quantity should be accompanied by a mathematical description of its uncertainty.

Qualitatively, the uncertainty assigned to a value is a measure of the level of confidence that this value corresponds to the true value, taking into consideration all available information [5]. Quantitatively, uncertainty is held to have a precise mathematical definition in terms of the second central moments of the probability distributions that govern the processes through which knowledge about the value of the physical quantity is derived [23].

### 3.1.1 Mathematical and Statistical Description of Uncertainty

To give a mathematical description of uncertainty, it is first necessary to introduce the concept of a random variable. A random variable is any parameter (such as a physical quantity or an empirical fitting parameter) having a value that is subject to variation. In contrast, values assigned to a non-random variable are exactly determined. The term "variation" in this context is time-independent and refers in general to any description of some aspect of the manner in which the value for the random variable may be expected to fluctuate. For a random variable representing a physical quantity (such as a cross section), the variation can depend on the measurement process, the calculation methodology, existing information (or lack of information) about the quantity, or a combination of these.

The variation of any random variable can be described based on the probability distribution, or the probability density function (PDF), of the population of all possible values for the random variable. The PDF for a random variable representing a physical quantity is generally not known explicitly and must be assumed or estimated by an evaluator based on the method employed in determining the value for the physical quantity and on any other pertinent information available regarding its value [5]. Often, this PDF will represent the combined effect of multiple aspects of the process through which the value for the quantity is determined, each of which may have an underlying PDF associated with it. The application of a least-squares fitting procedure is a common method for estimating the PDF when a function of a random variable can be compared to experimental data. Another common method of estimating the PDF is by generating a discrete sample of values for the random variable through some process which is assumed to be representative of the PDF or some underlying component of the PDF.

For a given PDF governing the variation in a random variable $x$,

$$\sigma(x) = \sqrt{\int_{-\infty}^{\infty} (x - < x >)^2 p(x) dx} \tag{3.1}$$

defines the uncertainty in $x$. The term $p(x)$ is the PDF for the random variable $x$, and the notation $< x >$ denotes the expectation value for the random variable $x$. For a given $p(x)$, the expectation value is the probability-weighted mean of possible $x$ values. In general, this expectation value will not represent the true value for a physical quantity, $x_{\text{true}}$, but it is defined as the best estimate for $x_{\text{true}}$ based on the given method of determining a value and any other pertinent information. The quantity $\sigma^2(x)$ is defined as the variance of the random variable $x$ and is a measure of the dispersion of $x$ about $< x >$ as a function of $p(x)$.

When a single value is determined for a physical quantity through some process, this value is often taken to be the expectation value and is the quoted value for the physical quantity represented by $x$. A corresponding form for $p(x)$ is then assumed or estimated by the evaluator to determine $\sigma(x)$. If the evaluator has information to suggest that the value determined for the physical quantity through a particular process should not be assumed to be representative of the expectation value for the physical quantity, a correction can be applied. In this case, $p(x)$ should capture any underlying probability distribution for the correction.

When a discrete sample of values for $x$ is given, the sample uncertainty is defined as

$$s(x) = \sqrt{\tfrac{1}{N-1}\textstyle\sum_{i=1}^{N}(x_i - \bar{x}_s)^2}, \tag{3.2}$$

where $\bar{x}_{\text{s}}$ is the sample mean and $N$ is the number of sample data points $i$. There are $N-1$ degrees of freedom in defining the variance of $N$ $x_i$ with respect to $\bar{x}_{\text{s}}$. For sufficiently large $N$, if the sampling probability is representative of $p(x)$, $s(x) \approx \sigma(x)$ and $s^2(x) \approx \sigma^2(x)$. In this case, the sample data can be expected to predict the uncertainty and variance in the random variable $x$ well. For discrete sample data, $< x >$ is estimated by $\bar{x}_{\text{s}}$, modified by any applicable correction. Assuming the sampling PDF is effectively time-independent over the sampling period, $\bar{x}_{\mathrm{s}}$ converges to $x_{\mathrm{c}}$ as $N \longrightarrow \infty$, where $x_{\mathrm{c}}$ is the expectation value for the sampling PDF. For finite $N$, $p(x)$ can be considered to be a function of $p(\bar{x}_{\mathrm{s}})$ and $p(x_{\mathrm{true}} - \bar{x}_{\mathrm{s}})$. As $N \longrightarrow \infty$, $p(\bar{x}_{\mathrm{s}})$ localizes, and $p(x)$ becomes a function of $x_{\mathrm{c}}$ and $p(x_{\mathrm{true}} - x_{\mathrm{c}})$. For $N = 1$, $\bar{x}_{\mathrm{s}} = x_{\mathrm{c}}$.

A set of random variables $[x_1, x_2, \ldots, x_n]$ can be expressed as the vector $\boldsymbol{x}$ to represent a set of physical quantities. These random variables may be independent or dependent. If the set is independent, then the vectors $<\boldsymbol{x}> = [<x_1>, <x_2>, \ldots, <x_n>]$ and $\boldsymbol{\sigma}(\boldsymbol{x}) = [\sigma(x_1), \sigma(x_2), \ldots, \sigma(x_n)]$ report sufficient information about the values and uncertainties for the physical quantities. If the set is dependent, there will be a joint probability density function $p(\boldsymbol{x}) = p(x_1, x_2, \ldots, x_n)$ governing the variation of the set of random variables. In this case, Eqs. (3.1) and (3.2) still apply in determining the uncertainty for a particular random variable. However, the covariance of any two random variables is defined as

$$\mathrm{COV}(x_i, x_j) = \int_{x_j=-\infty}^{x_j=\infty} \int_{x_i=-\infty}^{x_i=\infty} (x_i - <x_i>)(x_j - <x_j>) p(x_i, x_j) dx_i dx_j. \tag{3.3}$$

Covariance is a measure of the coupling of the variations of two random variables. For $i = j$ in Eq. (3.3), $\mathrm{COV}(x_i, x_i) = \sigma^2(x_i)$. The joint PDF is generally not known explicitly. A multi-dimensional least-squares approach is a historically common method of determining nuclear data covariances based on empirical models and experimental data. Alternatively, similar to estimating a single-variable PDF, generating discrete samples of values for the set of random variables allows covariances to be estimated.

When a discrete sample of $\boldsymbol{x}$ values is given, covariances are defined as

$$\mathrm{COV_s}\left(x_i, x_j\right) = \frac{1}{N-1}\sum_{i=1}^{N}\sum_{j=1}^{N}[x_i - (\bar{x}_i)_\mathrm{s}]\,[x_j - (\bar{x}_j)_\mathrm{s}]. \tag{3.4}$$

A sample consists of a number of data sets $\{x_1, x_2, \dots, x_n\}$, and there are $N$ data sets. For large $N$, if the sampling probability is representative of the joint PDF, $\mathrm{COV_s}\left(x_i, x_j\right)$ converges to $\mathrm{COV}\left(x_i, x_j\right)$. Whether covariances are determined through Eq. (3.3), Eq. (3.4) or otherwise, a covariance matrix for $\boldsymbol{x}$ of dimension $n \times n$ must be given, along with $< \boldsymbol{x} >$, to provide complete information regarding the quoted values for the random variable set $\boldsymbol{x}$. The notation $\boldsymbol{V_x}$ will be used to designate the covariance matrix for $\boldsymbol{x}$, with entries $(\boldsymbol{V_x})_{ij}$ given by $\mathrm{COV}\left(x_i, x_j\right)$. The diagonal of the covariance matrix will give the variances for each random variable, and the square roots of the diagonal terms provide the uncertainties given by $\boldsymbol{\sigma}(\boldsymbol{x})$.

A correlation matrix $\boldsymbol{C}$ is defined in terms of the covariance matrix $\boldsymbol{V}$ by

$$\boldsymbol{C}_{ij} = \boldsymbol{V}_{ij}/(\sigma_i \sigma_j). \tag{3.5}$$

The use of a correlation matrix, versus a covariance matrix, eliminates the presence of units and restricts numerical values to [-1.0,+1.0]. Correlations are often considered more intuitive than covariances and more natural for plotting and visual examination. Furthermore, when statistical methods are impracticable for the determination of covariances, evaluators often attempt to assess correlations directly. Correlation is a measure of the linear functional dependence between two random variables. A value of +1.0 or -1.0 implies that two random variables will always vary in linear proportion in the same direction (for +1.0) or in the opposite direction (for -1.0). Two independent random variables will have a correlation of zero. However, if their covariance is calculated with discrete samples of values per Eq. (3.4), the resulting correlation will likely be non-zero due to the discrete data imperfectly representing the corresponding joint PDF. For a sufficiently large number of samples, the calculated correlation for two independent random variables will be very small in magnitude. Conversely, it is important to note that a very small calculated correlation does not necessarily imply independence between two random variables but only a very limited linear functional dependence. Higher-order functional dependence could still exist [23].

### 3.1.2 Types of Uncertainty and Methods of Evaluation

Uncertainties can generally be separated into two broad categories based on the inherent nature of the source of uncertainty:

1. Uncertainties arising due to a *random* effect.
2. Uncertainties arising due to a *systematic* effect.

These types of uncertainties are independent of the manner in which they are mathematically evaluated to arrive at $\sigma(x)$. Specifically, they depend on the details of the particular method for determining a value for $x$ [24].

A Type 1 uncertainty is defined as an uncertainty which may be minimized through repeated trials of a particular sampling process. This process may involve measurement, calculation, or some combination of both. Specifically, if the PDF governing the values determined by a particular sampling process is consistent from trial to trial, then $\sigma(\bar{x}_s)$ is Type 1. This definition applies whether a single trial is performed or many. Furthermore, it is independent of whether or not repeated trials will result in the sample mean converging to the true value or the evaluated expectation value for a physical quantity. Type 1 uncertainties affect the *precision* to which the value of a physical quantity may be determined.

A Type 2 uncertainty is defined as an uncertainty which cannot be minimized through repeated trials of a particular sampling process. Uncertainties independent of the PDF for a particular sampling process are of Type 2. In this case, the Type 2 uncertainty is defined as $\sigma(x_{\text{true}} - \bar{x}_{\text{s}})$. If a particular sampling process has a PDF that is time-dependent over the sampling period, then $\sigma(\bar{x}_{\text{s}})$ is a Type 2 uncertainty unless specific information describing the time-dependence allows $\sigma(\bar{x}_{\text{s}})$ to be reduced to a Type 1 uncertainty. If no Type 2 uncertainties exist, the sample mean should be expected to converge to the true value of the physical quantity with repeated trials. In practice, Type 2 uncertainties are almost always present, are often difficult to identify and evaluate, and will typically be responsible for the majority of uncertainty in any physical quantity. Type 2 uncertainties affect the *accuracy* with which a physical quantity may be determined. They can lead to a *bias* in the value determined by a particular process. In general, a Type 2 uncertainty describes the uncertainty in a correction to a determined value necessary to arrive at $< x >$ for a physical quantity.

The classifications Type 1 and Type 2 distinguish the underlying nature of uncertainties. However, both types may be evaluated (or quantified) in different ways. Evaluation methodologies may be divided into two general categories [24]:

A. Evaluations based on strictly statistical methods.

B. Evaluations based on scientific judgment and/or the interpretation of pertinent information available regarding the quantity of interest.

Figure 3.1 gives three possible PDFs for a random variable $x$ which will be used to illustrate examples of Type 1 and 2 uncertainties and Type A and B evaluation methods. Consider the PDFs to represent (either exactly or by estimate) the energy distribution registered by three different detectors (A, B and C) over a fixed time period for the same incident beam of monoenergetic gammas. The energy units are arbitrary and the scale is exaggerated for illustration purposes. The physical quantity represented by $x$ is the gamma energy.

For Detector A, if the distribution is the result of actual detections, then $\sigma(\bar{x}_s)$ is a Type A evaluation of a Type 1 uncertainty, and no assumption is made about the presence of Type 2 uncertainties. If a normal distribution for $x$ is assumed based only on determining that the measured distribution is centered about $E = 100$ with a full-width half-maximum (FWHM)

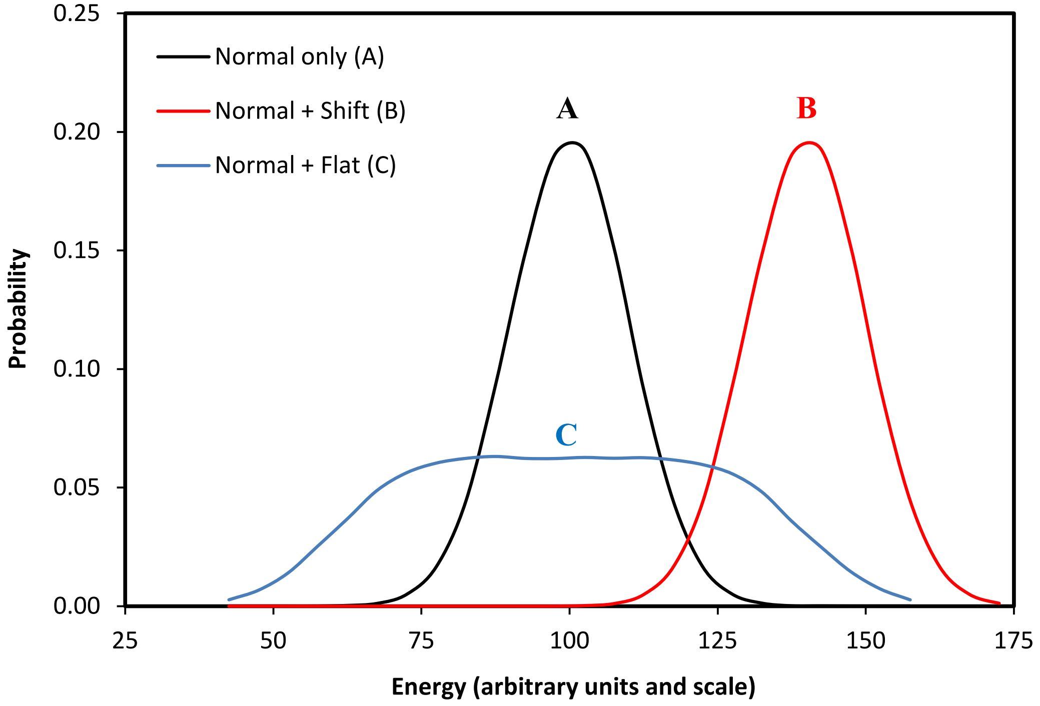

**Figure 3.1 Three example PDFs for a random variable $x$.**

of 25, then $\sigma(x)$ is a Type B evaluation of a Type 1 uncertainty, and Type 2 uncertainties are assumed to be zero.

Detector B may be assumed to have a fixed calibration error (energy shift) of +40 based on comparison to Detector A (where Detector A is assumed to be perfectly calibrated). Such an assumption is a Type B evaluation of a Type 2 uncertainty. In other words, a correction to $\bar{x}_s$ is determined to be required to arrive at $< x >$, and the uncertainty in this correction is estimated to be zero. If the given distribution for Detector B is the result of actual detections, $\sigma(\bar{x}_s)$ is again a Type A evaluation of a Type 1 uncertainty. If the distribution is assumed to be normal but shifted by +40, then $\sigma(x)$ is a Type B evaluation of Type 1 and 2 uncertainties.

Detector C has a random calibration fluctuation (possibly due to electrical noise). For this situation, if the given distribution is the result of actual detections, $\sigma(\bar{x}_s)$ is still a Type A evaluation of a Type 1 uncertainty. If $\sigma(x_{\text{true}} - \bar{x}_s)$ is based on a flat distribution for the calibration error, this is a Type B evaluation of a Type 2 uncertainty. If $\sigma(x_{\text{true}} - \bar{x}_s)$ is estimated by collecting data after replacing the gamma source with a test pulse subject to the same calibration fluctuation, this is a Type A evaluation of a Type 2 uncertainty.

The end goal is to provide the expectation values for the set of all quantities of interest, along with an associated covariance matrix from which total uncertainties and correlations may be calculated [23]. To achieve this, the evaluator must construct a joint probability density function which properly reflects all known information about the quantities [5]. There is certainly no single "correct" answer to this task. In particular, scientific judgment will often be necessary in the treatment of Type 2 uncertainties and covariances. As a practical matter, if a user is to accept and apply a nuclear library produced by a particular method, there should be the expectation that any uncertainty information associated with it appropriately reflects the extent of knowledge available to the evaluator in its generation.

### 3.1.3 Propagation of Uncertainty

Any function of one or more random variables can also be treated as a random variable. Often, the uncertainty information for underlying parameters which govern the determination of a physical quantity will be more accessible than for the physical quantity itself. Any differentiable function of two random variables $x_i$ and $x_j$ can be Taylor-expanded about $< x_i >$ and $< x_j >$ to first order as

$$f(x_i, x_j) \approx f(< x_i >, < x_j >) + x_i \frac{\partial f(x_i,x_j)}{\partial x_i} \Big|_{x_i,x_j=<x_i>,<x_j>}$$

$$+x_j \frac{\partial f(x_i,x_j)}{\partial x_j} \Big|_{x_i,x_j=<x_i>,<x_j>}. \tag{3.6}$$

A small change $\Delta x_i$ in $x_i$ and a small change $\Delta x_j$ in $x_j$ will result in a small change $\Delta f(x_i, x_j)$ in $f(x_i, x_j)$. Assuming that $\Delta x_i = x_i - < x_i >$ and $\Delta x_j = x_j - < x_j >$ are sufficiently small over the probable ranges for $x_i$ and $x_j$, $f(x_i, x_j)$ can be considered linear with respect to $x_i$ and $x_j$ in the region near $f(< x_i >, < x_j >)$. In this case, $\Delta f(x_i, x_j) \approx f(x_i, x_j) - f(< x_i >, < x_j >)$ and

$$f(x_i, x_j) - f(< x_i >, < x_j >) \approx [x_i - < x_i >] \frac{\partial f(x_i,x_j)}{\partial x_i} \Big|_{x_i,x_j=<x_i>,<x_j>}$$

$$+[x_j - < x_j >] \frac{\partial f(x_i,x_j)}{\partial x_j} \Big|_{x_i,x_j=<x_i>,<x_j>}. \tag{3.7}$$

Squaring both sides of Eq. (3.7) gives

$$\begin{aligned}[f(x_i, x_j) - f(< x_i >, < x_j >)]^2 \approx {} & [x_i - < x_i >]^2 \frac{\partial^2 f(x_i,x_j)}{\partial x_i} \mid_{x_i,x_j=<x_i>,<x_j>} \\ & + [x_j - < x_j >]^2 \frac{\partial^2 f(x_i, x_j)}{\partial x_j} \mid_{x_i,x_j=<x_i>,<x_j>} + \\ & 2 \times [x_i - < x_i >][x_j - < x_j >] \left[\frac{\partial f(x_i,x_j)}{\partial x_i} \frac{\partial f(x_i,x_j)}{\partial x_j}\right] \mid_{x_i,x_j=<x_i>,<x_j>}. \end{aligned} \tag{3.8}$$

Now, taking the expectation value of each side of Eq. (3.8) yields the desired relation

$$\begin{aligned}\sigma^2[f(x_i, x_j)] \approx {} & \sigma^2(x_i) \frac{\partial^2 f(x_i,x_j)}{\partial x_i} \mid_{x_i,x_j=<x_i>,<x_j>} + \sigma^2(x_j) \frac{\partial^2 f(x_i,x_j)}{\partial x_j} \mid_{x_i,x_j=<x_i>,<x_j>} \\ & + 2 \times \mathrm{COV}(x_i, x_j) \left[\frac{\partial f(x_i,x_j)}{\partial x_i} \frac{\partial f(x_i,x_j)}{\partial x_j}\right] \mid_{x_i,x_j=<x_i>,<x_j>}. \end{aligned} \tag{3.9}$$

The result of Eq. (3.9) may be generalized to any number of random variables to produce the familiar algebraic propagation of uncertainty formula

$$\sigma[f(x_1, \dots, x_n)] = \sqrt{\sum_{i=1}^{n} \left(\frac{\partial f}{\partial x_i}\right)^2 \sigma^2(x_i) + 2 \sum_{i=1}^{n-1} \sum_{j=i+1}^{n} \frac{\partial f}{\partial x_i} \frac{\partial f}{\partial x_j} \mathrm{COV}(x_i, x_j)}, \tag{3.10}$$

where the approximate equivalence is treated as exact by definition.

The propagation of uncertainty formula given by Eq. (3.10) may be extended to an arbitrary number of functions and written in a simplified matrix form as

$$\boldsymbol{V_y} = \boldsymbol{M}_{\boldsymbol{xy}}^{\mathrm{T}} \boldsymbol{V_x} \boldsymbol{M_{xy}}. \tag{3.11}$$

$\boldsymbol{V_x}$ and $\boldsymbol{V_y}$ are the covariance matrices for the input variable set $\boldsymbol{x}$ and the output data set $\boldsymbol{y}$. $\boldsymbol{M_{xy}}$ is the sensitivity matrix for each $y_j$ with respect to each $x_i$ with entries

$$M_{ij} = \frac{\partial y_j}{\partial x_i}. \tag{3.12}$$

For any data set calculated as functions of an underlying set of parameters which may be treated as random variables, uncertainty information for the output data set may be expressed, to first order, by specifying the covariance matrix for the input variable set along with a sensitivity matrix. As discussed in Section 1.2, ENDF File 30 incorporates this methodology, utilizing Eq. (3.11), to provide a compact format for storing large quantities of covariance data when the parent data is calculated from mathematical models [1].

For example [7], direct representation of the covariances for $10^5$ data entries requires a matrix with $10^5 \times 10^5 = 10^{10}$ elements. Assuming that 100 model parameters are employed, only a $100 \times 100$ parameter covariance matrix and a $10^5 \times 100$ sensitivity matrix is needed, reducing the required number of elements by 99.9% to about $1 \times 10^7$. Of course, only one-half of any covariance matrix need be stored due to symmetry. The reduction in storage requirements possible using Eq. (3.11) can be particularly advantageous in expressing covariances for very large quantities of secondary distribution data. The File 30 format also provides a clear route for calculating multigroup data covariances for a specified group structure since the loss of differential information could be limited by maintaining high covariance resolution [25].

There are also disadvantages to use of the File 30 format. It implicitly assumes linearity in the functional relationship among the model parameters and in the calculated nuclear data as a function of the model parameters. Over the global range of a parameter vector $\boldsymbol{x}$, significant nonlinearities may be present. However, the linear assumption is normally a good approximation if the probable range of $\boldsymbol{x}$ is localized about $<\boldsymbol{x}>$, and this condition typically holds. Therefore, the first-order form of Eq. (3.11) generally provides sufficiently accurate and physically acceptable results while greatly compacting data storage [25].

### 3.1.4 Monte Carlo Sampling and Simulation

The mathematical simulation of random processes is known as the Monte Carlo method. When the behavior of any number of random variables can be simulated mathematically, this allows a straightforward statistical treatment of a wide variety of problems. First, a general description of a Monte Carlo trial and of Monte Carlo sampling will be given. Next, the basic principles of the Monte Carlo method will be discussed. Finally, several example applications for the Monte Carlo method will be described.

Let a process be defined which contains one or more decision steps. These steps may be considered to occur in series, in parallel, or in combination. The number and sequence of these steps in the process can be constant or variable. For each decision step, a range of outcomes is possible according to some frequency distribution. The outcomes for the decision steps may be independent or dependent. The process may also contain any number of non-decision steps, where each output is fixed as a function of the input. The information resulting after the execution of the entire process comprises the outcome of one Monte Carlo trial. The repeated execution of the process and the collection of information resulting from these trials is known as Monte Carlo sampling [23].

The application of any Monte Carlo method depends on the ability to generate random numbers according to some frequency distribution. While no algorithm can produce a truly random number, there are many algorithms that exist in computer applications which can generate numbers which are, for practical intent, sufficiently random. The success of the Monte Carlo method lies in the central limit theorem. The central limit theorem states that if $M$ average values of a random variable are determined by $M$ repetitions of sampling the probability distribution for the random variable $N$ times, then the distribution of average values will converge to a normal distribution as $M \longrightarrow \infty$ and this normal distribution will converge to a central limit as $N \longrightarrow \infty$. Certain conditions apply, including the requirement that the probability distribution has a well-defined expectation value and variance. However, the central limit theorem applies in general to any Monte Carlo process as outlined in the previous paragraph. The values determined for measurands of a Monte Carlo process are by definition averages of outcomes for $N$ trials. Therefore, the value determined for any particular measurand of a Monte Carlo process may be expected to converge to a central limit with increasing $N$, and the probability distribution for the measurand can be considered normal [23].

A simple application of the Monte Carlo method is the numerical evaluation of an integral with no closed-form solution. For instance, consider $y = \int_a^b e^{-x^2} dx =< e^{-x^2} >\times (b-a)$. The term $< e^{-x^2} >$ can be easily determined by randomly sampling $x$ using a flat probability distribution bounded by $a$ and $b$. This will yield a solution for $y$ with a corresponding $\sigma(y)$. The Monte Carlo method is also useful in solving very complicated problems involving many integrals, in solving large sets of coupled differential equations, in performing complicated least-squares fits, in quantifying uncertainties and covariances, and in many other mathematical applications. The Monte Carlo method allows statistical solutions to a wide variety of problems which may otherwise be difficult or virtually impossible to solve by deterministic methods.

An important application of the Monte Carlo method is in the simulation of the behavior of very complex physical systems. Nuclear systems are particularly amenable to Monte Carlo analysis because particle transport and interactions are naturally governed by random processes which can be described by the reaction information tabulated in nuclear data libraries. The behavior of the neutron population of nuclear systems can be statistically simulated in time, space and energy. The accuracy of the Monte Carlo method is limited only by how well formulated the system description is, the number of Monte Carlo trials executed, and the completeness and accuracy of the nuclear data provided. Clearly, for nuclear systems in which the great majority of fission events are induced by thermal neutrons, it is particularly important to understand the behavior of the thermal neutron population well. Whether a nuclear system is simulated by a Monte Carlo or a deterministic method, the ability to provide thermal neutron scattering uncertainty information in the applied nuclear data library is of high interest.

Just as the characteristics of a physical system may be determined through Monte Carlo simulation, the characteristics of a mathematical function (such as a PDF) may be determined in the same manner. In some cases, a required function may not be known, or it may itself have a probability distribution. By using Monte Carlo simulation to model fundamental phenomena governing the function, a statistical description can be generated taking into account all available information regarding the behavior of the function and underlying phenomena.

## 3.2 Assessing the Thermal Scattering Uncertainty Problem

### 3.2.1 Covariance Data Requirements for Simulation Codes

In reactor analysis and criticality safety applications, system response parameters may be very sensitive to the characteristics of the thermal neutron flux distribution. The scattered neutron energy spectra, which are functions of molecular structure, can play a major role in determining the thermal neutron energy distribution of a nuclear system. The details of the thermal neutron energy distribution are essential in determining reaction rates. Consequently, this can affect criticality parameters and safety margins.

Calculating uncertainties and representing covariances for thermal neutron inelastic scattering data presents unique challenges. It is insufficient to quantify a covariance matrix for integrated cross sections since this information alone cannot be unfolded and decoupled to express covariance data for energy and angle distributions. The double-differential thermal scattering law data in ENDF File 7 is rarely used directly in nuclear system modeling and simulation codes. Rather, it is commonly processed to produce a pointwise energy library that can be directly utilized in system calculations. A pointwise energy library contains integrated cross section data tabulated at specific energies. For each energy given, the tabulation of differential data (coupled in energy and angle) is associated with specific secondary energies and scattering angles.

In principle, to present a complete description of thermal neutron scattering uncertainties in such a pointwise energy library, it would be required to provide covariance data collectively for all integrated and differential data for all incident energies. For most nuclear engineering applications, the details of neutron scattering angle distributions are far less important than secondary distributions in energy. In this work, uncertainties and covariances associated with differential cross sections in angle are not considered. Because many simulation codes employ different types and formats of data libraries, a general method is needed for calculating integrated and secondary energy distribution covariances. In most cases, the ENDF File 7 thermal library provides the fundamental double-differential thermal scattering law information upon which the thermal scattering data in code-specific libraries is based. Therefore, it should form the basis for thermal scattering uncertainty quantification.

### 3.2.2 Representing Differential and Integrated Covariances with a Thermal Scattering Law Covariance Matrix

It is clear, upon reviewing Eq. (2.33), that any particular integrated or differential cross section can be calculated by numerically integrating $e^{-\beta/2}S_{\mathrm{sym}}(\alpha,\beta) = S(\alpha,\beta)$ over appropriate ranges of $\alpha$ and/or $\beta$, and then multiplying by the constant $\frac{Ak_{\mathrm{B}}T\sigma_{\mathrm{b}}}{4E}$. Let the set of all integrated and differential cross sections be collectively defined as the output data set $\boldsymbol{y}$. Let the set of all tabulated $S_{\mathrm{sym}}(\alpha,\beta)$ at a specified $T$ in ENDF File 7 be defined as the input data set $\boldsymbol{s}$. The physical limits of $\alpha$ and $\beta$ are governed by the specified $E$ and $T$. (For an example, see Figure 2.2). The matrix propagation of uncertainty formula given by Eq. (3.11) allows $\boldsymbol{V_y}$ to be expressed as a function of $\boldsymbol{V_s}$ and $\boldsymbol{M_{sy}}$. This follows the basis of ENDF File 30 [1], as discussed in Section 3.1.3, except the tabulated $S_{\mathrm{sym}}(\alpha,\beta)$ are now considered "input parameters." Alternatively, $S(\alpha,\beta)$ could have been defined as the input parameter set without loss of generality. The choice of $S_{\text{sym}}(\alpha,\beta)$ is simply to provide consistency with the actual values conventionally tabulated in File 7.

Since $\frac{d^2\sigma(E)}{d\alpha\, d\beta}$ is linear with respect to all $s_i$ in Eq. (2.33), each $y_j$ is also linear with respect to all $s_i$. The integrated inelastic cross section $\sigma_{\text{inel}}(E)$ can be expressed, for specified $T$, by the algebraic summation

$$\sigma_{\text{inel}}(E) = \frac{Ak_{\text{B}}T\sigma_{\text{b}}}{4E}\sum_{a,b}\left(e^{-\beta_b/2}s_{i(a,b)}d\alpha_a d\beta_b\right),$$

$$a = a_{\text{min}} \dots a_{\text{max}}, b = b_{\text{min}} \dots b_{\text{max}}. \qquad (3.13)$$

The term $i(a,b)$ defines the particular $s_i$ associated with $\alpha_a$ and $\beta_b$. The $\alpha$ and $\beta$ grids may be arbitrarily spaced. Therefore, $d\alpha_a$ and $d\beta_b$ are defined by the grids selected by the evaluator. The ranges of $a$ and $b$ are determined by all $\alpha_a$ and $\beta_b$ that lie within the physical bounds $\left[\frac{2E+\beta k_{\text{B}}T-2\sqrt{E^2+\beta k_{\text{B}}TE}}{Ak_{\text{B}}T}, \frac{2E+\beta k_{\text{B}}T+2\sqrt{E^2+\beta k_{\text{B}}TE}}{Ak_{\text{B}}T}\right]$ and $[-\frac{E}{k_{\text{B}}T}, \infty)$ for $\alpha$ and $\beta$, respectively. Eq. (3.13) can be modified for differential cross sections by carrying out the summation over only one variable with the other variable fixed. In this case, there will be no differential term (i.e., $d\alpha_a$ or $d\beta_b$) associated with the fixed variable.

When applying Eq. (3.13), the physical bounds for $\alpha$ and $\beta$ will generally not lie exactly on grid points. Likewise, the grids desired for tabulating differential cross sections may not coincide with the $\alpha$ and $\beta$ grids. It is conventional to apply linear interpolation between tabulated $S_{\text{sym}}(\alpha,\beta)$ in both of these cases. To convert calculated differential cross sections into terms with respect to $dE'$ and/or $d\Omega$, the relationships $d\beta = \frac{dE'}{k_{\text{B}}T}$ and/or $d\alpha = \frac{4\pi\sqrt{EE'}}{Ak_{\text{B}}T}d\Omega$ are applied, respectively.

As a result of the linearity of $\boldsymbol{y}$ with respect to $\boldsymbol{s}$, the terms $M_{ij} = \frac{\partial y_j}{\partial s_i}$ of the sensitivity matrix $\boldsymbol{M_{sy}}$ can be expressed as the constants

$$c_{ij} = \frac{A k_{\mathrm{B}} T \sigma_{\mathrm{b}}}{4E} e^{-\beta_{b(i,j)}/2} \, d\alpha_{a(i,j)} d\beta_{b(i,j)}. \tag{3.14}$$

The functions $a(i,j)$ and $b(i,j)$ each output two pieces of information. First, the functions identify the particular $a$ and $b$ associated with the index $i$. Second, the functions identify whether or not the particular $\alpha_a$ and $\beta_b$ values are physically applicable for the associated $y_j$ (which is a function of $E$). If not, the value of $c_{ij}$ is zero. In fact, for fixed $i$, the $c_{ij}$ corresponding to $j$ for which they are physically applicable are all identical in value.

Inspecting Eq. (3.14), it is clear that the sensitivity matrix $\boldsymbol{M_{sy}}$ need not even be provided, as its elements can be quite trivially computed when required. For example, any particular element of $\boldsymbol{V_y}$ can be expressed as

$$\mathrm{COV}(y_k, y_l) = \textstyle\sum_{q,r} c_{qk} c_{rl} \mathrm{COV}(s_q, s_r)\,, q = q_{\min} \dots q_{\max}, r = r_{\min} \dots r_{\max}. \tag{3.15}$$

In Eq. (3.15), $q$ and $r$ are indices that increment the rows and columns of $\boldsymbol{V_s}$ to calculate the covariance associated with the $k^{\mathrm{th}}$ and $l^{\mathrm{th}}$ elements of $\boldsymbol{y}$. The $c_{qk}$ and $c_{rl}$ terms are simply determined as needed from $c_{ij}$ in Eq. (3.14). In this case, $q$ and $r$ map to $i$, and $k$ and $l$ map to $j$. It is not necessary to perform the $q$ and $r$ summations in Eq. (3.15) over all $i$. The range of $q$ is restricted by the physically allowable $s_i$ for the particular $y_k$. Likewise, the range of $r$ is restricted by the physically allowable $s_i$ for the particular $y_l$. As a result of the properties demonstrated, the $\boldsymbol{V_s}$ covariance matrix for tabulated $S_{\mathrm{sym}}(\alpha, \beta)$ data makes up the only information necessary to fully determine covariances among all integrated and differential thermal scattering cross sections for all incident energies.

### 3.2.3 Establishing the Phonon Density of States as the Primary Random Variable in the Thermal Scattering Law

The task at hand is to develop a methodology for quantifying covariances among ENDF File 7 $S_{\text{sym}}(\alpha,\beta)$ data. The $S_{\text{sym}}(\alpha,\beta)$ parameters are clearly not "model parameters" in any traditional sense. They are neither free "adjustable" variables nor empirically based. The terminology has been borrowed rather loosely from the terminology of File 30 to emphasize the simplicity with which $\boldsymbol{V_s}$ can be propagated to fully describe $\boldsymbol{V_y}$, regardless of how $\boldsymbol{s}$ is defined or calculated. ENDF File 7 thermal libraries tabulate $S_{\text{sym}}(\alpha,\beta)$ data for specified $T$ over $\alpha$ and $\beta$ grids defined by the evaluator. The parameters $\alpha$, $\beta$ and $T$ in the thermal scattering law are also not traditional "model parameters." They are better described as selected points at which the scattering model is evaluated in $\alpha$, $\beta$ and $T$ space. In other words, the values of $\alpha$, $\beta$ and $T$ are arbitrary constants and affect only the *resolution* with which $\boldsymbol{s}$ is described based on a fixed scattering model.

Experimentally derived $S(\alpha,\beta)$ data is often scarce and may not exist for particular materials or at the temperatures desired. When experimental measurements are available, a comparison to the theoretical scattering law model may be made for verification and validation. Existing experimental $S(\alpha,\beta)$ data is usually limited in scope, covering only select $\alpha$ and $\beta$ points or insufficient ranges of $\alpha$ and $\beta$. As a result, the thermal scattering law data published in ENDF File 7 libraries is, by convention, theoretically calculated according to the incoherent inelastic scattering model and unadjusted. Consequently, the focus of the uncertainty analysis in this work will correspond to this theoretical methodology of calculating $S(\alpha,\beta)$.

Reviewing Eqs. (2.13) – (2.33), it is evident that, within the incoherent approximation, the fundamental parameter describing the thermal scattering law is $\rho(\varepsilon)$, the phonon density of states. Indeed, this is the only input to LEAPR providing information about the dynamic behavior of atoms within a material's molecular structure. The phonon DOS may be viewed as a probability density function of the population of atomic vibrational energy modes that exist in a material. It is typically defined pointwise over an evaluator-specified energy grid. There are many different procedures for estimating the DOS spectrum. Uncertainties associated with $\rho(\varepsilon)$ will depend on the particular methods employed to generate it and on any other information available about the true nature of $\rho(\varepsilon)$.

The parameters $T$, $A$ and $\sigma_\mathrm{b}$ are required information in the calculation of $S_\mathrm{sym}(\alpha,\beta)$. The thermal scattering law is calculated at a defined temperature which is considered to be exact. The uncertainty in the accepted values for $A$ and $\sigma_\mathrm{b}$ is usually far less than the uncertainty in $\rho(\varepsilon)$. Therefore, $S_\mathrm{sym}(\alpha,\beta)$ may be considered to be a function of a single random "parameter" – $\rho(\varepsilon)$. Consequently, within the incoherent inelastic scattering model utilized, describing uncertainties in the phonon DOS is a fundamental requirement for estimating $\boldsymbol{V_s}$ and $\boldsymbol{V_y}$.

## 3.3 A Framework for Describing Uncertainties in the Phonon Density of States

To begin analyzing and describing uncertainties in the phonon DOS, it is necessary to first have a mathematical construct with which these can be expressed. Since $\rho(\varepsilon)$ is not a single-valued variable, its uncertainty cannot be quantified in terms of a single probability distribution. The phonon DOS is itself a PDF and can be considered a function of many variables. In particular, it is generally defined as a normalized piecewise function over $D$ specified energy grid points, or energy bins. In this case, $\rho(\varepsilon)$ can be described by the parameters $p_d$, for $d = 1 \ldots D$, or by the parameter set $\boldsymbol{p}$. Figure 3.2 illustrates this parameterization of $\rho(\varepsilon)$ utilizing the low-energy region of the Young and Koppel phonon DOS spectrum for graphite [22] as an example. See Figure 2.3 for the full spectrum. Each $p_d$ represents the fraction of phonon modes in the material with energies that lie within the bounds of the $d^{\text{th}}$ energy bin.

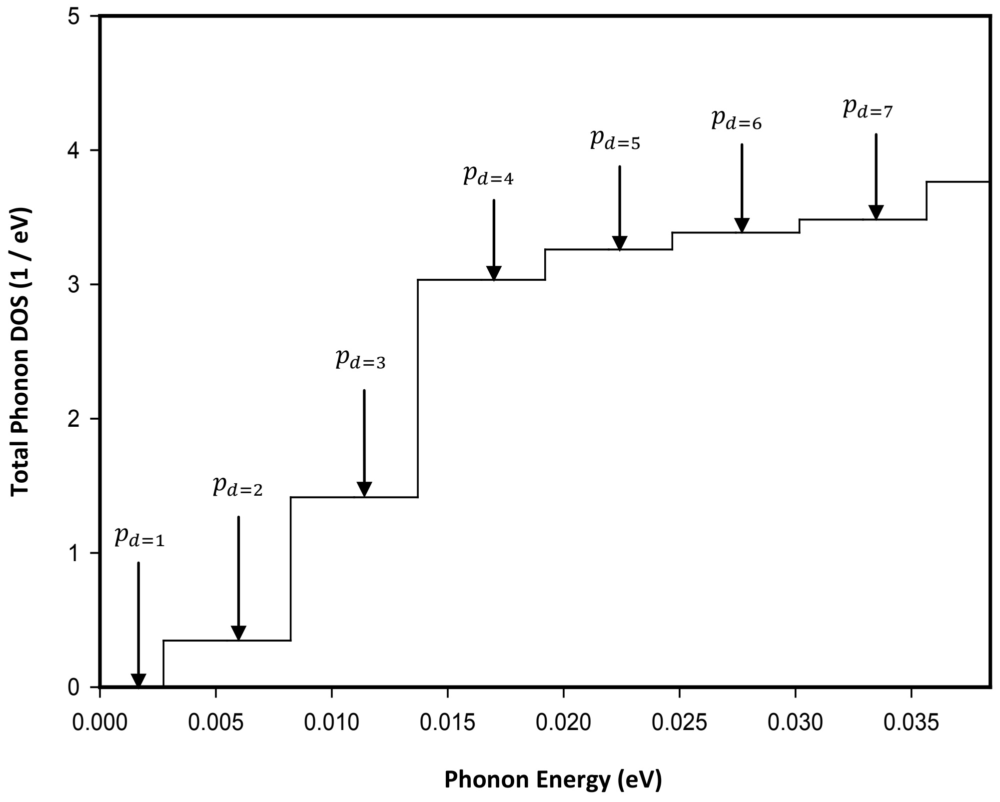

**Figure 3.2 Low-energy region of the Young and Koppel total phonon density of states for graphite [22] illustrating the parameterization of the $\rho(\varepsilon)$ spectrum.**

In general, the energy bin widths for $\boldsymbol{p}$ may be arbitrary. However, it is standard practice to use a uniform grid. Since this is also the input method for LEAPR, this line shall be followed and the $d^{\text{th}}$ energy grid point is considered to lie at the center of the $d^{\text{th}}$ energy bin (with the exception of $d = 0$ and $d = D$). The fixed energy bin width is represented by $p_{\text{int}}$. Furthermore, the restrictions $E(p_1) = 0$ eV, $E(p_D) = E_{\text{max}} = \hbar\omega_{\text{max}}$, $p_1 = 0$ and $p_D = 0$ are imposed for $\boldsymbol{p}$. For any method of arriving at the phonon DOS, the features of the DOS spectrum may be distorted and shifted to some extent in energy and magnitude with respect to the ideal DOS. To generalize, there are spectral shape uncertainties present in $\rho(\varepsilon)$. The vector $\boldsymbol{p}$ can be considered to be a set of $D$ random variables. In principle, there is a joint probability density function for $\boldsymbol{p}$ that fully describes these shape uncertainties (within the context of the given bin structure). Of course, this joint PDF will not be known explicitly. In theory, uncertainties in the shape of the $\rho(\varepsilon)$ spectrum can be described to first order by a covariance matrix for the parameter set $\boldsymbol{p}$, or by $\boldsymbol{V_p}$. However, there must be a clear path for quantifying $\boldsymbol{V_p}$. To determine how to proceed, the particular procedures and information employed in generating the $\rho(\varepsilon)$ spectrum must be investigated.

## 3.4 Describing Uncertainties in the Phonon Density of States Through Monte Carlo Sampling

### 3.4.1 Rationale for a Monte Carlo Approach

The phonon DOS for a material may be calculated using experimental methods, theoretical methods, or a combination of both. There is no standard process employed for generating the phonon DOS for the purpose of calculating the thermal scattering law. Several approaches are listed as examples. First, the DOS may be calculated based on experimentally measured phonon dispersion relations, or $\omega(\boldsymbol{q})$. Alternatively, the DOS may be calculated based on experimentally measured double-differential scattering cross sections. The DOS may also be calculated through a molecular dynamics simulation of the material structure. Finally, lattice dynamics in the harmonic approximation may be applied to calculate the DOS using some set of interatomic force constants. In the latter example, the necessary force constants may be arrived at by fitting to experimental thermodynamic data, or they may be calculated by a first-principles approach using density functional theory [18]. Other methods for calculating the phonon DOS exist as well.

For any methodology selected for determining $\rho(\varepsilon)$, both Type 1 and Type 2 uncertainties will likely exist. Type 2 uncertainties will almost invariably be of the greatest importance and require careful scientific judgment to model. When experimental measurements are involved, Type 2 uncertainties will generally consist of approximations and assumptions inherent in the interpretation and processing of the experimental data. For theoretical approaches to determining $\rho(\varepsilon)$, Type 2 uncertainties arise based on how well mathematical models reproduce the actual physics of a system.

In principle, one could attempt to quantify $\boldsymbol{V_p}$ through a covariance matrix and sensitivity matrix associated with underlying model/method parameters. In some specific cases this may be possible, such as when force constants in a theoretical model are fitted to experimental thermodynamic data. However, even in this case, the resulting $\boldsymbol{V_p}$ associated with these force parameters may describe only one aspect of uncertainty in the $\rho(\varepsilon)$ spectrum. Unfortunately, it will often be the case that the complex nature of the particular methodology used in determining the phonon DOS is not conducive to this parameter-based approach. It may be unclear how to quantify a covariance matrix for the underlying parameters and calculating the necessary sensitivity matrix may be problematic. Furthermore, it may not even be possible to identify or define appropriate model/method parameters.

By examining the particular methodology employed to produce the phonon DOS and any relevant experimental data, specific aspects of uncertainties in the shape of $\rho(\varepsilon)$ may be described by one or more functions of any number of the parameters $p_d$. For example, bounds may be established for the possible variation in magnitude of the DOS in a particular energy region while keeping features coupled. Alternatively, bounds may be established for the possible displacement of features in energy. This displacement may be energy-dependent or fixed. In any of these cases, a function may be defined which operates on $\boldsymbol{p}$ to apply random magnitude changes or energy shifts based on the established bounds. Any appropriate sampling scheme may be used (such as a flat or Gaussian distribution), and the bounds may be treated as absolute or as $1\sigma$ bounds as appropriate. Finally, statistical fluctuations in individual $p_d$ may be modeled based on appropriate probability distributions.

In this sense, any uncertainties in $\rho(\varepsilon)$ arising due to random effects or complicated systematic effects can, in theory, be reduced to geometric descriptions of the expected variation in the shape of the phonon spectrum. Furthermore, any information the evaluator possesses regarding the expected variation of the shape of the $\rho(\varepsilon)$ spectrum may be statistically modeled as a function of the random variable vector $\boldsymbol{p}$ through Monte Carlo sampling.

### 3.4.2 Formulating the Monte Carlo Problem

Any number of functions may be defined which operate on the parameters $p_d$ to describe specific aspects of uncertainty (Type 1 or Type 2) in the shape of the phonon spectrum. These reshaping functions, which will be called $R$-functions, can be thought of as specialized random number generators. Individual $R$-functions may operate on the parameters $p_d$ in a dependent or independent manner, but the $R$-functions must not be redundant in the representation of uncertainties. A few examples of possible $R$-functions relating to particular statistical and physical attributes of the phonon DOS are given. In each case, $\boldsymbol{p'}$ represents a modified, or perturbed, phonon DOS and $p'_d$ represents an individual perturbed $p_d$. In the second example, $d'$ represents the $d^{\text{th}}$ energy bin for a modified energy grid, where $E(d')$ is shifted with respect to $E(d)$. Also in the second example, $d'_{\text{high}}$ and $d'_{\text{low}}$ represent upper and lower interpolation points for the purpose of remapping the shifted spectrum back onto the original energy grid. In the third example, $\xi$ is a dimensionless sampling factor used to vary the value of $p'_d$ from $(p'_d)_{\min}$ to $(p'_d)_{\max}$ for each $d$ from $d_{\min}$ to $d_{\max}$.

---

$R_1$ := *Pointwise-independent magnitude shift with normal sampling defined by* $< p_d >= p_d$ *and* $\sigma_d = \sqrt{N \times p_{\text{int}} \times p_d}$.

$R_1(\boldsymbol{p}) = [R_1(p_d), d = 1 \dots D] = \boldsymbol{p}'$

```
for $d = 1 \dots D$,
    $\mathrm{PDF}(\, p'_d) = \dfrac{\exp\left(\frac{-\left(p'_d - p_d\right)^2}{2Np_{\mathrm{int}}p_d}\right)}{2\sqrt{2\pi N p_{\mathrm{int}} p_d}}$
    $p'_d = \mathrm{RAND}[\mathrm{PDF}(\, p'_d)].$
```

---

$R_2$ := *Spectrum energy shift as a linear function of energy with flat sampling defined by a minimum and maximum shift.*

```
$R_2(\boldsymbol{p}) = [R_2(p_d), d = 1 \dots D] = \boldsymbol{p}'$
$\mathrm{PDF}(E_{\mathrm{shift}}) = \frac{1}{E_{\mathrm{max}} - E_{\mathrm{min}}},\ E_{\mathrm{shift}} = E_{\mathrm{min}} \dots E_{\mathrm{max}}$
$E_{\mathrm{shift}} = \mathrm{RAND}[\mathrm{PDF}(E_{\mathrm{shift}})]$
for $d = 1 \dots D$,
    $E(d') = E(d) + \frac{d}{D} E_{\mathrm{shift}}$
for $d = 1 \dots D$,
    if $E(d) < E(D')$, then
        $d'_{\mathrm{low}}, d'_{\mathrm{high}} \equiv [E(d'_{\mathrm{low}}) \leq E(d) < E\left(d'_{\mathrm{high}}\right),\ d'_{\mathrm{high}} = d'_{\mathrm{low}} + 1]$
        $p'_d = \frac{E(d) - E(d'_{\mathrm{low}})}{\left(\frac{E(D) + E_{\mathrm{shift}}}{E(D)}\right) p_{\mathrm{int}}} \times \left(p_{d'_{\mathrm{high}}} - p_{d'_{\mathrm{low}}}\right) + p_{d'_{\mathrm{low}}}$
    else $p'_d = 0.$
```

---

$R_3$ := *Partial spectrum magnitude shift defined by pointwise-variable bounds with flat sampling.*

$R_3(\boldsymbol{p}) = [R_3(p_d), d = 1 \dots D] = \boldsymbol{p}'$

```
$\mathrm{PDF}(\xi) = 1,\ \xi = 0 \dots 1$
$\xi = \mathrm{RAND}[\mathrm{PDF}(\xi)]$
for $d = d_{\mathrm{low}} \dots d_{\mathrm{high}}$,
    $p'_d = \xi \times [(p'_d)_{\max} - (p'_d)_{\min}] + (p'_d)_{\min}$.
```

In $R_1$, independent statistical variations in the magnitudes of $p_d$ are modeled in the outputted $\boldsymbol{p}'$. This may be appropriate, for example, when the phonon DOS is calculated by sampling theoretical dispersion relations [26, 27]. In $R_2$, the entire spectrum is either compressed or stretched, with the maximum energy shift of $E_{\mathrm{shift}}$ occurring for $p_D$ and a minimum shift occurring for $p_1$. The same grid structure is retained and a new phonon DOS is outputted as $\boldsymbol{p}'$. To prevent upper truncation when $E_{\mathrm{shift}}$ is positive, the reference grid can be extended to energies beyond $E_{\max}$. This $R$-function could be used to model the effect of uncertainties in the lattice constants of a crystal. Alternatively, this $R$-function may be used to approximate phonon mode shifts in energy due to temperature-dependent anharmonic effects [17, 28]. In $R_3$, $\boldsymbol{p}'$ accounts for a specific energy region of the DOS that lies, with its features coupled, between lower and upper magnitude bounds described as a function of individual $p_d$. This may allow modeling the uncertainty in regions of the phonon DOS based on other calculated spectra (either theoretical or experimental) for the same material.

After the sequential application of all $R$-functions to $\boldsymbol{p}$ and renormalization, a perturbed phonon DOS spectrum, $\tilde{\boldsymbol{p}}$, is produced. The overlay of all $R$-functions, along with the renormalization condition, collectively defines an estimated joint PDF for $\boldsymbol{p}$. By repeated application of this process, or Monte Carlo sampling of the joint PDF for $N$ trials, a set of $N$ $\boldsymbol{\tilde{p}}$ vectors is generated. A covariance matrix $\boldsymbol{V_p}$ may then be constructed from this set by

$$\mathrm{COV}(p_i, p_j) = \frac{1}{N-1}\sum_{k=1}^{N}\left(\tilde{p}_{i_k} - \bar{\tilde{p}}_i\right)\left(\tilde{p}_{j_k} - \bar{\tilde{p}}_j\right), \tag{3.16}$$

where the index $k$ tracks individual Monte Carlo trials. Covariances will naturally arise as a result of the renormalization condition and the coupling of features of the DOS when describing shape uncertainties. It should be noted that the mean value of $\boldsymbol{\tilde{p}}$ predicted by the joint PDF for $\boldsymbol{p}$ will, in general, not be equivalent to $\boldsymbol{p}$. Therefore, $\boldsymbol{V_p}$ should properly be referenced to the Monte Carlo mean of the generated set of $\boldsymbol{\tilde{p}}$ vectors, $\boldsymbol{\bar{\tilde{p}}}$, and not to $\boldsymbol{p}$. In cases where $\boldsymbol{V_p}$ may be described through underlying model/method parameters with a known covariance and sensitivity matrix, the generation of $\boldsymbol{V_p}$ is first order, and the associated joint PDF can be treated as a multivariate normal distribution which may be sampled with respect to $\boldsymbol{p}$. This simply defines an $R$-function operating on $\boldsymbol{p}$. Therefore, there is no obstacle to combining this with other $R$-functions describing independent uncertainties based on information not captured by the model/method parameters. In such a case, the final $\boldsymbol{V_p}$ would again be referenced to $\boldsymbol{\bar{\tilde{p}}}$.

To describe uncertainties in $\boldsymbol{p}$, it is necessary to make scientific judgments about the sources and natures of the uncertainties and how this information translates geometrically to $\boldsymbol{p}$. Clearly, this is a Type B evaluation of uncertainty. The Monte Carlo approach of generating $\boldsymbol{V_p}$ with a set of $R$-functions provides a clear mechanism for accomplishing this task. The procedure is completely general and is not restricted to any particular method of producing the phonon DOS. Like any uncertainty analysis method, its success will depend on the quality of judgments made about underlying uncertainties. In particular, the evaluator must be able to define an appropriate set of $R$-functions which reflect the physics and methodologies involved in the production of the DOS as well as any other information available regarding the true shape of the $\rho(\varepsilon)$ spectrum.

## 3.5 Calculating Uncertainties in the Thermal Scattering Law

Given the covariance matrix for the phonon DOS, $\boldsymbol{V_p}$, it is straightforward to use the propagation of uncertainty formula given by Eq. (3.11) to calculate $\boldsymbol{V_s}$ as

$$\boldsymbol{V_s} = \boldsymbol{M}_{\boldsymbol{ps}}^{\mathrm{T}} \boldsymbol{V_p} \boldsymbol{M_{ps}}. \tag{3.17}$$

However, the sensitivity matrix $\boldsymbol{M_{ps}}$ would have to be numerically calculated by individually perturbing each $p_d$. While this is a straightforward process, note from Eqs. (2.20) – (2.25) that $S(\alpha, \beta)$ is not linear with respect to $\boldsymbol{p}$. Therefore, $S_{\mathrm{sym}}(\alpha, \beta)$ is not linear with respect to $\boldsymbol{p}$. Moreover, $\boldsymbol{V_p}$ captures only a linear functional dependence among the $p_d$. Although the use of Eq. (3.17) may well produce acceptable results, any loss of information at this stage of the uncertainty analysis is unnecessary. In particular, the intention is to directly calculate $\boldsymbol{V_y}$ from the elements of $\boldsymbol{V_s}$ per Eqs. (3.14) and (3.15). The assumption will be made at this point that $\boldsymbol{V_s}$ can be explicitly provided to the user to facilitate this. Issues related to the storage of large quantities of covariance data are addressed in Section 5.3.2.

The theoretical calculation of the thermal scattering law in the incoherent approximation is not computationally expensive. Therefore, the Monte Carlo approach can be continued to solve for $\boldsymbol{V_s}$ by generating a large set of $\tilde{\boldsymbol{s}}$ vectors from the Monte Carlo trials which generate

$\widetilde{\boldsymbol{p}}$. For each Monte Carlo trial $k$, the entire thermal scattering law $\tilde{\boldsymbol{s}}_k$ is determined from $\widetilde{\boldsymbol{p}}_k$ per Eqs. (2.16), (2.20), (2.22) – (2.25), (2.27), and (2.32). In fact, the calculation of $\boldsymbol{V_p}$ may be bypassed altogether if desired. Now, the elements of $\boldsymbol{V_s}$ are given by

$$\mathrm{COV}(s_i, s_j) = \frac{1}{N-1}\sum_{k=1}^{N}\left(\tilde{s}_{i_k} - \bar{\tilde{s}}_i\right)\left(\tilde{s}_{j_k} - \bar{\tilde{s}}_j\right), \tag{3.18}$$

and $\boldsymbol{V_s}$ is referenced to $\bar{\tilde{\boldsymbol{s}}}$. Accordingly, it is $\bar{\tilde{\boldsymbol{s}}}$ which would be provided in a final ENDF File 7 library.

Note that each calculated $\widetilde{\boldsymbol{p}}_k$ will have its own specific Debye-Waller factor $e^{-\alpha\lambda_k}$ associated with it, where $\lambda$ is defined per Eq. (2.16). Therefore, there will be a mean $\lambda$, or $\bar{\tilde{\lambda}}$, and a $\sigma(\lambda)$ associated with the collection of all $\widetilde{\boldsymbol{p}}$. While individual $\sigma(p_d)$ will have somewhat localized effects on $\sigma(\bar{\tilde{\boldsymbol{s}}})$ as a function of $\beta$, $\sigma(\lambda)$ will globally affect $\sigma(\bar{\tilde{\boldsymbol{s}}})$ as a function of $\alpha$. For low incident energies where one-phonon scattering is dominant and the average $\alpha$ is low, the particular $\sigma(p_d)$ will be dominant in determining differential and integrated cross section uncertainties. For very low $\alpha$, there is very little uncertainty in the Debye-Waller factor even if $\sigma(\lambda)$ is large. At incident energies high in the thermal energy range, multiphonon scattering is dominant and the average $\alpha$ is high. Therefore, $\sigma(\lambda)$ will be dominant in determining differential and integrated cross section uncertainties in this case. For high-order phonon scattering, the effects of individual $\sigma(p_d)$ are almost completely smoothed out.

The approach of producing the entire thermal scattering law and its covariance matrix by Monte Carlo sampling is similar to that used in the Total Monte Carlo (TMC) method for empirical nuclear model data [29]. In TMC, the nuclear model empirical parameters are sampled based on their covariance matrix or joint PDF, and each trial is used to produce an entire perturbed nuclear data library. The collective set of these libraries is incorporated to calculate uncertainties in system response parameters in a Monte Carlo transport code by separately solving for the response parameters for each Monte Carlo library. While in this work a large set of ENDF File 7 libraries is generated only for the purpose of determining $\boldsymbol{V_s}$, there is no obstacle, except for computing resources, to extending the Monte Carlo approach to a Monte Carlo transport code such as MCNP [30]. Each $\tilde{\boldsymbol{y}}_k$ library could be generated directly from $\tilde{\boldsymbol{s}}_k$ by Eq. (3.13). Indeed, this might be the most practical way to carry out a preliminary test of the impact of thermal neutron inelastic scattering uncertainties since there are presently no codes capable of directly processing and incorporating this uncertainty information.

Unless the intent is to proceed with the TMC approach for use in a transport code, there is no need to calculate the entire set of $\tilde{\boldsymbol{y}}_k$ vectors. The sensitivity constants $c_{ij}$ given by Eq. (3.14) are not impacted by perturbations in $\boldsymbol{p}$. Therefore, instead of calculating $\bar{\tilde{\boldsymbol{y}}}$ from the set of $\tilde{\boldsymbol{y}}_k$ vectors, $\bar{\tilde{\boldsymbol{y}}}$ can simply be calculated directly from $\bar{\tilde{\boldsymbol{s}}}$ via Eq. (3.13), except that $s_{a,b}$ is replaced by $\bar{\tilde{s}}_{a,b}$. A complete method for generating $\bar{\tilde{\boldsymbol{y}}}$ and $\boldsymbol{V_y}$ from $\bar{\tilde{\boldsymbol{s}}}$ and $\boldsymbol{V_s}$ is now at hand. Figure 3.3 displays a flowchart illustrating the entire *R*-function and Monte Carlo process from the initially supplied phonon DOS to the calculation of covariances for integrated and differential thermal neutron scattering cross sections.

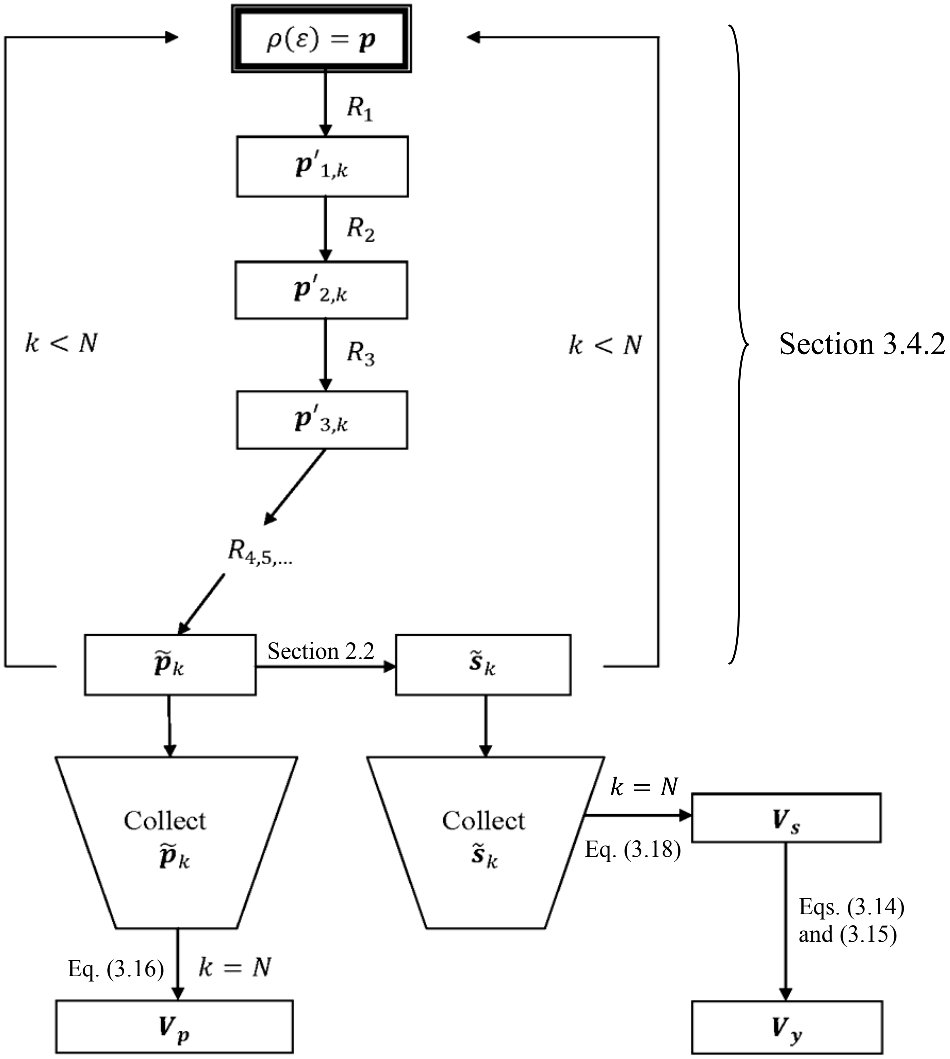

**Figure 3.3 Flowchart illustrating the *R*-function and Monte Carlo process of generating $V_p$, $V_s$ and $V_y$ from an input phonon DOS.**

### 3.5.1 A Special Case for One-Phonon Scattering

Since $S_1(\alpha,\beta)$ is essentially linear with respect to the phonon DOS, the DOS can be estimated by attempting to extract $S_1(\alpha,\beta)$ from experimentally measured $S(\alpha,\beta)$. Eq. (2.14) is restated to illustrate.

$$S_1(\alpha,\beta) = \frac{\alpha e^{-\alpha\lambda} e^{-\beta/2}\rho(\beta)}{2\beta\sinh(\beta/2)}. \tag{3.19}$$

This extraction process may involve correcting for and/or minimizing background, multiple scattering, multiphonon scattering, quasi-elastic scattering, etc. The incoherent approximation is also assumed in Eq. (3.19). In other words, any coherent interference contribution to the true $S_1(\alpha,\beta)$ is not considered.

The Debye-Waller factor may be assumed to be unity, since this will cause the estimate of $\rho(\beta)$ to be off by a fixed factor over all $\beta$, for fixed $\alpha$, which will be negated after normalization. The total phonon DOS is independent of $\alpha$, so a collection of extracted $S_1(\alpha,\beta)$ over an appropriate range of $\alpha$ may be used to improve statistics. If the extracted $S_1(\alpha,\beta)$ are the true $S_1(\alpha,\beta)$, then the calculated $\rho(\beta)$ will give the correct Debye-Waller factor for all $\alpha$ and will reproduce the measured $S(\alpha,\beta)$ for all $\alpha$ and $\beta$.

Of course, in reality, $\rho(\beta)$ can only be approximated by this method, notwithstanding the incoherent approximation. In particular, due to the imperfect extraction process, the extracted $S_1(\alpha,\beta)$ will generally not be independent of the incident $E$, and the $\rho(\beta)$ spectrum calculated from extracted $S_1(\alpha,\beta)$ will generally not be independent of $\alpha$. However, if the uncertainty in the calculated phonon DOS is appropriately modeled by the *R*-function and Monte Carlo methodology outlined, the extracted values for $S_1(\alpha,\beta)$ should be statistically consistent with the calculated $\bar{\bar{\boldsymbol{s}}}_1$ and $\boldsymbol{V}_{s_1}$, noting the relationship given by Eq. (2.32) for the symmetric thermal scattering law. This is a way to verify the modeling of *R*-functions against experimentally derived data and to gauge the accuracy with which $\rho(\beta)$ was calculated from the extraction process.

Conveniently, since $S_1(\alpha,\beta)$ is linear with respect to the DOS, $\boldsymbol{M_{ps_1}}$ can be expressed analytically as a set of constants in the same manner that $\boldsymbol{M_{sy}}$ can be expressed analytically as a set of constants. This allows an exact description of $\boldsymbol{V_{s_1}}$ as a function of $\boldsymbol{V_p}$, where

$$\boldsymbol{V_{s_1}} = \boldsymbol{M_{ps_1}^{\mathrm{T}}}\boldsymbol{V_p}\boldsymbol{M_{ps_1}}. \tag{3.20}$$

In this application, the details of $\boldsymbol{V_p}$ are not extraneous, but are fundamental in guiding the proper development of *R*-functions. Specifically, $\boldsymbol{M_{ps_1}}$ will be sparse, allowing very simple and easily interpretable analytical expressions for the terms of $\boldsymbol{\sigma}(\boldsymbol{s_1})$ as functions of at most two $\sigma(p_d)$ each. A full analysis of this analytical one-phonon case is given in Appendix C.

In conclusion, a practical note regarding this discussion should be mentioned. If the extracted $S_1(\alpha,\beta)$ are very poor estimates for the true $S_1(\alpha,\beta)$, the calculated phonon DOS will have little meaning and so will any attempt to describe its uncertainty. Fortunately, this situation should be readily apparent upon examination of the variation in the calculated $\rho(\beta)$ as a function of $\alpha$.

## 3.6 Comparison with Traditional Uncertainty Analysis

The great majority of currently published ENDF nuclear data covariances are associated with nuclear reactions (i.e., reactions involving excitations or changes in the structure of the nucleus itself). Specifically, most existing covariance evaluations focus on reactions in the resonance energy region. While there have been great improvements in understanding the nucleus and modeling nuclear phenomena, there is no comprehensive fundamental theory regarding nucleon-nucleon interactions or nuclear cross sections that is widely predictive [31, 32]. Successful empirical nuclear models have been developed to model particle interactions with nuclei in the resonance energy region. The quantification of parameters for these models has necessarily been guided by experimental measurements. The agreement of these models with new experimental data is often very good and predictive when interpolation is applied. However, the nuclear models can potentially fail when extrapolated to conditions where the empirical parameters have not been tuned to experimental data [23].

Most nuclear data evaluations involve, to some extent, fitting and/or adjustment of nuclear model calculations to experimental measurements. This is a formal mathematical process which generates a covariance matrix for the calculated data that reflects the fitting process. In some instances, very low uncertainties (< ~ 3%) are quoted in neutron cross section evaluations. Such low uncertainties may be called into question when they do not reflect the spread of experimental data, implying that the evaluated data is unadjustable [33]. The 3% threshold is the minimum uncertainty considered acceptable by CSEWG for non-thermal inelastic scattering cross sections based on current QA guidelines [34]. These unusually low uncertainties can result from several potential issues, including the accuracy of the empirical model, the least-squares fitting process, and scientific judgments made in estimating experimental uncertainties and correlations [35].

There is a growing demand for nuclear data for reactions and isotopes for which experimental measurements may be limited or nonexistent. In these cases, the data must be calculated directly from mathematical models without adjustment. Until around 2004, covariances for purely theoretically calculated data, such as for emission spectra in the unresolved resonance region, were rarely reported. It is now commonplace, with covariances reported in terms of the underlying empirical model parameters along with corresponding sensitivities [35].

The thermal scattering law $S_{\mathrm{sym}}(\alpha,\beta)$, or $\boldsymbol{s}$, is typically calculated theoretically as a function of the underlying parameter $\rho(\varepsilon)$, the phonon DOS, with no fitting or adjustment to experimental scattering law data performed. As discussed, there is precedent for publishing theoretically generated covariances. However, the theory of thermal neutron scattering is not empirical, and the phonon DOS can be independently calculated from fundamental principles or experimentally derived in numerous ways. Should the evaluator choose, coherent inelastic terms may also be calculated, either from fundamental principles or experimentally, and added to $S_{\mathrm{sym}}(\alpha,\beta)$ [19]. Because of this situation, uncertainties in experimentally measured $S_{\mathrm{sym}}(\alpha,\beta)$ may not be directly related to a $\boldsymbol{V_s}$ calculated as a function of uncertainties in the phonon DOS. It is certainly conceivable that the theoretical calculation of $\boldsymbol{s}$ may yield much smaller uncertainties than would be expected from experimental double-differential measurements, and that this result would be physically justifiable. Under these circumstances, the principal purpose of experimental $S_{\mathrm{sym}}(\alpha,\beta)$ data would be for verification and validation of the physics models employed.

Furthermore, it is conceivable that different theoretical evaluations of $\boldsymbol{s}$ using different $\boldsymbol{p}$ may lie significantly outside the $1\sigma$ range of uncertainty for a reference $\boldsymbol{s}$ and its associated $\boldsymbol{V_s}$. Although worth examining, this would not necessarily be problematic. Other evaluations may employ completely different methods for calculating the phonon DOS, and the uncertainties in those methods may differ considerably.

When experimental $S_{\text{sym}}(\alpha,\beta)$ is available, assuming good covariance information, it is conceivable that a theoretically evaluated $\boldsymbol{s}$, with an associated $\boldsymbol{V_s}$, could be incorporated to produce a new set of $S_{\text{sym}}(\alpha,\beta)$ that is adjusted to the experimental data by a least-squares methodology. However, experimental data may be more limited in the ranges and resolution of $\alpha$ and $\beta$ covered than a theoretical calculation. Furthermore, $S_{\text{sym}}(\alpha,\beta)$ represents a single physical scattering law tabulated at different points. Therefore, any adjustment should be made globally and maintain the physics of the entire scattering law. A global approach would be to modify $\boldsymbol{p}$, consistent with $\boldsymbol{V_p}$, to determine a best fit with the experimental $S_{\text{sym}}(\alpha,\beta)$ data. Limited resolution of the experimental data would present no difficulties. Such a procedure would be analogous to tuning empirical nuclear model parameters to provide a best fit to experimental data in the resonance energy region.

A complication arises when one considers that experimental $S_{\text{sym}}(\alpha,\beta)$ will have uncertainties in magnitude as well as in the quoted $\alpha$ and $\beta$. However, experimental $S_{\text{sym}}(\alpha,\beta)$ can often be considered to be of the form

$$S_{\text{sym}}(\alpha,\beta) = \frac{\int_{\beta_{\text{min}}}^{\beta_{\text{max}}} \int_{\alpha_{\text{min}}}^{\alpha_{\text{max}}} S_{\text{sym}}(\alpha,\beta)\, d\alpha d\beta}{(\beta_{\text{max}}-\beta_{\text{min}})(\alpha_{\text{max}}-\alpha_{\text{min}})}, \tag{3.21}$$

where the bounds for $\alpha$ and $\beta$ are reasonably well known based on detector characteristics, and $S_{\text{sym}}(\alpha,\beta)$ is considered the center point average over these narrow intervals. In this case, if $S_{\text{sym}}(\alpha,\beta)$ is considered to be sampled equally within the given bounds, any uncertainties in $\alpha$ and $\beta$ can be treated as a component of the magnitude uncertainty. In situations where the bounds for $\alpha$ and $\beta$ cannot be well described, the treatment of uncertainties and covariances may be seriously complicated.

## 3.7 Sources of Uncertainty External to the Phonon Density of States

Up to this point, it has been implicitly assumed that uncertainties in differential and integrated cross sections can be treated in the context of uncertainties in the phonon density of states. This path is taken because published ENDF File 7 $S_{\text{sym}}(\alpha,\beta)$ data is conventionally generated theoretically in the incoherent approximation with the input of a unique phonon DOS for each element type in the moderator material. In the development of the analytical form for the thermal scattering law, each assumption and approximation made was stated with some justification. At this point, it is appropriate to investigate more closely each source of uncertainty in the thermal scattering law (and in differential and integrated cross sections) which *cannot* be directly characterized through a description of uncertainties in the phonon DOS.

### 3.7.1 The Born Approximation and Fermi Pseudopotential

The development of thermal neutron scattering theory began with the expression for the double-differential cross section in Eq. (2.1). While its derivation is beyond the scope of this work, one need only assume the first-order Born approximation and Fermi pseudopotential to arrive at the given form.

Incident neutrons can be considered to be plane waves of the form

$$\psi_n(\boldsymbol{r}) = e^{i\boldsymbol{k}\cdot\boldsymbol{r}} \tag{3.22}$$

which then scatter with a fixed nucleus. In Eq. (3.22), $\boldsymbol{r}$ is a position vector with respect to the nucleus. The scattering radii $b$ for most nuclei are experimentally known to be on the order of $10^{-4}$ Å. The wavelength of a neutron in the extreme upper limit of the thermal energy region is on the order of $10^{-1}$ Å. Therefore, the scattering nucleus will be a pointlike particle with respect to incident thermal neutrons, and pure s-wave scattering applies.

Scattered neutrons can be treated as spherical waves of the form

$$\psi_{n'}(r) = f(\theta)\frac{e^{ikr}}{r}, \tag{3.23}$$

where $\theta$ is the scattering angle in the laboratory frame and $f(\theta)$ is the scattering amplitude. For $r \gg b$, the wave amplitude of $\psi_{n'}(r)$ is very small compared to that of $\psi_n(r)$. The distance between atoms in condensed matter is on the order of $10^0$ Å. Therefore, thermal neutron scattering can be considered to be a very weak process where the incoming plane waves are nearly unperturbed by the scattered spherical waves [16].

As a result, the system scattering wave function in the first-order Born approximation can be written

$$\psi(\boldsymbol{r}) = \psi_n(\boldsymbol{r}) + \psi_{n'}(r). \tag{3.24}$$

Although the true functional form of the scattering potential $V(\boldsymbol{r})$ is unknown, the only requirement is that it results in scattering that is isotropic with respect to a fixed nucleus. Because of the pointlike nature of the nucleus compared to incident neutron wavelengths, one can assume the potential to nearly be a δ-function about the nucleus. Indeed, applying the Fermi pseudopotential, or

$$V(\boldsymbol{r}) = \frac{2\pi\hbar^2}{m}\delta(\boldsymbol{r}), \tag{3.25}$$

gives the required result and also yields the familiar definition of the bound cross section for potential scattering, or

$$\sigma_{\mathrm{b}} = 4\pi|b|^2. \tag{3.26}$$

Therefore, defining the double-differential cross section per Eq. (2.1) is well justified [15].

### 3.7.2 The Nuclear Bound Cross Section and Atomic Mass Ratio

The nuclear bound cross section, $\sigma_{\mathrm{b}}$, and the scattering atom to neutron mass ratio, $A$, are physical quantities upon which $S_{\mathrm{sym}}(\alpha,\beta)$ depends. The uncertainty in $\sigma_{\mathrm{b}}$ is typically on the order of 1%. For natural carbon (which consists almost entirely of C-12), the uncertainty in $\sigma_{\mathrm{b}}$ is about 0.5% [13]. The uncertainty in $A$ is a function of the uncertainty in the mass of the scattering nuclide (or in the isotopically-averaged atomic weight) and in the mass of a neutron. Masses of naturally-occurring nuclides typically have uncertainties on the order of $10^{-9}$% – $10^{-5}$% (e.g., ~ $8\times10^{-9}$% for C-13) [36]. For certain elements, isotopically-averaged atomic weights can have spreads on the order of $10^{-3}$% – $10^{-1}$% between material samples due to natural and synthetic enrichment processes (e.g., ~ $2\times10^{-2}$% for carbon). For most elements, these enrichment effects are insignificant and the isotopic abundance uncertainties are orders of magnitude lower [37]. The mass (in amu) of a neutron is known to within about $4\times10^{-10}$% [38]. Therefore, the uncertainties in $S_{\mathrm{sym}}(\alpha,\beta)$ associated with the atomic mass ratio should be negligible.

### 3.7.3 Randomly Oriented Microcrystal Structure

Randomly oriented microcrystal structure is assumed in the definition of the thermal scattering law since the momentum transfer factor $\alpha$ is a scalar. This is not an approximation but is an assumed condition physically present in most nuclear engineering applications. In some situations, manufacturing processes may result in materials with preferentially-oriented grain boundaries. Just as if impurities or defects are present in the actual material, the effect of this lies outside the conventional definition of the scattering law. If a single oriented crystal is the scattering medium, the use of conventional ENDF File 7 thermal libraries may be inappropriate.

### 3.7.4 Coherent Interference in Inelastic Scattering

In the Monte Carlo method presented for determining $\boldsymbol{V_s}$, the incoherent approximation given by Eq. (2.7) has been presupposed. Neglecting the multiphonon $S_\mathrm{d}$ terms of Eq. (2.6) is of no concern. These will effectively be zero since the conservation of energy condition

$$\frac{\hbar^2}{2m}\left(k^2 - k'^2\right) = \hbar[\pm\,\omega(\boldsymbol{q}_1) \pm \omega(\boldsymbol{q}_2) \pm \cdots] \tag{3.27}$$

and the conservation of momentum condition

$$\boldsymbol{k} - \boldsymbol{k}' = \boldsymbol{\tau} \pm \boldsymbol{q}_1 \pm \boldsymbol{q}_2 \pm \ \dots\ , \tag{3.28}$$

where $\boldsymbol{\tau}$ is a discrete reciprocal lattice vector, can essentially always be met by some combination of phonon wave vectors $\boldsymbol{q}$. Therefore, no interference condition will arise [15]. However, ${}^1S_\mathrm{d}(Q,\omega)$ can be of significant magnitude and generally cannot be neglected if one is concerned with uncertainties in $S_\mathrm{sym}(\alpha,\beta)$ for particular $\alpha$ and $\beta$. Since $S_1(\alpha,\beta) = k_\mathrm{B}T[\,{}^1S_\mathrm{s}(Q,\omega) +\ {}^1S_\mathrm{d}(Q,\omega)]$ is coupled in energy and angle due to coherent interference effects, its uncertainty cannot be treated as a function of the phonon DOS only.

The ${}^1S(Q,\omega) = {}^1S_\mathrm{s}(Q,\omega) + {}^1S_\mathrm{d}(Q,\omega)$ term can be calculated from the dispersion relations $\omega(\boldsymbol{q})$ for all $Q$ and $\omega$ by analyzing spherical shells of fixed $Q$ magnitude in the first

Brillouin zone for fixed $\omega$. This calculation has been demonstrated for graphite [19] and other materials [39]. Next, $\boldsymbol{s}$ and $\boldsymbol{V}_s$ can be solved for *excluding one-phonon scattering* using the Monte Carlo methodology and then the $S_{\mathrm{sym},1}(\alpha,\beta)$ terms (which will include coherent one-phonon scattering) can be *added* to $\boldsymbol{s}$. As long as uncertainties and correlations for the $S_{\mathrm{sym},1}(\alpha,\beta)$ terms obtained from $\omega(\boldsymbol{q})$ can be represented, there is no obstacle to calculating a final $\boldsymbol{V}_s$ which accounts for both one-phonon and multiphonon scattering.

The determination of a covariance matrix for $S_{\mathrm{sym},1}(\alpha,\beta)$ calculated from $\omega(\boldsymbol{q})$ is beyond the scope of this paper. A similar Monte Carlo methodology may be well suited. It can be expected that cross-correlations between the $S_{\mathrm{sym},1}(\alpha,\beta)$ terms containing coherent one-phonon scattering and the multiphonon terms of $\boldsymbol{s}$ would generally not be strong for two reasons. First, if the methodologies for calculating the $S_{\mathrm{sym},1}(\alpha,\beta)$ terms from $\omega(\boldsymbol{q})$ and for generating the phonon DOS are unrelated, there will be no cross-correlations. If they are related, it is still the case that the multiphonon terms of $S_{\mathrm{sym}}(\alpha,\beta)$ are generally insensitive to the structure of the phonon DOS which will be closely tied to the structure of $\omega(\boldsymbol{q})$.

Even if ${}^1S_{\mathrm{d}}(Q,\omega)$ can be accounted for in this manner, it may not be necessary to do so. For reactor analysis and criticality safety applications, the quantities of interest are typically differential cross sections in energy and integrated cross sections, not the double-differential cross sections specifically. As discussed in Section 2.1, the impact of ${}^1S_{\mathrm{d}}(Q,\omega)$ is significantly lessened when considering differential cross sections in energy (after averaging over $Q$), and ${}^1S_{\mathrm{d}}(Q,\omega)$ is further marginalized when considering integrated inelastic cross sections. For graphite, however, the effect of ${}^1S_{\mathrm{d}}(Q,\omega)$ on the integrated cross section is unusually pronounced and, at room temperature, can be in the vicinity of +10% at incident energies below 0.5 meV to -5% at incident energies between 10 and 100 meV [17, 19]. For most applications, only the upper energy band is relevant. At higher temperatures, the effect is lessened as one-phonon scattering becomes less prominent.

### 3.7.5 Anharmonicities

Another assumption made in the development of thermal neutron scattering theory is that the vibrational displacements of atoms from their equilibrium positions are small and that, consequently, the interatomic forces acting on them are purely harmonic. This is essentially equivalent to assuming that no phonon-phonon scattering interactions take place, and it allows the analytical expression of the thermal scattering law in terms of a phonon expansion.

Figure 3.4 gives a schematic of the interatomic potential as a function of separation distance. At very small separation distances, there is a strong repulsive force as the electron clouds move into close proximity. There is an ideal equilibrium separation distance with a potential well that is nearly parabolic about the equilibrium point. As the distance from the equilibrium point increases, the restoring forces become less and less harmonic, and eventually the atomic bond is severed. An atom oscillating with a specified amplitude in energy will always have a mean position slightly offset from the equilibrium position, $r_{\text{eq}}$, due to the anharmonicity of the restoring force. This anharmonicity is responsible for thermal expansion as well as for finite thermal conductivity and other physical properties [40]. Anharmonic forces become particularly important at high temperatures, where the occupation number for higher-energy phonons becomes significant, or at temperatures near a phase transition for the material.

The potential $V(r)$ can be Taylor-expanded about $r = r_{\mathrm{eq}}$ to the form

$$V(r) = V(r_{\mathrm{eq}}) + \frac{\partial V}{\partial r}\Big|_{r=r_{\mathrm{eq}}}(r - r_{\mathrm{eq}}) + \frac{1}{2}\frac{\partial^2 V}{\partial r^2}\Big|_{r=r_{\mathrm{eq}}}(r - r_{\mathrm{eq}})^2 + O(r^3). \tag{3.29}$$

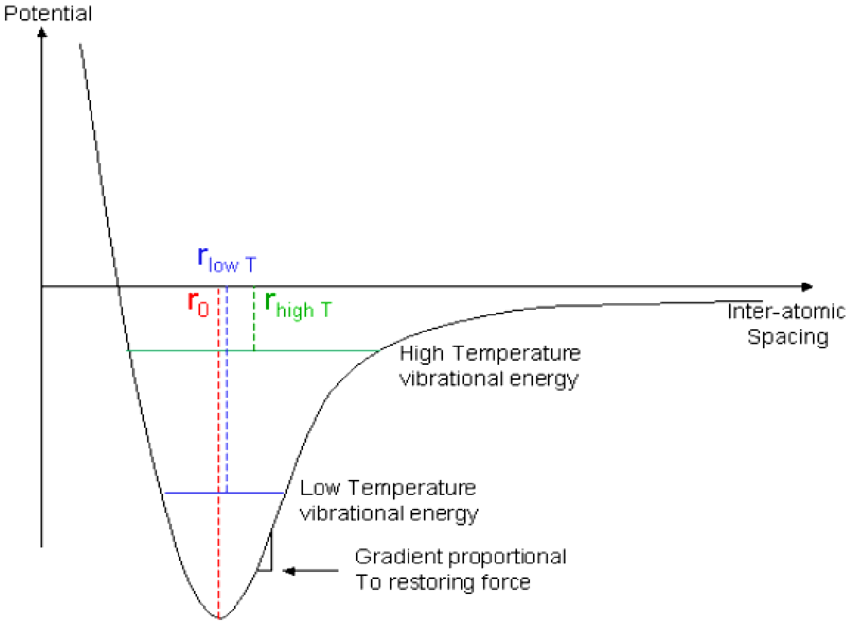

**Figure 3.4 Schematic of the interatomic potential as a function of separation distance.**

The zero-order term gives the potential well depth. The first-order term is always zero unless the expansion is written with respect to $r \neq r_{\mathrm{eq}}$. The second-order term contains the force constants for a harmonic oscillator, allowing the calculation of phonon frequencies from a dynamical matrix [41]. Third-order and higher terms result from phonon-phonon scattering. Physically, in a three-phonon process, a particular phonon oscillation will induce a periodic strain in space and time, perturbing the interatomic forces and elastic properties of the crystal. A second phonon perceives and scatters with the periodic oscillations, generating a third phonon of combinatorial energy [40].

Phonon-phonon interactions modify the phonon frequencies such that

$$\omega(\boldsymbol{q}) = \omega_{\text{harmonic}}(\boldsymbol{q}) + \Delta\omega(\boldsymbol{q}) + i\Gamma\omega(\boldsymbol{q}). \tag{3.30}$$

The term $\Delta\omega(\boldsymbol{q})$ represents a frequency shift (or energy shift) in the phonon mode that depends on changes in the lattice parameters as a function of temperature and on the sensitivity of each $\omega(\boldsymbol{q})$ to changes in the unit cell volume. In general, the phonon spectrum shifts downward in energy with increasing temperature, though not necessarily uniformly, and the highest energy phonons will generally be subject to the greatest spectral shift. The term $i\Gamma\omega(\boldsymbol{q})$ represents a spectral broadening of the phonon mode resulting from a finite lifetime of interacting modes. As phonon-phonon (or phonon-electron) scattering takes place, phonons will transfer their energy away and decay. Note that the anharmonic effects on the total phonon DOS are the combined result of shifting and broadening each phonon mode $\boldsymbol{q}_m$ [28]. Therefore, the effects cannot be described in terms of frequency (or energy) alone. There are theoretical methods available for calculating or estimating these effects, such as low-order perturbation theory, molecular dynamics or the quasiharmonic approximation, and the effects can also be experimentally measured. Although this would allow capturing anharmonicity in the phonon DOS, the phonon expansion method itself for calculating the thermal scattering law is strictly valid only when phonon-phonon scattering does not take place.

The influence of anharmonicity is often negligible except at relatively high temperatures. This is indeed the case for graphite, the example material investigated in this work.

Referring to the works of Bonini et al. [42] and Giura et al. [43], the energy shift of the Raman-active and IR-active peak near 200 meV (near $E_{\max} = \hbar\omega_{\max}$) in the phonon DOS for graphite (this peak is not represented well in the YK [22] spectrum in Figure 2.3) is less than 0.5 meV at 300 K. This is typically less than the resolution in which $\rho(\varepsilon)$ is given. At 800 K, the shift is in the neighborhood of 1.5 – 2.5 meV. Referencing the work of Paulatto et al. [44], the broadening (full-width half-maximum) of the phonon spectrum for graphite is shown to be almost universally less than 1 meV at 300 K. If the thermal scattering law is to be computed for graphite at temperatures well above 300 K, incorporating a temperature-specific phonon DOS that accounts for anharmonic shifting and broadening would produce the best results within the limitations of the phonon-expansion method used.

### 3.7.6 Directional and Momentum Dependence of the Phonon Energy Spectrum

The Debye-Waller factor is a function of the mean square displacement of an atom. It is defined as $e^{-2W}$, where $W$ is, in general, a function of $\boldsymbol{Q}$ and of all phonon modes $\boldsymbol{q}_m$. In the formulation of the thermal scattering law given, it has been assumed that the Debye-Waller factor is isotropic, or of the form $e^{-\alpha\lambda}$ given in Eqs. (2.15) and (2.16), and that a unique phonon DOS, the total DOS, is applicable to all $S(\alpha, \beta)$. In other words, it is assumed that the directional distribution of atomic vibrations is unnecessary information in calculating the thermal scattering law, as is any information regarding the magnitudes of the phonon wave vectors $\boldsymbol{q}$.

For an oriented non-cubic crystal, the Debye-Waller factor is clearly not isotropic, since the mean square displacement of atoms will vary with the lattice vector. If randomly oriented microcrystal structure is assumed, the Debye-Waller factor will always be isotropic. However, even in this case, the orientation-averaged phonon spectrum will still be a function of the *magnitude* of $\boldsymbol{Q} = \boldsymbol{q} \pm \boldsymbol{\tau}$, or of $\alpha$, even for cubic crystals, since $Q$ and $\omega$ are coupled in ${}^{1}S(Q,\omega)$ which directly corresponds to the phonon dispersion relations $\omega(\boldsymbol{q})$. If ${}^{1}S_{\mathrm{d}}$ is neglected, which has been argued to be valid in many cases from an application standpoint, then the phonon spectrum becomes independent of $\alpha$.

Even in incoherent scattering, there is still a directional distribution of atomic vibrations, but this effect is eliminated when scattering with randomly oriented microcrystal structure is considered. For a cubic crystal, the phonon spectrum and Debye-Waller factor are isotropic whether or not an orientation average is taken. The terms $2W$ and $\lambda$ for a cubic crystal can be expressed in analytical form with respect to the total phonon DOS per Eqs. (2.12) and (2.16), respectively, and these equations hold true regardless of whether the incoherent approximation is invoked. Therefore, the use of Eq. (2.12) or Eq. (2.16) is justified to calculate the Debye-Waller factor for *any* crystal lattice as long as one assumes randomly oriented microcrystal structure. Moreover, if the additional assumption is made that the incoherent approximation is valid, all $S_{\mathrm{sym}}(\alpha,\beta)$ can be considered to be a function of the total phonon density of states only. Finally, these arguments hold regardless of the number of atoms per unit cell.

### 3.7.7 Unit Cells with Multiple Basis Positions of Unique Symmetry

In the previous section, the use of only the total phonon density of states to calculate the thermal scattering law was justified (with conditions). Care must be taken to clarify how the total phonon DOS should be defined. Thus far, scattering in a material with one atom (or basis position) per unit cell has been considered. Most materials have more than one atom per unit cell or even more than one chemical element. Each basis position in a unit cell that is *unique by symmetry* will have a unique interatomic potential function associated with it which will depend on its particular surrounding neighbors. Therefore, there is a unique phonon DOS for each unique basis position.

In the case of a unit cell with two basis positions populated by different chemical elements, it is clear that the total phonon DOS must be specified for each. Then, $S_{\text{sym}}(\alpha, \beta)$ and cross sections can be calculated separately for each element or combined to represent a stoichiometric unit. When there is more than one unique basis position for a particular chemical element, the conventional methodology is to specify a single total phonon DOS that is averaged over the basis positions for that element. This is the methodology employed by LEAPR, although it is not strictly correct. The resulting $S_{\text{sym}}(\alpha, \beta)$ and cross sections will generally not be the same as those calculated by properly specifying a unique phonon DOS for each basis position, but they can be very similar in some cases. Uncertainties in $S_{\text{sym}}(\alpha, \beta)$ arising from the use of the conventional method cannot be quantified through a description of uncertainty in the averaged phonon DOS. This is because there is no single phonon DOS that is "correct" by itself in this situation. Rather, two or more distinct spectra should be provided, each with its own unique Debye-Waller factor. It is straightforward to compare the results of the two methods side-by-side and qualitatively determine whether the conventional method is acceptable. If not, there is no obstacle to using the exact method.

### 3.7.8 Phonon Expansion Order

When incorporating the phonon expansion method given in Section 2.2 to calculate $S_{\text{sym}}(\alpha,\beta)$, a phonon expansion order must be selected. The convention is to calculate $S_{\text{sym}}(\alpha,\beta)$ to phonon order $n = 100$. This is sufficient for determining integrated inelastic cross sections up to about 4 eV with extremely high accuracy. For incident energies higher than this, a rapid increase in the required phonon order is required to achieve convergence with the free cross section. If integrated cross sections are only required to be calculated at significantly lower energies, there is a substantial reduction in the necessary phonon order. In fact, for incident energies in the vicinity of $k_{\text{B}}T$, one-phonon scattering is usually dominant. It is rarely of interest to calculate thermal inelastic cross sections above 5 eV. Furthermore, once incident energies are sufficient to cause nuclei to sever their atomic bonds, the phonon expansion is no longer physically meaningful.

### 3.7.9 Material Structure Uncertainties

It is implicitly assumed that the phonon DOS incorporated is associated with a known material structure. In other words, it is not considered that the actual material structure the phonon spectrum represents may be different from that which it is purported to represent. Although difficult to address, this situation could potentially arise. For instance, a phonon DOS could be experimentally determined for a material that has significant unknown impurities or unknown lattice damage. Conversely, the structure of an actual material may not be well understood and a phonon density of states could be theoretically generated for a crystal structure which is not representative of the actual material being modeled.

### 3.7.10 Resolution of the Phonon Density of States and the Thermal Scattering Law

Finally, the $R$-function and Monte Carlo method of describing uncertainties in the phonon density of states is only applicable within the context of the energy bin resolution with which $\rho(\varepsilon)$ is provided. The information contained within a $p_d$ energy bin is already an average for all phonon modes with energies lying within the bin. Any information internal to the bins can neither be extracted once a particular reference $\rho(\varepsilon)$ is established nor expressed in terms of the given $p_d$. To recover any of this information, the methodology involved in producing the reference phonon spectrum would have to be modified.

When differential and integrated cross sections are calculated from the thermal scattering law, they are determined by integrating over $S_{\text{sym}}(\alpha,\beta)$ data points which lie on an established grid with finite resolution. In the limit of infinitely fine $\alpha$ and $\beta$ grids, the calculation of cross sections will converge. In practice, the evaluator must select particular $\alpha$ and $\beta$ grids, balancing computational expense, storage requirements and accuracy. The choice of these grids is by no means arbitrary. In particular, a poor choice of a $\beta$ grid may miss sampling vital details of the structure of the phonon spectrum and result in significant problems with calculated cross sections. In theory, this Type 2 grid uncertainty may be modeled using a Monte Carlo sampling of grid selections. Alternatively, the grid resolutions could simply be increased until acceptable convergence of the calculated differential and integrated cross sections is observed.

# Chapter 4

# Demonstrating the Monte Carlo Method for Calculating Thermal Scattering Uncertainties

## 4.1 A Material Basis for the Uncertainty Analysis: Graphite

Graphite has been in continuous use in nuclear reactors since the world's first nuclear reactor, Chicago Pile 1, was built in 1942 by Enrico Fermi [45]. It is attractive as a thermal neutron moderator, reflector and construction material for many reasons. Graphite has a low neutron absorption cross section, carbon atoms have low mass (making them efficient at slowing down neutrons), and graphite has good thermal and mechanical properties over the range of temperatures expected in nuclear reactor operations. Reactor grade graphite is specially manufactured to maintain dimensional stability under irradiation and over a large range of temperatures. Due to the manufacturing process, reactor grade graphite can vary in structure and porosity. In general, it is composed of randomly oriented crystallites interspersed in an amorphous-like carbon matrix, and its density can range from 1.5 – 1.8 g/cm$^3$ with a porosity as high as 30% [19, 46]. In addition to reactor grade graphite, the material graphite has numerous forms, both natural and artificial, differing greatly in structure.

The primary scope of this work is to examine and demonstrate procedures for calculating uncertainties in theoretically generated inelastic thermal scattering law data, or $S(\alpha,\beta)$, published in ENDF File 7 libraries as well as in the resulting differential and integrated cross sections. In this context, hexagonal (ABAB-stacked) crystalline graphite (with randomly oriented microcrystals) will be used as the example material. The choice of this form of graphite as a demonstration material is for several reasons. First, it is a layered material with highly anisotropic interatomic forces. This will serve to illuminate key physical aspects of its phonon density of states that are integral in the treatment of its uncertainties. Second, single-crystal hexagonal graphite is a thoroughly studied material for which there is a great of amount of information, both experimental and theoretical.

Currently published ENDF File 7 $S(\alpha,\beta)$ data is produced in the incoherent approximation for a *specific* material structure with a single total phonon DOS applied for all temperatures for each chemical element in the material, and the same will be assumed in demonstrating the Monte Carlo methodology. Uncertainties will be examined in this context and a systematic approach will be demonstrated for their calculation – using the hexagonal graphite structure and the physics models employed in this work as an example basis. Uncertainties due to unknown variations in an actual graphite structure (such as impurities, dislocations, cracks, and other lattice irregularities) are not considered.

For graphite, is has been mentioned that the ${}^{1}S_{\mathrm{d}}$ interference term of the dynamic structure factor cannot be strictly neglected, even for integrated cross sections, as it can be for many other materials. The ability to separately calculate ${}^{1}S_{\mathrm{d}}$ from dispersion relations has been demonstrated for graphite [17, 18, 19], and this methodology (as well as others) is applicable to any material. Therefore, the exclusion of ${}^{1}S_{\mathrm{d}}$ in the incoherent approximation does not detract from the utility of treating uncertainties in the thermal scattering law as a function of uncertainties in the total phonon density of states. Hence, the intent of this work is not to generate a final set of "evaluated" covariances that is application-ready, but to propose and demonstrate a generalized Monte Carlo method for their determination that is consistent with the standard method for calculating $S(\alpha, \beta)$ from $\rho(\varepsilon)$ in published ENDF File 7 libraries. Moreover, the particular sensitivities of the thermal scattering law, differential cross sections and integrated cross sections to characteristic uncertainties in the phonon DOS will be highlighted.

## 4.2 The Structure of Hexagonal Graphite

Hexagonal graphite is a layered material consisting of stacked planes of $sp^2$-bonded carbon atoms on a Bravais hexagonal lattice. The in-plane covalent bonds are very strong with a bond length of only 1.42 Å at 300 K. In contrast, the spacing between planes is large – 3.35 Å at 300 K – and the planes are only weakly bound by Van der Waals forces. The unbonded carbon atom valence $\pi$-electron is free to oscillate perpendicular to the plane. Hexagonal graphite is associated with an ABAB stacking sequence. Rhombohedral graphite has an ABCABC stacking sequence. This form is thermodynamically unstable and only occurs in small fractions mixed with ABAB-stacked graphite. Figure 4.1(a) shows the planar stacking structure and a representative parallelepiped unit cell for hexagonal graphite. Its density is 2.26 g/cm$^3$ at 300 K. There are four atoms per unit cell, and this basis set of four atoms is associated with one lattice site [17]. Only two of the basis positions are unique by symmetry. A-type carbon atoms are defined as those with neighboring atoms directly above and below in adjacent planes, while B-type carbon atoms are centered in the middle of adjacent-plane hexagons. Figure 4.1(a) shows the A-type and B-type basis positions and Figure 4.1(b) provides a vertical view.

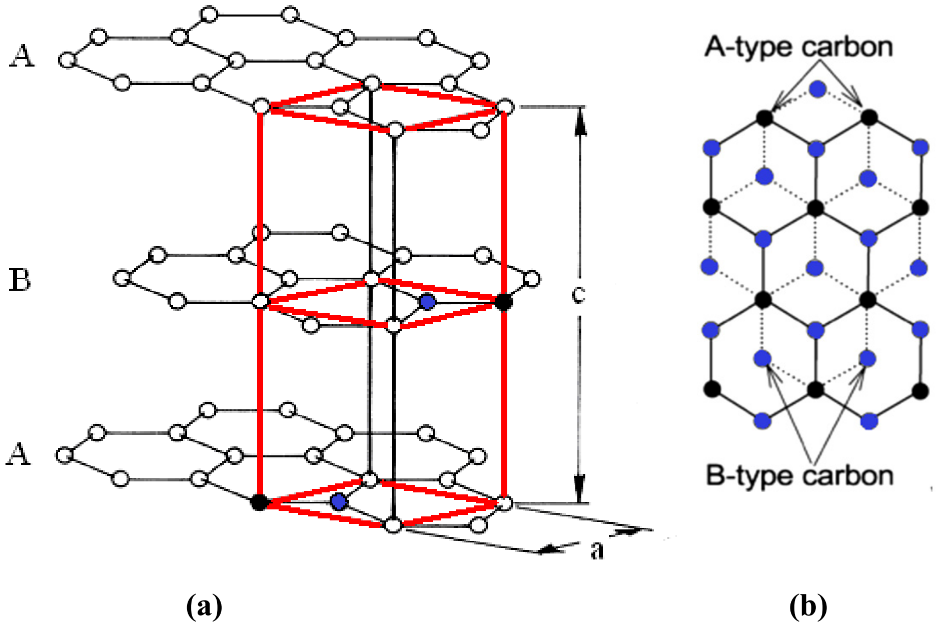

**(a)** **(b)**

**Figure 4.1 Left panel (a): Hexagonal ABAB-stacked graphite planar structure. A unit cell is outlined in red with dimensions $a = b = 2.46$ Å and $c = 6.71$ Å at 300 K. The four basis positions are shown. Black carbon atoms are A-type and blue carbon atoms are B-type. Right panel (b): Top view of ABAB-stacking. Atoms are A-type (black) and B-type (blue).**

Figure 4.2(a) gives a two-dimensional view of the unit cell and the lattice vectors $\boldsymbol{a}$ and $\boldsymbol{b}$. Note that only half of the carbon atoms in a plane can lie on lattice sites, and only every other carbon plane contains lattice sites. The lattice vectors $\boldsymbol{a}$ and $\boldsymbol{b}$ are defined to be separated by the angle $\gamma = 60°$, while all other angles in the parallelepiped are 90°. The lattice vector magnitudes for graphite at 300 K are $a = b = 2.46$ Å and $c = 6.71$ Å, where $c$ is twice the interplanar distance. The in-plane lattice vector translations into reciprocal space, given by $\boldsymbol{a}^*$ and $\boldsymbol{b}^*$, are shown in Figure 4.2(b) along with points of high symmetry in reciprocal space. In Figure 4.2(b), note that reciprocal lattice sites are defined at each Γ-point. The $x$, $y$ and $z$ Cartesian directions given in Figure 4.2(a) will be considered to also apply to reciprocal space.

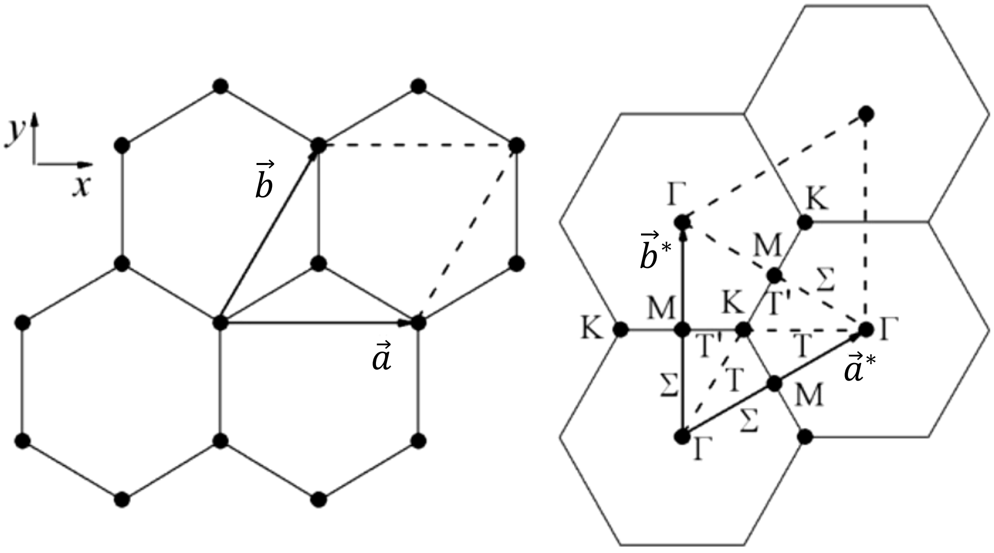

(a) (b)

**Figure 4.2 Left panel (a): Two-dimensional view of the graphite hexagonal lattice with lattice vectors $\vec{a}$ and $\vec{b}$ shown. The lower planar boundary of the unit cell is completed by dashed lines. Right panel (b): Two-dimensional view of the graphite reciprocal lattice (defined by Γ-points) with reciprocal lattice vectors $\vec{a}^*$ and $\vec{b}^*$ shown. Points of high symmetry for a hexagonal reciprocal lattice are labeled.**

Figure 4.3 displays a three-dimensional view of the hexagonal first Brillouin zone in reciprocal space with points of high symmetry labeled. An irreducible section is shaded. The magnitudes of the vectors $\overrightarrow{\Gamma A}$, $\overrightarrow{\Gamma M}$ and $\overrightarrow{\Gamma K}$ are given by

$$|\overrightarrow{\Gamma A}| = \frac{\pi}{c}, \; |\overrightarrow{\Gamma M}| = \frac{2\pi}{a\sqrt{3}}, \; |\overrightarrow{\Gamma K}| = \frac{4\pi}{3a}. \tag{4.1}$$

The first Brillouin zone is a primitive cell containing one lattice site in reciprocal space at its center (the Γ-point). The volume enclosed by points in reciprocal space that lie closer to a reference reciprocal lattice site than to any other reciprocal lattice site defines the first Brillouin zone. It is the reciprocal space analog of the Wigner-Seitz primitive cell. The

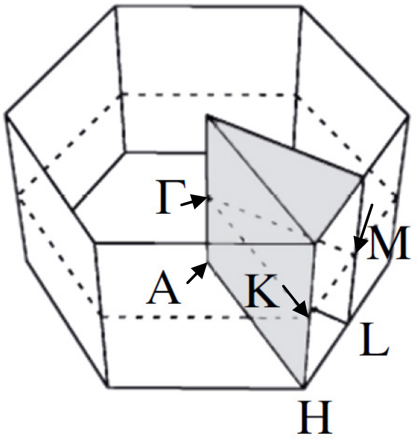

**Figure 4.3 Schematic of the hexagonal first Brillouin zone with an irreducible section shaded and points of high symmetry labeled.**

reciprocal lattice vectors are bisected by perpendicular planar boundaries of the first Brillouin zone.

Any wave vector $\boldsymbol{k}$ originating from the Γ-point that terminates on a boundary of the first Brillouin zone will satisfy the condition for diffraction, or the Bragg condition

$$2\boldsymbol{k} \cdot \boldsymbol{\tau} = \tau^2. \tag{4.2}$$

For an infinite crystal, all locations in the first Brillouin zone are allowed values for $\boldsymbol{k}$. For a finite crystal, $\boldsymbol{k}$ must satisfy periodic boundary conditions. Without loss of generality, the crystal may be considered to be infinite. The range of independent $\boldsymbol{k}$ is bounded by the first Brillouin zone. For all $\boldsymbol{k}$ lying outside the first Brillouin zone, $\boldsymbol{k} = \boldsymbol{k} - \boldsymbol{\tau}_{\boldsymbol{k}}$, where $\boldsymbol{\tau}_{\boldsymbol{k}}$ is the discrete reciprocal lattice vector $\boldsymbol{\tau}$ nearest to $\boldsymbol{k}$. Due to periodicity, information in the first Brillouin zone can describe all of the physics of the crystal. Moreover, due to symmetry, the irreducible section of the first Brillouin zone shown in Figure 4.3 is actually sufficient [40]. The phonon modes $\boldsymbol{q}_m$ available in the crystal populate the first Brillouin zone according to the dispersion relations $\omega(\boldsymbol{q})$, which depend on the interatomic potentials. Therefore, for the neutron scattering wave vector $\boldsymbol{Q} = \boldsymbol{k} - \boldsymbol{k}'$, both the conditions $\boldsymbol{Q} = \boldsymbol{\tau} \pm \boldsymbol{q}_1 \pm \boldsymbol{q}_2 \pm \ldots$ and $\frac{\hbar^2}{2m}\left(k^2 - k'^2\right) = \hbar[\pm\,\omega(\boldsymbol{q}_1) \pm \omega(\boldsymbol{q}_2) \pm \cdots]$ must be met [15]. As discussed in Sections 2.1 and 3.7.4, the former is only restrictive for one-phonon scattering.

Due to the anisotropy of the interatomic forces, graphite has very distinct in-plane and out-of-plane material properties. Since the number of stacked planes has little influence on in-plane forces, the in-plane material properties of graphite are very similar to those for single-plane graphene. For graphite, the phonon density of states can be separated into two directional partials, or

$$\rho_{\text{tot}} = \rho_{\parallel} + \rho_{\perp}, \tag{4.3}$$

which are characteristic of the distinct in-plane and out-of-plane interatomic forces in its layered structure.

Weak interplanar forces readily allow for planar translation and rotation. Manufacturing large crystals of perfect single-crystal graphite is difficult. Highly oriented pyrolytic graphite (HOPG) refers to graphite with a very low angular spread among planes about the *c*-axis. It is generally highly pure and exhibits the highest degree of three-dimensional symmetry. This is commonly the single-crystal form of graphite examined in experimental measurements. In general, the numerous forms of graphite all possess very similar structure on a nano-scale level. On a micro-scale to bulk level, different forms of graphite reflect varying degrees of interruption of the fundamental ABAB-stacked structure. These imperfections may include stacking faults, plane rotations, misoriented crystallites, dislocations, impurities, local sp$^3$-hybridization, porosity, etc.

## 4.3 Generation of the Phonon Density of States with Density Functional Theory and Lattice Dynamics in the Harmonic Approximation

The phonon density of states for graphite is generated using the *ab initio* density functional theory code VASP [47, 48, 49] and the lattice dynamics code PHONON [26, 27]. The selection of parameters in VASP and PHONON and the procedures followed were guided by the previous work of Al-Qasir [17]. In addition to the considerations of physics given by Al-Qasir in the VASP/PHONON process, the present work focused on issues of uncertainty in the VASP/PHONON process in determining a final phonon density of states for graphite to be used as a reference basis for the uncertainty analysis. The "best-estimate" outputs of VASP/PHONON in the work of Al-Qasir and in the present work are similar but not identical. In particular, the final phonon DOS presented for graphite in the two works differs in physically important ways from an uncertainty perspective. Henceforth, the term "reference" will refer to the "best-estimate" VASP/PHONON output in the *present* work, to the final basis phonon DOS for graphite generated directly from it, and to any subsequent calculations directly utilizing this information without modification.

The uncertainty analysis for graphite in the present work will depend on the physics of the structure of graphite as well as on the details of the VASP/PHONON methodology. For a review of the physics models and algorithms incorporated by VASP and PHONON in the context of the present work on graphite, see Appendix D. For additional details, the reader is referred to Ref. [17].

### 4.3.1 The Reference Phonon Density of States

Applying the cubic approximation for randomly oriented microcrystal structure, a single total phonon density of states, $\rho(\omega)$, is calculated by summing the partial phonon DOS associated with each Cartesian vector generated by PHONON (see Appendix D). Next, $\rho(\omega)$ is converted to $\rho(\varepsilon)$ (recall that $|\hbar\omega| = |\varepsilon|$) and renormalized.

Graphite has two basis positions that are unique by symmetry. They are defined by A-type and B-type carbon atoms as described in Section 4.2. To be strictly correct, a separate phonon DOS should be provided for each unique basis position (this information is available in the PHONON output) and distinct Debye-Waller factors should be used in calculating the thermal scattering law. However, the asymmetry between A-type and B-type carbon atoms is small and present only in the $z$-direction, where interatomic distances are large and interplanar forces are very weak. There is no in-plane asymmetry. Consequently, it is not surprising that the partial phonon DOS is virtually identical for all corresponding coordinate vectors for the A-type atoms and B-type atoms. Therefore, the total phonon DOS of the system is safely applied.

Figure 4.4 displays the reference total phonon DOS $\rho(\varepsilon)$ for graphite which will be used in the remainder of this work. It is compared to the Al-Qasir phonon spectrum [17, 18] and the YK phonon spectrum [22] incorporated in the ENDF/B-VII File 7 evaluation for graphite [21]. The Al-Qasir phonon spectrum is very similar to the reference $\rho(\varepsilon)$, except that Al-Qasir imposes a parabolic fit up to 5 meV [17]. Recall that in the work of Young and Koppel, the crystallography and lattice dynamics of perfect crystalline ABAB-stacked graphite are used, except the four force constants in the YK lattice dynamics model are fitted

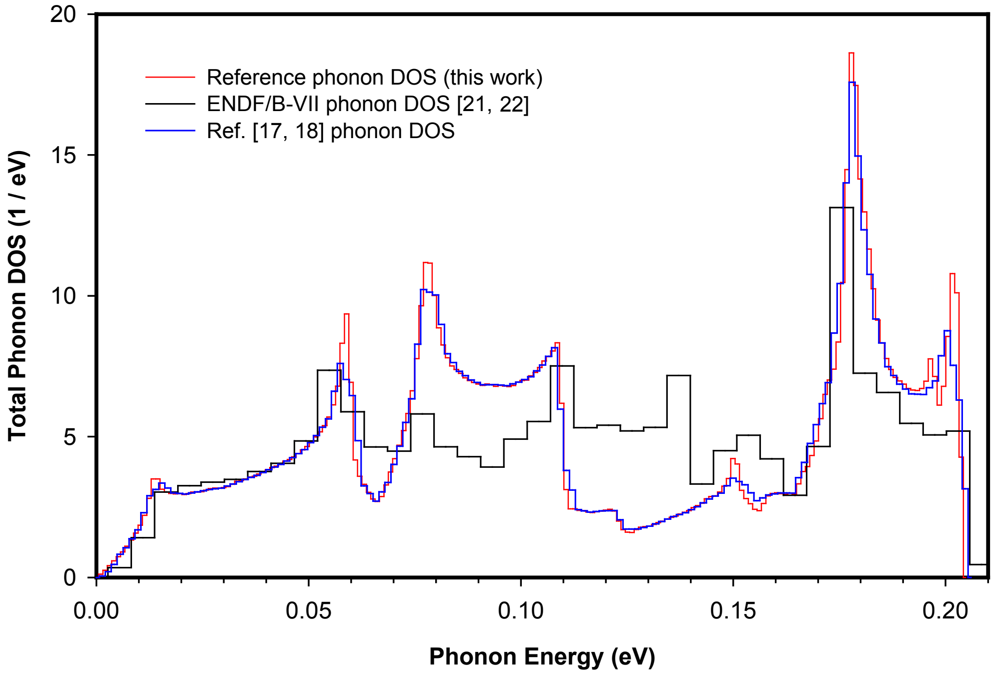

**Figure 4.4 Total phonon DOS comparison for graphite. The red line is the reference spectrum calculated in this work with VASP/PHONON. The black line is the ENDF/B-VII YK spectrum [21, 22]. The blue line is the Al-Qasir spectrum [17, 18].**

to thermodynamic data associated with high-porosity reactor grade graphite. Therefore, the general features of the YK phonon spectrum match those of the reference $\rho(\varepsilon)$ but with differing intensities. Figure 4.5 provides a zoom-in of the three phonon spectra shown in Figure 4.4 for the low-energy region below 24 meV.

The calculated parallel (in-plane) and perpendicular (out-of-plane) partial phonon DOS are displayed in Figure 4.6, overlaid to exhibit their individual contributions. The parallel DOS (which is the sum of the two in-plane polarizations) is normalized to 2/3, and the perpendicular DOS (which accounts for phonon modes with out-of-plane polarization) is

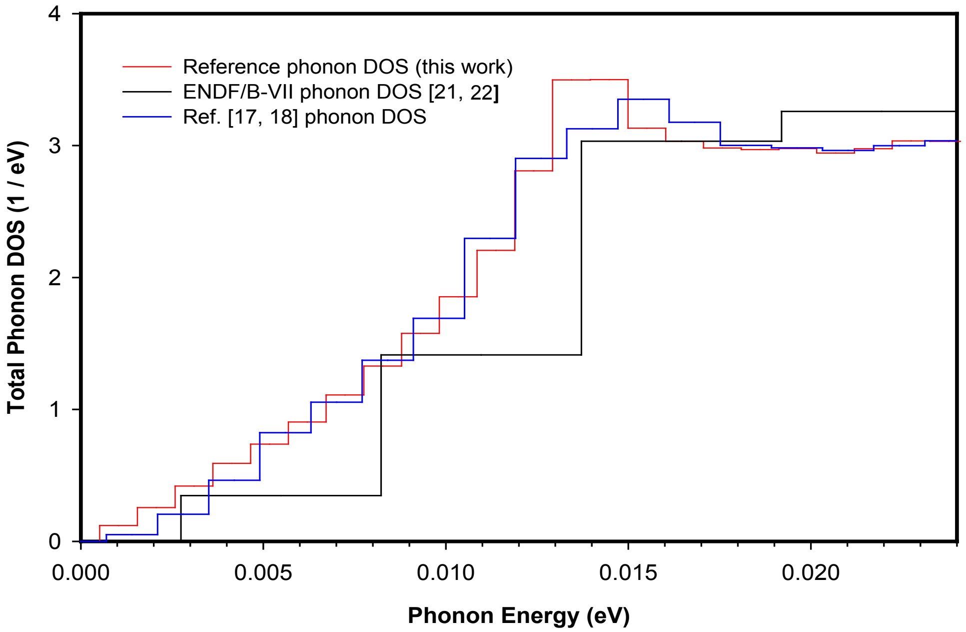

**Figure 4.5 Zoom-in of Figure 4.4 for the low-energy region below 24 meV.**

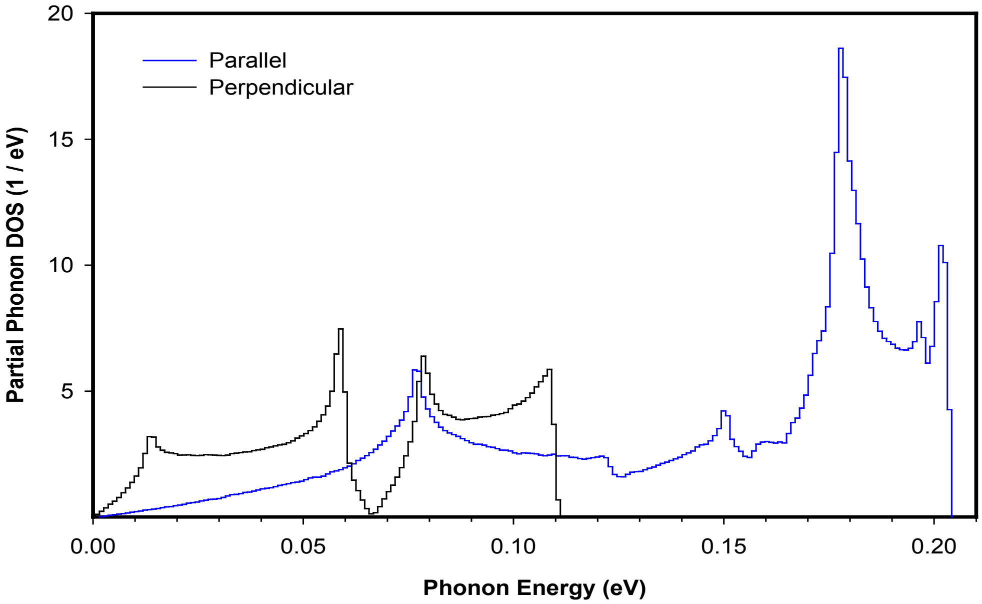

**Figure 4.6 Reference partial phonon density of states for graphite, by direction, calculated with VASP/PHONON. Parallel (blue line, in-plane), perpendicular (black line, out-of-plane).**

normalized to $1/3$. For three degrees of freedom, there are three polarization vectors $\boldsymbol{e}_j$, each of which is considered associated with a Cartesian vector.

In Figure 4.6, it is evident that the lower energies are dominated by phonon modes with out-of-plane polarization and the higher energies are associated *only* with phonon modes having in-plane polarizations. While this is to be expected from the layered structure of graphite, it is important to note that the total energy functional utilized in VASP does not account for interplanar Van der Waals forces (see Appendix D). Therefore, the perpendicular energies seen in Figure 4.6 are the result of interactions between the oscillating unbonded valence $\pi$-electrons in neighboring planes as well as planar tensions and shear stresses induced by motion of the basis atoms in the $z$-direction.

### 4.3.2 The Reference Dispersion Relations

There is a total dispersion relation $\omega(\boldsymbol{q})$, combining all basis atoms, which maps throughout the first Brillouin zone. It is standard to plot this $\omega(\boldsymbol{q})$ for $\boldsymbol{q}$-vectors terminating on lines of high symmetry which bound an irreducible section of the first Brillouin zone. For a hexagonal lattice, $\omega(\boldsymbol{q})$ is typically plotted for $\boldsymbol{q}$-vectors along the $\overrightarrow{\Gamma\mathrm{A}}$, $\overrightarrow{\Gamma\mathrm{M}}$, and $\overrightarrow{\Gamma\mathrm{K}}$ directions, and for $\boldsymbol{q}$-vectors terminating on $\overline{\mathrm{KM}}$ (see Figure 4.3). Figure 4.7 gives this reference $\omega(\boldsymbol{q})$ generated by the VASP/PHONON process and shows its relationship to the total phonon DOS.

Each curve may be conceptualized as mapping the intersections of isofrequency surfaces in reciprocal space with a $\boldsymbol{q}$-vector originating at the $\Gamma$-point and extending in the $\overrightarrow{\Gamma\mathrm{A}}$, $\overrightarrow{\Gamma\mathrm{M}}$, and $\overrightarrow{\Gamma\mathrm{K}}$ directions. The intersections of isofrequency surfaces with a $\boldsymbol{q}$-vector terminating on

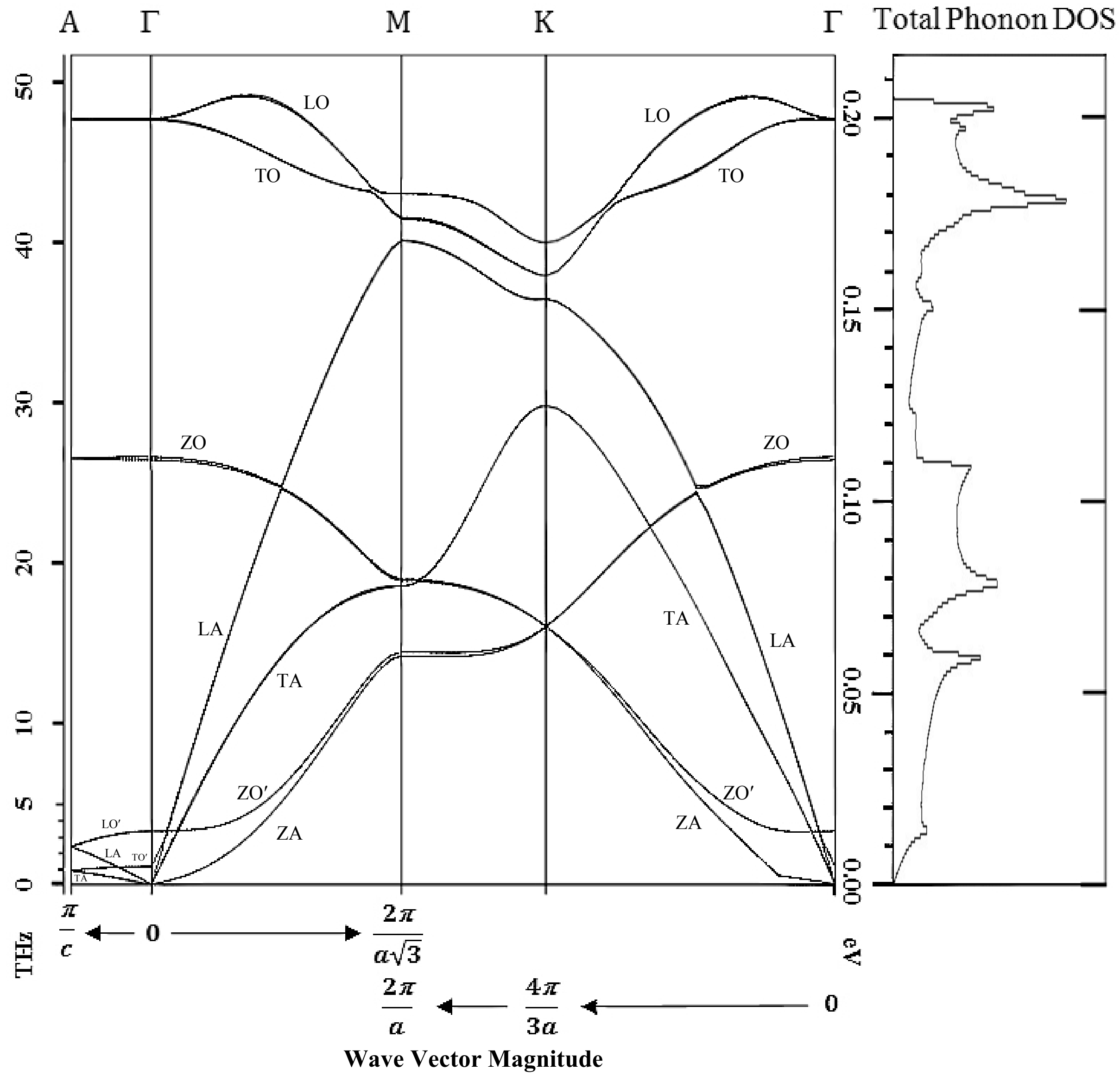

**Figure 4.7 Graphite reference dispersion relations along directions of high symmetry calculated with VASP/PHONON. The corresponding total phonon DOS is shown to the right for comparison.**

the $\overline{\mathrm{KM}}$ line are mapped by extending a ***q***-vector in the $\overrightarrow{\Gamma \mathrm{K}}$ direction beyond the first Brillouin zone to the point M′ (i.e., the next M-point by periodicity). This is equivalent by reflection to terminating the ***q***-vector on the $\overline{\mathrm{KM}}$ line at the boundary of the first Brillouin zone. The different branches of the dispersion relations are labeled in Figure 4.7 where T is in-plane transverse polarization, Z is out-of-plane transverse polarization, L is longitudinal polarization, A is acoustic and O is optical. The $\mathrm{O}'$ terms distinguish optical modes associated with a different phase relationship among the basis atoms.

Transverse phonon waves have perpendicular propagation and polarization directions. Longitudinal phonon waves have parallel propagation and polarization directions. For phonons waves propagating in any $\overrightarrow{\Gamma\mathrm{K}}$ direction with L polarization and for phonon waves propagating in any $\overrightarrow{\Gamma\mathrm{M}}$ direction with T polarization, the atomic vibrations can be considered to be in the $\hat{\boldsymbol{x}}$ direction by symmetry. Likewise, for phonon waves propagating in any $\overrightarrow{\Gamma\mathrm{K}}$ direction with T polarization and for phonon waves propagating in any $\overrightarrow{\Gamma\mathrm{M}}$ direction with L polarization, the atomic vibrations can be considered to be in the $\hat{\boldsymbol{y}}$ direction by symmetry (see Figure 4.2(b)). The two T polarizations for phonon waves propagating in the $\overrightarrow{\Gamma\mathrm{A}}$ direction are effectively degenerate for atomic vibrations in the $\hat{\boldsymbol{x}}$ or $\hat{\boldsymbol{y}}$ directions and will have the same associated frequencies. For phonon waves propagating in any in-plane direction with Z polarization and for phonon waves propagating in the $\overrightarrow{\Gamma\mathrm{A}}$ direction with L polarization, atomic vibrations will be in the $\hat{\boldsymbol{z}}$ direction. Finally, for phonon waves propagating in any off-symmetry direction, the definitions of polarizations are fixed as defined above, and the propagation and polarization directions will be neither perpendicular nor parallel.

Note that peaks in the phonon DOS are associated with frequencies for which the magnitude of the gradient of $\omega$ with respect to $\boldsymbol{q}$, or $|\boldsymbol{\nabla}_{\boldsymbol{q}}\omega|$, is small or approaching zero. This gradient magnitude is also known as the group velocity of the phonon and determines its speed of propagation through the crystal. In one dimension, it is analogous to $\frac{\partial\omega}{\partial q}$. These frequency peaks are known as Van Hove singularities and are physically associated with standing wave packets of phonons. In the context of sampling $\boldsymbol{q}$-points in the first Brillouin zone, it can be conceptualized that these peaks arise because the isofrequency surfaces are "thick," or because "adjacent" surfaces are widely separated, and many $\boldsymbol{q}$-points will be associated with the same or nearly the same frequency.

## 4.4 Thermal Scattering Law and Cross Section Calculations with the Reference Total Phonon Density of States

Before commencing the uncertainty analysis for graphite, integrated inelastic cross section, differential cross section and thermal scattering law results will be presented based on the reference phonon density of states calculated with VASP/PHONON. All calculations are with a 110-point $\beta$-grid and 70-point $\alpha$-grid which provided good convergence of integrated cross sections. Figure 4.8 displays the reference inelastic cross section for graphite calculated to phonon order $n = 100$. It is compared to the inelastic cross section calculated with published ENDF/B-VII File 7 $S_{\text{sym}}(\alpha,\beta)$ data [21], which is based on the YK phonon spectrum [22], and to the inelastic cross section calculated by Al-Qasir, in which a parabolic fit is imposed up to 5 meV in a phonon DOS generated by VASP/PHONON [17] that is otherwise similar to the reference phonon DOS (see Figures 4.4 and 4.5).

The inelastic cross sections are calculated at 293.6 K. In the region near $k_{\mathrm{B}}T = 0.0253$ eV (for $T = 293.6\,K$), the curves differ by as much as 100%. The variation in the cross

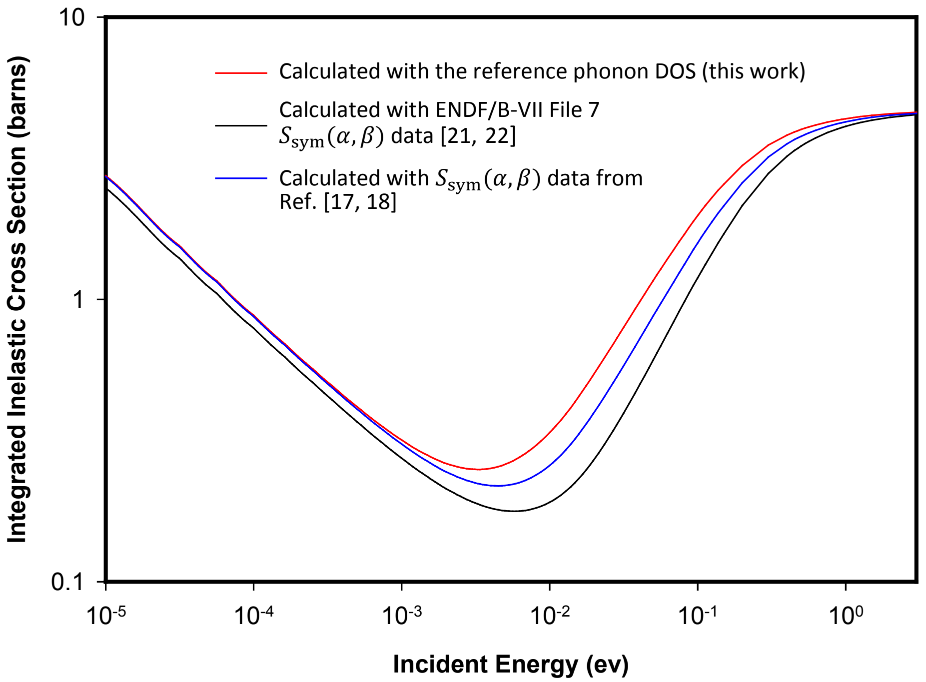

**Figure 4.8 Inelastic cross sections for graphite calculated from different information. Using the reference phonon spectrum produced by VASP/PHONON in this work (red line). Using the published ENDF/B-VII File 7 $S_{\text{sym}}(\alpha,\beta)$ data for graphite (black line) [21], which is based on the YK phonon spectrum [22]. Using the Al-Qasir $S_{\text{sym}}(\alpha,\beta)$ data and phonon spectrum produced by VASP/PHONON with an imposed parabolic fit up to 5 meV (blue line) [17, 18]. Cross sections are calculated at 293.6 K.**

section results serves to illustrate two points. First, the characteristics of phonon spectra associated with the same crystal structure can differ in important ways when the methodologies or assumptions incorporated in their generation differ, and the resulting cross sections can be affected significantly. Second, the benefit of using a thermal cross section library produced with a phonon DOS associated with a particular material model may be questioned if the actual material in the scattering medium does not reflect this model.

Plots for differential cross sections in energy for graphite for $E$ = 0.005 eV, 0.0253 eV, 0.1 eV and 0.5 eV are given in Figure 4.9 at 293.6 K. The abscissa is in terms of energy

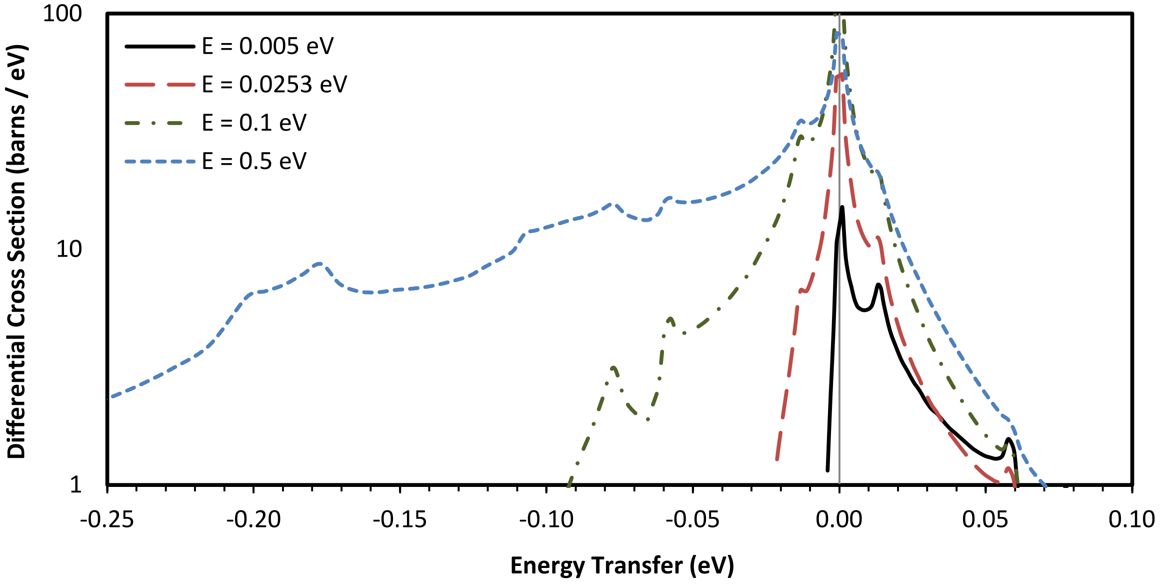

**Figure 4.9 Differential cross sections in energy for graphite at 293.6 K for various incident energies. *E* = 0.005 eV (black plot), 0.0253 eV (red plot), 0.1 eV (dark green plot) and 0.5 eV (blue plot).**

transfer, vs. secondary energy, to facilitate comparison of changes in the structure of the distributions as a function of incident energy. Table 4.1 tabulates information about downscattering, upscattering, the total inelastic cross section, and multiphonon components of these. It is notable that the distributions in Figure 4.9 are much more peaked than those based on the YK phonon spectrum (see Figure 2.4). Physically, this is because hexagonal crystalline graphite has a nearly linear phonon DOS up to about 8 meV as a result of its quasi-two-dimensional layered structure. It is only parabolic at extremely low energies below about 1 meV [50, 51, 52]. This phenomenon will be discussed in further detail in Section 4.5.3.1. The YK spectrum given in Figure 2.3 is parabolic up to about 16 meV, which is characteristic of a fully three-dimensional (i.e., non-planar) crystal structure, and this may be more appropriate for quasi-amorphous reactor grade graphite.

**Table 4.1 Inelastic scattering cross section, downscattering, upscattering and multiphonon information for differential cross sections in energy given in Figure 4.9.**

| Incident Energy | (eV) | 0.005 | 0.0253 | 0.100 | 0.500 |
|---|---|---|---|---|---|
| | | | | | |
| Downscattering | (barns) | 0.0252 | 0.2547 | 1.143 | 3.183 |
| Upscattering | (barns) | 0.2364 | 0.4073 | 0.8355 | 0.8144 |
| Total | (barns) | 0.2616 | 0.6619 | 1.979 | 3.998 |
| | | | | | |
| Downscattering | (%) | 9.63 | 38.47 | 57.77 | 79.63 |
| Upscattering | (%) | 90.37 | 61.53 | 42.23 | 20.37 |
| Down/Up Scattering | (ratio) | 0.107 | 0.625 | 1.368 | 3.908 |
| | | | | | |
| Multiphonon Contribution to Downscattering | (%) | 0.83 | 6.51 | 30.16 | 84.03 |
| Multiphonon Contribution to Upscattering | (%) | 9.60 | 13.44 | 31.47 | 68.76 |
| Multiphonon Contribution to Total | (%) | 8.75 | 10.78 | 30.71 | 80.91 |
| Down/Up Scattering Multiphonon Contribution | (ratio) | 0.086 | 0.4 | 0.958 | 1.222 |

The broadening of the distributions in Figure 4.9 as a function of incident energy is directly attributable to an increase in multiphonon scattering. Not only do the distributions broaden in an absolute sense, but the secondary spectra become progressively less sensitive to the structure of the phonon DOS and they are "smoothed." Table 4.1 gives details of the relationships of incident energy, downscattering, upscattering and multiphonon scattering.

The thermal scattering law $S_{\text{sym}}(\alpha,\beta)$ for hexagonal graphite at 293.6 K calculated with the reference phonon DOS is plotted in Figure 4.10 as a function of $\beta$ for several fixed $\alpha$. Likewise, Figure 4.11 plots $S_{\text{sym}}(\alpha,\beta)$ as a function of $\alpha$ for several fixed $\beta$. In Figure 4.10,

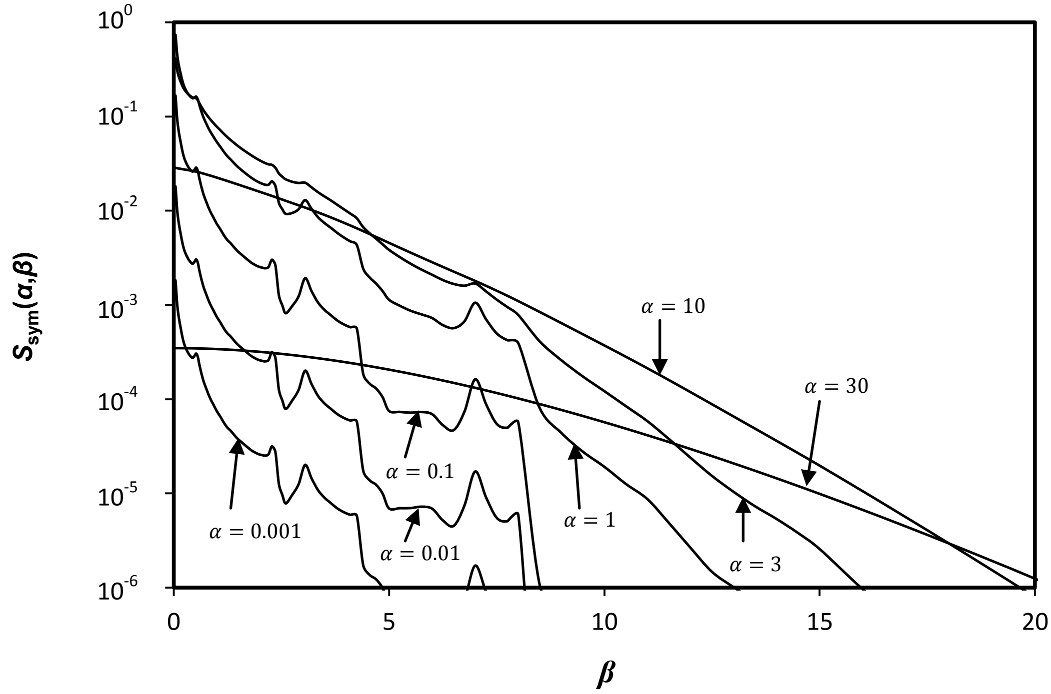

**Figure 4.10 Fixed $\alpha$ curves of $S_{\mathrm{sym}}(\alpha,\beta)$ for graphite at 293.6 K as a function of $\beta$.**

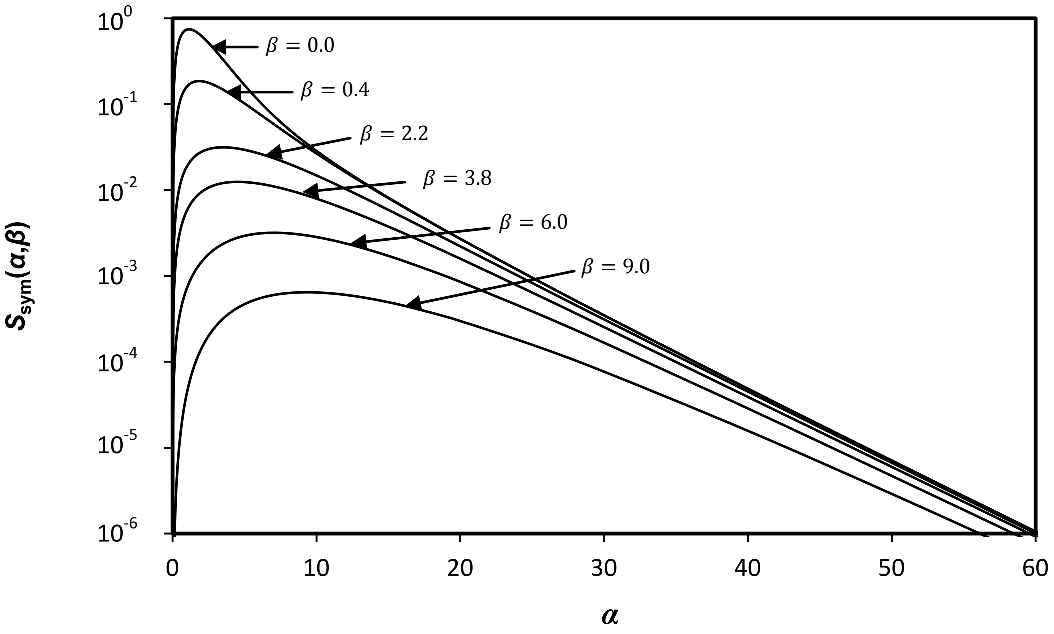

**Figure 4.11 Fixed $\beta$ curves of $S_{\mathrm{sym}}(\alpha,\beta)$ for graphite at 293.6 K as a function of $\alpha$.**

the $\alpha = 0.001$, 0.01 and 0.1 curves are associated almost entirely with one-phonon scattering, and the fine structure of the phonon spectrum is evident. $S_{\text{sym}}(\alpha, \beta)$ is less than 0.001 for all $\beta$ when $\alpha < 0.001$. At $\alpha = 1$, one-phonon and multiphonon scattering are mixed and the features of $S_{\text{sym}}(\alpha, \beta)$ begin to smooth. At $\alpha = 3$, multiphonon scattering is dominant. At $\alpha = 10$ and $\alpha = 30$, essentially all structure in $S_{\text{sym}}(\alpha, \beta)$ is lost. All curves are less than 0.001 for $\beta > 10$. In Figure 4.11, a selection of $\beta$ curves is given. The $\beta = 0$ curve gives the upper limit of $S_{\text{sym}}(\alpha, \beta)$ as a function of $\alpha$ and is associated with quasielastic multiphonon scattering, or multiple phonon energy exchanges combining to yield nearly zero energy transfer. With the exception of very low $\beta$, the proportion and order of multiphonon scattering will tend to increase with $\beta$. For $\beta > 8$, $S_{\text{sym}}(\alpha, \beta)$ is less than 0.001 for all $\alpha$.

## 4.5 Assessing and Calculating Uncertainties in the Phonon Density of States for Graphite

Density functional theory is a first-principles condensed matter simulation methodology that has been very successful in modeling the physical properties of materials. As with almost all physics models, there are inherent and practical limitations to its accuracy. Likewise, any lattice dynamics physics model will be subject to similar limitations. There will be inherent uncertainties in any phonon density of states generated through the VASP/PHONON process. These uncertainties may arise due to the physics models employed by VASP and PHONON and due to the selection of code parameters governing the application of those physics models.

Various sources of uncertainty in the phonon DOS for graphite generated by the VASP/PHONON process will now be examined and their impacts modeled using $R$-functions and Monte Carlo sampling as described in Section 3.4.2. To allow a physics-guided approach, the expected sensitivity of cross sections and the thermal scattering law to particular energy regions of the phonon DOS is first examined.

In this work, all Monte Carlo and thermal scattering kernel calculations are performed with the code MCTHERM written by the author. MCTHERM uses the same theoretical methodology as LEAPR for calculating $S_{\text{sym}}(\alpha,\beta)$, except that 64-bit double-precision allows for calculations with high phonon order and large $\alpha$ to be carried out without resorting to the short collision-time approximation [20]. MCTHERM also allows for accurate intermediate phonon-order outputs (unlike LEAPR), and it allows greater flexibility in the selection of $\alpha$ and $\beta$ grids, energy grids, and the output format. MCTHERM was benchmarked to LEAPR in a variety of tests to confirm the consistency of its calculations. The MCTHERM code incorporates native Monte Carlo sampling of phonon spectra based on user-defined perturbations in a reference phonon DOS, and the code allows for introducing uncertainty in temperature if desired. Finally, MCTHERM can calculate resulting uncertainties and/or covariance matrices for the phonon DOS, the thermal scattering law, differential cross sections in energy and integrated cross sections.

### 4.5.1 Cross Section Sensitivity to the Phonon Density of States

The phonon density of states has been described as a probability density function of atomic vibrational modes that exist in a given material structure. In this sense, it is natural to treat uncertainties in the thermal scattering law in the context of this PDF. However, the phonon spectrum only maps the population distribution of phonon modes as a function of energy. It does not provide any information regarding the *likelihood* that a particular phonon mode will be excited.

If the vibrational motion of an atom is associated with an incoherent mixture of phonon modes and that atom is part of an ensemble of atoms at an average temperature $T$, then for a phonon mode with energy $\varepsilon$, the thermal average of the phonon occupation number $n$ is

$$< n > = \left[\exp\left(\frac{\varepsilon}{2k_{\mathrm{B}}T}\right)\sinh\left(\frac{\varepsilon}{2k_{\mathrm{B}}T}\right)\right]^{-1} \tag{4.4}$$

[15]. An estimate of the relative probability that a phonon with energy $\varepsilon$ will participate in a thermal scattering event can be given by the scattering probability density function

$$T(\varepsilon) = C < n > \rho(\varepsilon), \tag{4.5}$$

where $C$ is a normalization constant. $T(\varepsilon)$ is plotted vs. $\rho(\varepsilon)$ in Figure 4.12 for graphite at the temperatures 300 K and 1500 K.

Eq. (4.4) strictly applies only for upscattering (for downscattering, the quantity $< n + 1 >$ is required). Additionally, Eq. (4.5) neglects coherent interference effects, although this is consistent with the incoherent approximation invoked for the thermal scattering law. Finally, Eq. (4.5) gives the relative probability for a particular $\alpha$ and does not account for the fact that the average $\alpha$ is a function of $E$. Even so, the general shape of $T(\varepsilon)$ calculated from Eqs. (4.4) and (4.5) is a strong qualitative predictor of the sensitivity of cross sections to different energy regions of the phonon DOS as a function of temperature.

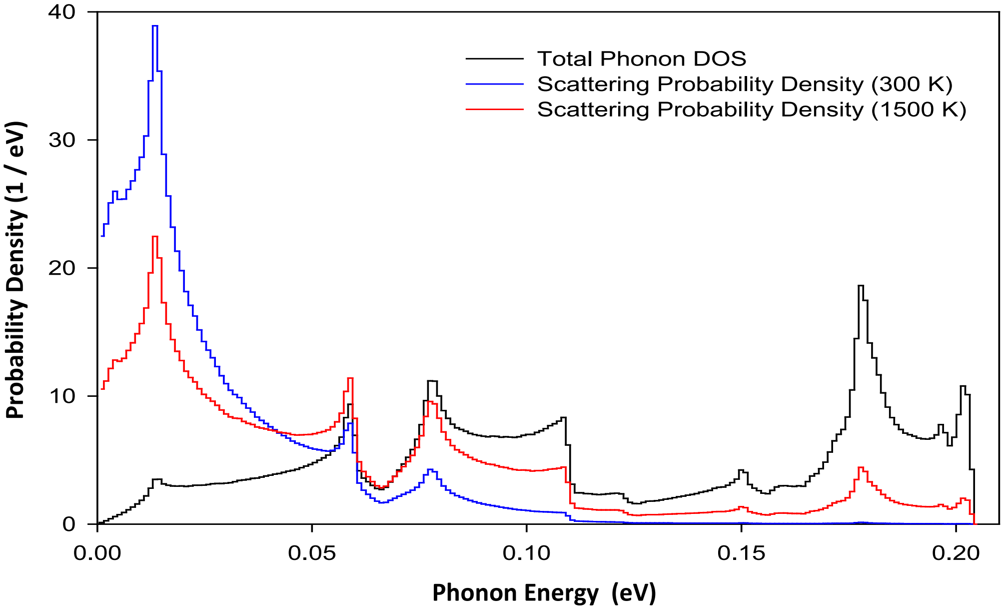

**Figure 4.12 Scattering probability density function $T(\varepsilon) = p(\varepsilon)\rho(\varepsilon)$ at 300 K and 1500 K.**

It is clear that the thermal scattering law and integrated cross sections will, in general, be very sensitive to the population of low-energy phonons and extremely insensitive to the population of higher-energy phonons. Indeed, the large peak in the phonon DOS near 175 meV (see Figure 4.4) is barely visible in the map of $T(\varepsilon)$ at 300 K. Thus, uncertainties in the thermal scattering law and integrated cross sections will heavily depend on uncertainties in the lower-energy region of the phonon spectrum.

Reviewing Figure 4.6, recall that phonons with polarizations perpendicular to the carbon atom planes dominate the low-energy region of the phonon spectrum. Considering Figures 4.6 and 4.12 together, it is clear that uncertainties in the thermal scattering law and in integrated cross sections will depend overwhelmingly on uncertainties in the perpendicular phonon DOS. Consequently, it is essential that any uncertainty analysis carefully examine physical phenomena which affect the low-energy perpendicular phonon modes and how well those phenomena are represented in the VASP/PHONON methodology for generating $\rho(\varepsilon)$.

### 4.5.2 Estimating Uncertainties Internal to VASP and PHONON

To facilitate the evaluation of the total uncertainty in $\rho(\varepsilon)$, it is beneficial to separate those uncertainties which can be considered *internal* to the VASP and PHONON codes from those which can be considered *external* to the codes. For example, any uncertainties arising strictly due to the user's particular selection of parameters when executing VASP and PHONON can be considered internal uncertainties. In other words, the variation in the calculated $\rho(\varepsilon)$ resulting from particular sets of code parameter choices defines internal uncertainty, and this can include both Type 1 and Type 2 uncertainties. Additional variation in $\rho(\varepsilon)$ can also be described by the evaluator. This additional variation may be based on experimental data, corrections to the physics models employed by VASP and PHONON, etc. The uncertainty resulting from this additional evaluator-imposed variation defines external uncertainty, and this will always be of Type 2.

Running the VASP and PHONON codes requires the user to specify many input parameters which will control the computational algorithms and specific physics models invoked in their execution. It is not the intent of this discussion to provide an exhaustive list and analysis of every input parameter in these codes. Rather, a qualitative approach is more practical and is sufficient. Unlike empirical models with fitted "tunable" parameters, most of the parameters of these codes cannot be treated as random variables. In other words, assignment of expectation values or covariances generally has no real meaning for parameters such as the exchange-correlation energy model (e.g., LDA or GGA) or supercell size. Similarly, there will be parameters which, without source code modification, the user must accept. An example is the particular pseudopotentials employed in the calculation of the $V[n(\boldsymbol{r})]$ term from Eq. (D.1).

The VASP and PHONON input parameters can be divided into two general classes: "convergence" parameters and "algorithm" parameters. The former class controls *to what extent* or the *resolution with which* the codes carry out calculations. Examples include the plane-wave energy cutoff, and the $k$-mesh and supercell sizes. Although these examples involve the setting of numerical criteria, they are related to Type 2 uncertainty because they control the *accuracy* of the output (and not the *precision* of the output). The $\boldsymbol{q}$-point sampling resolution of the first Brillouin zone is also a convergence parameter, but it is related to Type 1 uncertainty because it strictly controls the *precision* of the output. In theory, given unlimited computing resources, the convergence parameters should be able to be set to arbitrarily high-quality limits until the output is converged to arbitrarily fine criteria. In practice, a balance with computational expense is usually necessary. In the production of the reference phonon DOS and dispersion relations given in Figures 4.4 – 4.7, the final Type 2 uncertainty convergence parameters chosen are optimized with computational expense and still provide good convergence [17] (i.e., the phonon DOS and dispersion relations outputs do not consequentially change for incremental improvements in any of the Type 2 convergence parameters). Therefore, it will be assumed that any Type 2 uncertainty in the phonon DOS due to the convergence parameters is negligible.

#### 4.5.2.1 Type 1 Uncertainties from Sampling the First Brillouin Zone

There will be purely statistical uncertainties, or counting uncertainties, arising from randomly sampling $\boldsymbol{q}$-points in the first Brillouin zone to determine the phonon density of states (see Appendix D). The number of $\boldsymbol{q}$-points sampled is a convergence parameter controlled by the user. Strictly, the partial phonon DOS frequency bins for each Cartesian vector and basis atom will be populated during the PHONON Monte Carlo sampling process according to a Dirichlet (or compound) multinomial distribution with covariances that are determined by the force constant and dynamical matrices. In the limit of a large number of frequency samples collected in a large number of bins, each bin may be treated as being populated according to a Gaussian distribution, although the Gaussians will not necessarily be independent.

In this work, $N = 10^6$ $\boldsymbol{q}$-points are sampled and $D = 199$ bins (or grid points) with a uniform energy width of $p_{\text{int}} = 1.03$ meV are used for each partial and for the total phonon DOS. Each partial will contain one million frequency samples. These conditions are sufficient to use the Gaussian approximation. However, the total phonon DOS, which is the sum of all of the partials for each frequency bin, is the spectrum for which uncertainties are required.

The value of each partial frequency bin will be designated as $p_d^{par}$, where $d = 1 \ldots D$ and $par = 1 \ldots 12$ for each of the twelve dispersion branches of graphite. After normalizing each partial phonon DOS, the standard deviation for each $p_d^{par}$ is calculated as

$$\sigma(p_d^{par}) = \sqrt{\frac{p_d^{par}}{N p_{\text{int}}}}. \qquad (4.6)$$

The quantities $\sigma(p_d)$ will be required for an $R$-function. Since $p_d = \sum_{par=1}^{12}(p_d^{par})$, $\sigma(p_d)$ can be calculated as

$$\sigma(p_d) = \sqrt{\sum_{g,h} \mathrm{COV}(p_d^{par=g}, p_d^{par=h})}, g = 1 \dots 12, \; h = 1 \dots 12. \tag{4.7}$$

In this case, $g$ and $h$ are indices for incrementing the twelve rows and columns of the $p_d^{par}$ covariance matrix (for fixed $d$). Note that no sensitivity coefficients (or $\frac{\partial p_d^{par}}{\partial p_d}$) are included in Eq. (4.7) since they are all unity.

For a particular coordinate vector, each partial phonon DOS for the different basis atoms is almost identical. Therefore, it can be assumed that they are perfectly correlated with a covariance equal to the product of their standard deviations, which are defined by Eq. (4.6). Physically, there are isofrequency surfaces in reciprocal space associated with each branch of the dispersion relations for that frequency. The isofrequency surfaces are virtually degenerate for the different basis atoms. Therefore, any random $\boldsymbol{q}$-point located on a particular isofrequency surface associated with one basis atom will effectively be located on the same isofrequency surface for all other basis atoms.

The situation is different for partials of different Cartesian coordinates. In this case, the isofrequency surfaces associated with different polarizations (for the same frequency) may or may not intersect and will have distinct geometry within the first Brillouin zone. Therefore, only in rare instances will a $\boldsymbol{q}$-point be located simultaneously on the isofrequency surfaces associated with different polarizations (for the same frequency). Consequently, the partials for different coordinate vectors can be considered to be uncorrelated and Eq. (4.7) can be rewritten as

$$\sigma(p_d) = \sqrt{\textstyle\sum_{par} \sigma^2(p_d^{par}) + 2 \sum_{g,h,j} \sigma\left(p_j^{\eta = g}\right) \sigma\left(p_j^{\eta = h}\right)};$$

$$par = 1 \ldots 12;\; g = 1 \ldots 3,\; h = (g+1) \ldots 4\,;\; j = 1 \ldots 3, \tag{4.8}$$

where $\eta$ represents a basis atom and $j$ corresponds to polarizations in terms of the Cartesian coordinates. The first term under the square root in Eq. (4.8) captures uncorrelated uncertainties while the second term captures fully correlated uncertainties. In the formulation of Eq. (4.8), terms of $\mathtt{COV}(p_d^{par})$ with zero correlation are absent. The indices $g$ and $h$ now increment only the basis atom in the rows and columns of $\mathtt{COV}(p_d^{par})$. The correlated terms of $\mathtt{COV}(p_d^{par})$ are given by $\sigma(p_j^{\eta = g})\sigma(p_j^{\eta = h})$. The coefficient 2 accounts for the triangular symmetry of the covariance matrix since $g$ and $h$ are defined to increment only over the upper-right triangle (excluding the diagonal).

Now that a fully described set of $\sigma(p_d)$ is given, it must be considered if there are any correlations between $p_d$ (for different $d$) related to sampling the first Brillouin zone. For each $\boldsymbol{q}$-point sampled, there will be twelve coupled frequencies associated with it which will all contribute to the total phonon DOS. The dispersion relations define this coupling for each $\boldsymbol{q}$. Consequently, there will certainly be some underlying correlation between any two given frequencies in the total phonon DOS. However, the $\boldsymbol{q}$-points are randomly sampled and an infinite number of $\boldsymbol{q}$-points will be associated with any particular frequency. Each $\boldsymbol{q}$-point that is associated with a particular frequency will couple that frequency to different sets of other frequencies. In summary, while correlations among $p_d$ cannot be calculated without re-running the Brillouin zone sampling process a large number of times, it can be stated that the correlations are generally not expected to be strong because of this “averaging” effect.

Neglecting the correlations among $p_d$ in the total phonon DOS resulting from random sampling of the first Brillouin zone, the $R_1$ function given in Section 3.4.2 (which will now be redefined as $R_\mathrm{A}$) can be applied to $\boldsymbol{p}$ using the solutions of Eq. (4.8) to provide a reasonable description of the statistical uncertainties in the parameters $p_d$. Although Eq. (4.8) already provided this information directly, this Type 1 uncertainty will need to be combined with other $R$-functions and then a renormalization condition imposed.

Figure 4.13 plots the relative uncertainty in the $p_d$ parameters of the phonon DOS calculated from Eq. (4.8) to be incorporated in the $R_\mathrm{A}$ function and Monte Carlo sampling process. As expected, the plot is nearly the inverse of the reference phonon spectrum given in Figure 4.4. Higher statistical uncertainties are associated with valleys in the phonon DOS

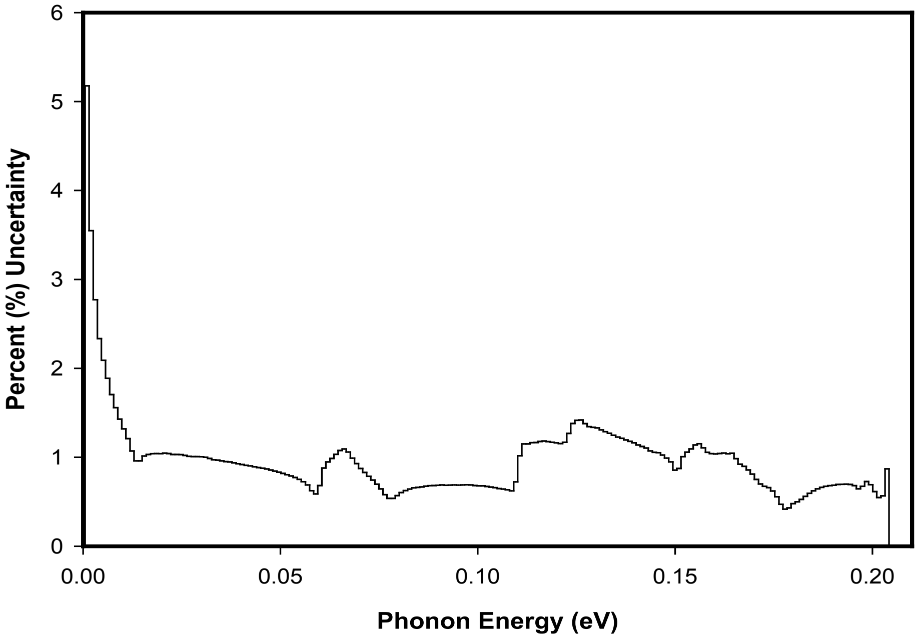

**Figure 4.13 Statistical relative uncertainty in the graphite reference phonon DOS due to random sampling of $10^6$ $\vec{q}$-points in the first Brillouin zone.**

and low statistical uncertainties are associated with peaks. Although the uncertainties are quite small, they will compound with other uncertainties in the Monte Carlo process.

#### 4.5.2.2 Type 2 Uncertainties from Selection of VASP/PHONON Algorithm Parameters

Algorithm parameters for VASP and PHONON control *how* the codes carry out calculations. Examples include the exchange-correlation energy model, atomic displacement magnitudes, and the system relaxation choice (e.g., relax the unit cell, relax the supercell, or do not perform relaxation). The choice of algorithm parameters must be guided by physics and the known operation of the codes. Different selections may provide better results for different problems or materials. In general, the best choice for non-numerical algorithm parameters was clear upon examining the output. For example, the GGA exchange-correlation energy model yields very inaccurate relaxed lattice constants for graphite while the results for LDA are quite close to experimental data. This problem with GGA for graphite is common and documented throughout published literature [17]. The selection of an appropriate atomic displacement magnitude (for the purpose of determining the Hellmann-Feynman forces) required testing several cases. An appropriate value depends on several factors, including the $k$-mesh employed and the behavior of the total energy functional. In this work, the displacement range from 0.03 Å to 0.08 Å yields similar and physically consistent results in the dispersion relations and phonon DOS, with imaginary frequencies contributing 0.04% or less. If displacements are too small or too large, the population of imaginary frequencies increases dramatically. (See Appendix D for background information.)

Within the acceptable range, small shifts in the phonon DOS are evident above about 140 meV. At lower energies, the results are effectively identical. Figure 4.14 compares the total phonon DOS above 140 meV for three distinct trials – 0.045 Å, 0.055 Å (the reference case) and 0.08 Å. To improve visualization of the energy shift, Figure 4.14 is plotted on a pointwise energy grid with straight connecting lines (instead of in histogram form representing energy binning). All code parameters are held identical (per the reference case) except for the atomic displacement magnitude. The features of the phonon DOS in the upper energy region vary in position by about ± 1 meV while remaining coupled. Although this variation is quite small and in the most insensitive region of the phonon DOS, it can quite

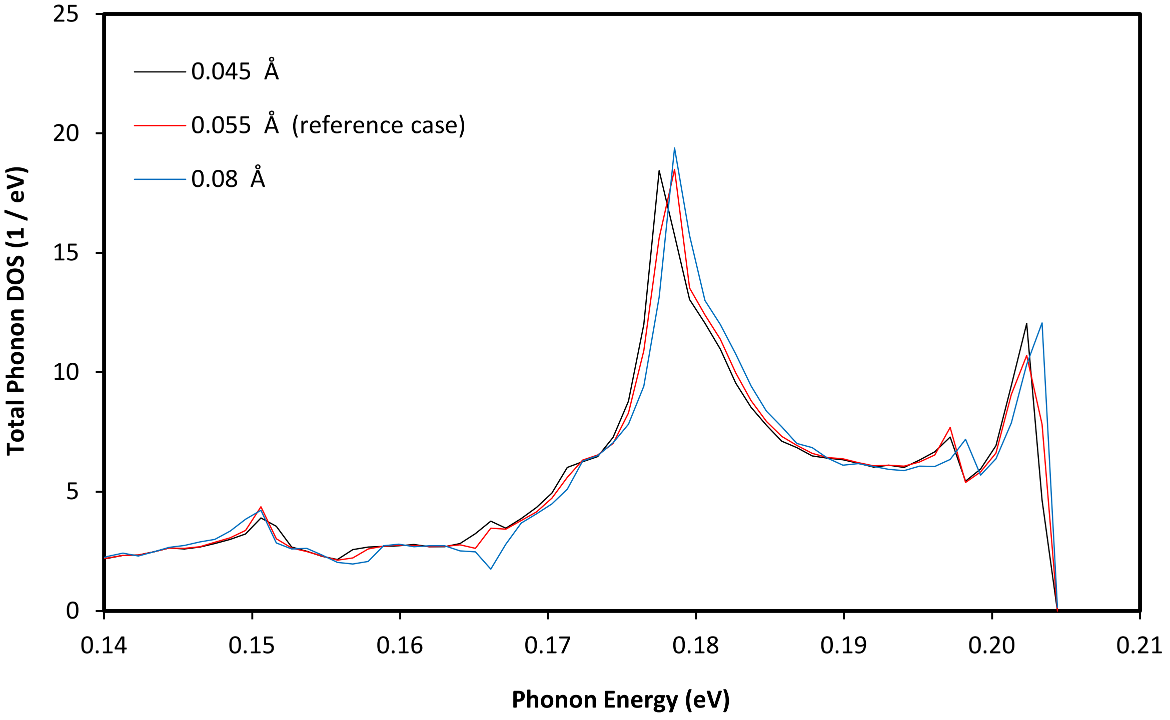

**Figure 4.14 Total phonon DOS for graphite above 140 meV for three atomic displacement magnitudes in VASP. Magnitudes are 0.045 Å (black line), 0.055 Å (red line, reference case) and 0.08 Å (blue line). All other parameters are held fixed to the reference case.**

easily be modeled using a modification of the $R_2$ function given in Section 3.4.2 to demonstrate its effect. The possible energy shift will be bounded by ± 1 meV with flat sampling since there is no reason to judge the reference result to be any more likely than the other cases tested. The energy shift is restricted to the region above 140 meV, or to $p_d$ for $d > 136$ ($D$ = 199 represents the maximum $d$ for the phonon DOS in this work). Finally, separation between features is held constant (the spectrum is not stretched or compressed). Specifically, this $R$-function will be named $R_{\mathrm{B}}$ and defined as follows (see Section 3.4.2 for a review of the variable definitions):

---

$R_{\mathrm{B}}$ := *Fixed spectrum energy shift over a restricted region with flat sampling defined by a minimum and maximum shift.*

$R_{\mathrm{B}}(\boldsymbol{p}) = [R_{\mathrm{B}}(p_d), d = 137 \ldots D-1] = \boldsymbol{p}'$

$\mathrm{PDF}(E_{\mathrm{shift}}) = \frac{1}{2\ \mathrm{meV}},\ E_{\mathrm{shift}} = -1\ \mathrm{meV} \ldots +1\ \mathrm{meV}$

$E_{\mathrm{shift}} = \mathrm{RAND}[\mathrm{PDF}(E_{\mathrm{shift}})]$

```
for $d = 137 \ldots D-1$,
    $E(d') = E(d) + E_{\mathrm{shift}}$
for $d = 137 \ldots D-1$,
    $d'_{\mathrm{low}}, d'_{\mathrm{high}} \equiv [E(d'_{\mathrm{low}}) \leq E(d) < E\left(d'_{\mathrm{high}}\right),\ d'_{\mathrm{high}} = d'_{\mathrm{low}} + 1]$
    $p'_d = \frac{E(d)-E(d'_{\mathrm{low}})}{p_{\mathrm{int}}} \times \left(p_{d'_{\mathrm{high}}} - p_{d'_{\mathrm{low}}}\right) + p_{d'_{\mathrm{low}}}$
```

---

The atomic displacement magnitude was found to be the only algorithm parameter for which a range of justifiable choices was possible that consequentially influenced the total phonon DOS. Thus, $R_{\mathrm{B}}$ will allow a reasonable quantitative assessment of the internal Type 2 uncertainty arising due to the selection of algorithm parameters within the VASP/PHONON simulation process. Note that it does not capture the Type 2 uncertainty present in the native physics models employed but only in their algorithmic application. The only way to truly assess the accuracy of the native physics models (i.e., the exchange-correlation energy model, the pseudopotentials, the harmonic approximation, etc.) is to compare the outputs to experimental data.

### 4.5.3 The Low-Energy Region of the Phonon Density of States

It has been stated that uncertainties in the thermal scattering law and in integrated cross sections will be the most sensitive to uncertainties in the low-energy region of the phonon density of states. For the layered structure of graphite, strong in-plane covalent bonding results in a significant population of high-energy phonon modes with in-plane polarization. Interatomic forces in the $z$-direction control the population and energy distribution of phonon modes with Z polarization. (See Figure 4.6.) Interplanar forces represent the weakest component of $z$-direction forces by far. The other component is due to planar tensions and shear stresses induced by out-of-plane thermal motion of the carbon atoms. Therefore, interplanar forces are largely responsible for the population of low-energy phonons. Interplanar forces are due to Van der Waals forces as well as interactions between $\pi$-electrons oscillating perpendicular to the planes. The latter effect is expected to be much stronger than Van der Waals forces [53]. Therefore, Van der Waals forces may be expected to influence the lowest-energy region of the phonon DOS (to which thermal scattering is the most sensitive). Since density functional theory employed by VASP does not account for Van der Waals forces, the physics of how Van der Waals forces influence the phonon DOS will be assessed and a comparison of the output of VASP and PHONON to experimental data will be made. Specifically, an examination at the level of dispersion relations is required, and the reader is reminded of the relationship $\varepsilon = \hbar\omega$ for phonons. The resulting uncertainty in the reference $\rho(\varepsilon)$ is Type 2 uncertainty external to VASP and PHONON.

#### 4.5.3.1 The Impact of Interplanar Forces on the Dispersion Relations for Graphite

To gain insight into how Van der Waals forces may physically contribute to the phonon DOS, and to address uncertainties in the low-energy region in general, a qualitative comparison of the dispersion relations of graphite to those of graphene can be made. Figure 4.15 shows the dispersion relations of graphene (solid lines) calculated by Mounet and Marzari [54] using DFT with experimental data for graphite using coherent inelastic neutron scattering from Nicklow et al. [51] overlaid. Since graphene is single-layer, it has only two atoms per unit cell and six dispersion branches. Above about 60 meV, the splitting of optical branches for graphite in Figure 4.15 is indiscernible (and nearly so even for theoretical calculations), and the dispersion relations of graphite and graphene are known to be virtually identical. Physically, this is expected since higher-energy modes are associated with stronger interatomic forces. The weak interplanar forces of graphite have little influence in this

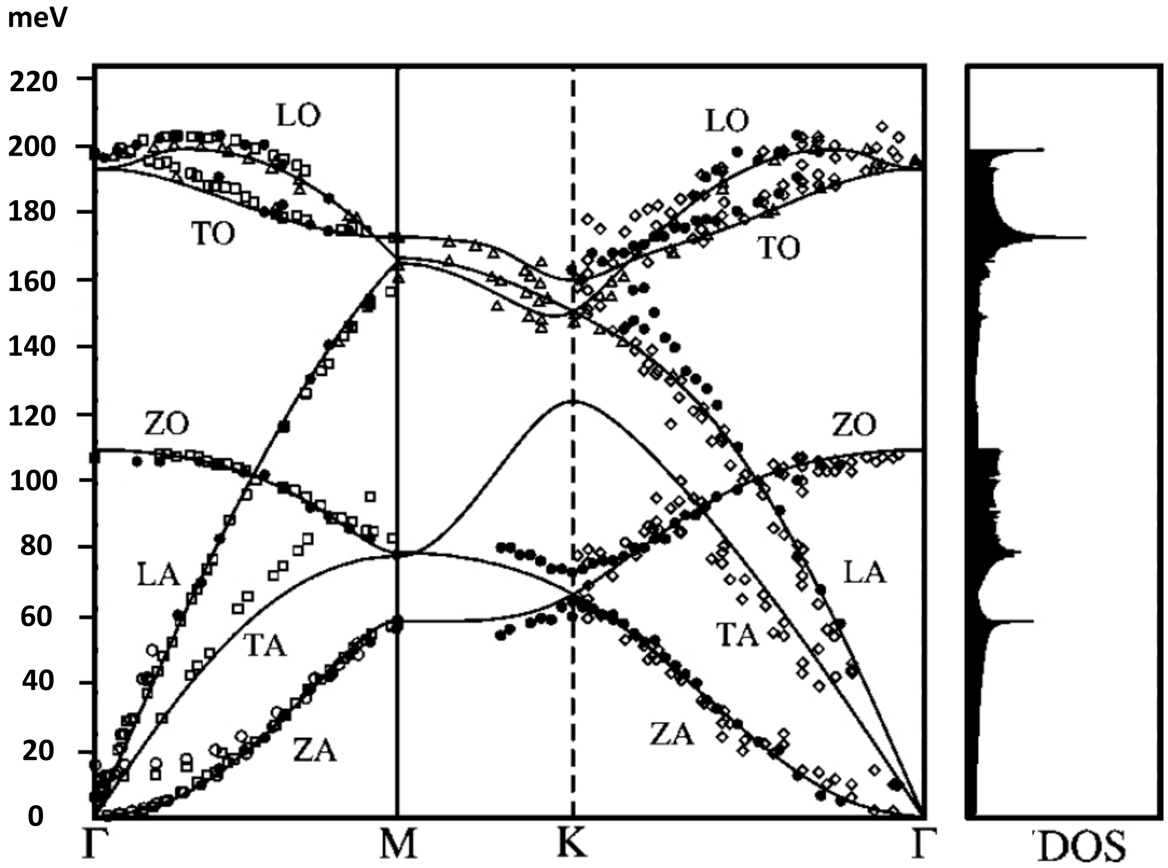

**Figure 4.15 DFT calculation of graphene dispersion relations (solid line) by Mounet and Marzari [54] with experimental data for graphite using coherent inelastic neutron scattering from Nicklow et al. [51]. The total phonon DOS for graphene is shown to the right.**

region [53, 54]. Indeed, the perpendicular phonon DOS is zero above about 110 meV (see Figure 4.6).

Below about 60 meV, the introduction of a layered planar structure alters the dispersion relations of graphene in three primary ways. First, a ZO′ branch splits from the ZA branch because interplanar forces make oscillations between planes (or local regions of planes) possible for these energies. Second, the first Brillouin zone becomes three-dimensional and

$\boldsymbol{q}$-vectors may have a $z$-component (i.e., phonons may propagate from plane to plane). Thus, isofrequency surfaces acquire a three-dimensional character, and the $\overrightarrow{\Gamma\mathrm{A}}$ direction is added to the dispersion relations map giving their intersection with the $z$-axis in reciprocal space. Third, for very low phonon energies, the ZA bending mode is modified. The ZA bending mode is physically represented by the flexural rippling of planes as the basis atoms vibrate in phase with out-of-plane polarization.

For three-dimensional materials, the three acoustical dispersion branches are linear at the Γ-point and $\omega(\boldsymbol{q}) = V_s|\boldsymbol{q}|$. $V_s$ is the speed of sound in the crystal, or $|\boldsymbol{\nabla}_{\boldsymbol{q}}\omega|$. For two-dimensional materials, such as graphene, the ZA bending mode has the form $\omega(\boldsymbol{q}) = \sqrt{\kappa}|\boldsymbol{q}|^2$ at the Γ-point, where $\kappa$ is a function of the bending rigidity of the layer. Graphite behaves as a quasi-two-dimensional material in this regard. The analytical form for the ZA dispersion of graphite at the Γ-point is $\omega(\boldsymbol{q}) = \sqrt{\tau|\boldsymbol{q}|^2 + \kappa|\boldsymbol{q}|^4}$, where $\tau$ is a function of the elastic shear constant. Therefore, in the limit as $\boldsymbol{q} \to 0$ (and as $\omega \to 0$), this reduces to $\omega(\boldsymbol{q}) = \sqrt{\tau}|\boldsymbol{q}|$, and graphite behaves as a three-dimensional material [51, 52, 54]. Physically, shear stress is dominant over the layer bending rigidity for very small $\boldsymbol{q}$ (which are associated with "bending" over extended regions of real space). For larger $\boldsymbol{q}$ (and larger $\omega$), the in-plane propagation of ZA bending mode phonons becomes independent of interplanar forces.

The interplanar forces will also modify the in-plane polarization branches, but only significantly at very low energies (below about 5 meV) [50]. Since the parallel phonon DOS is extremely small in this low-energy region, the impact on the total phonon DOS in this region is negligible.

#### 4.5.3.2 The Impact of Van der Waals Forces on the Dispersion Relations for Graphite

Van der Waals forces can only contribute to the total phonon DOS through the mechanisms by which interplanar forces modify the dispersion relations of graphene to those of graphite. It is expected that the interplanar forces will be dominated by the interaction between adjacent unbonded $\pi$-electrons and that Van der Waals forces will be only a minor component. This expectation is borne out by noting the accuracy with which DFT predicts the relaxed interplanar distance. It was previously stated that the experimental $c$ lattice constant for graphite at 4.2 K is 6.67 Å [55]. The value for $c$ of 6.59 Å predicted in this work (without geometry constraints) gives an error magnitude of 1.2%. Wirtz and Rubio [53] predict, also using DFT with LDA and no constraints, a value of 6.60 Å – giving an error magnitude of 1.1%. Furthermore, in the work of Savini et al. [56], the elastic shear constant (proportional to $\tau$) for graphite is calculated with the linear combination of atomic orbitals (LCAO) method with and without a Van der Waals correction. The Van der Waals correction increased the calculated shear constant by only about 7%. While interplanar forces become important only for energies below about 60 meV, it can be expected that Van der Waals forces become important only for a much lower range of energies.

The ZO′ optical mode splitting in graphite occurs from about 13 meV to 60 meV. Below the Van Hove singularity near 13 meV, which occurs when the LO′ and ZO′ branches intersect at the Γ-point, dispersion relations for phonons propagating in the $z$-direction become possible for all polarizations due to the introduction of interplanar forces. Consequently, it is reasonable to hypothesize that the contribution of Van der Waals forces to the total phonon DOS is captured to a very large extent by the properties of the dispersion relations at energies below the LO′/ZO′ Van Hove singularity. In particular, since the dispersion branches in the $\overrightarrow{\Gamma \mathrm{M}}$ and $\overrightarrow{\Gamma \mathrm{K}}$ directions are modified very little (because interplanar forces have minimal impact on the in-plane propagation of phonons), the main effect of Van der Waals forces will be manifested through the $z$-dependence of the isofrequency surfaces. The LO′/ZO′ Van Hove singularity is not a physical "cutoff" point delimiting where Van der Waals forces may play a role. Rather, it will serve as a convenient upper threshold to the energies at which Van der Waals forces may significantly impact the total phonon DOS. According to Mounet and Marzari [54], Van der Waals forces significantly influence the characteristics of the $\overrightarrow{\Gamma \mathrm{A}}$ dispersions. Finally, since this region of the DOS is the most sensitive from the standpoint of propagated uncertainty, a close examination of the accuracy of the reference VASP/PHONON results in this region is judicious.

#### 4.5.3.3 Geometric Calculation of the Phonon Density of States with Experimental Data

For a periodic crystal structure, the phonon density of states $\rho_{\mathrm{branch}}(\omega)$ associated with one dispersion branch is defined as the number of allowed phonon wave vectors $\boldsymbol{q}$ terminating within the volume in reciprocal space enclosed by the isofrequency surfaces $S(\omega)$ and $S(\omega + d\omega)$ for that branch, per unit $\omega$. Since an infinite perfect crystal is assumed with no wave vector periodic boundary conditions, the number of wave vectors $\boldsymbol{q}$ enclosed by any two isofrequency surfaces is theoretically infinite. However, the only concern is the relative values of the phonon density over $\omega$ such that $\rho_{\mathrm{branch}}(\omega)$ can be considered a normalizable phonon population density function. Without loss of generality, all $\boldsymbol{q}$ are treated as originating at the Γ-point of the first Brillouin zone. Mathematically, one can write

$$\rho_{\text{branch}}(\omega) = C \int_{\text{shell}} \frac{d^3k}{d\omega}, \tag{4.9}$$

where $C$ is a normalization constant, and the integral is taken over the shell volume of reciprocal space enclosed by $S(\omega)$ and $S(\omega + d\omega)$ for the given branch. Note that $\int_{\text{shell}} \frac{d^3k}{d\omega} = \int dS(\omega) dk_\perp$, where $dk_\perp$ is the distance from a surface element $dS(\omega)$ on $S(\omega)$, along a vector normal to $dS(\omega)$, to the surface $S(\omega + d\omega)$. Also, $dk_\perp = \frac{d\omega}{|\nabla_{\boldsymbol{q}}\omega|}$, which is equivalent in one dimension to stating $dk = \frac{d\omega}{d\omega/dk}$. Now, Eq. (4.9) can be rewritten

$$\rho_{\text{branch}}(\omega) = C \int_{\text{S}} \frac{dS(\omega)}{|\nabla_{\boldsymbol{q}}\omega|} = C \int_{\text{S}} \frac{dS(\omega)}{v_{\text{g}}(\omega, \boldsymbol{k})}, \tag{4.10}$$

where $v_{\text{g}}(\omega, \boldsymbol{k})$ maps the group velocity over $S(\omega)$ [40]. Thus, $\rho_{\parallel}(\omega)$ will be given by summing over every T and L polarization branch, $\rho_{\perp}(\omega)$ will be given by summing over every Z polarization branch, and $\rho(\omega)$ will be given by summing over all branches.

With experimental dispersion data for phonon energies below the LO′/ZO′ Van Hove singularity, Eq. (4.10) can be used to calculate the total phonon density of states geometrically in this low-energy region, and this result can be compared to the reference phonon DOS calculated by VASP/PHONON. This allows an assessment of the systematic uncertainty inherent in the reference $\rho(\varepsilon)$ as a result of the neglect of Van der Waals forces and as a result of any other model uncertainties in this highly sensitive low-energy region. In theory, fully three-dimensional experimental dispersion data defining the isofrequency surfaces below the LO′/ZO′ Van Hove singularity within the first Brillouin zone is needed. For hexagonal lattices, it is standard for dispersion relations to be experimentally measured only in the $\overrightarrow{\Gamma A}$, $\overrightarrow{\Gamma M}$, and $\overrightarrow{\Gamma K}$ directions of high symmetry. Even in VASP/PHONON, dispersion data is calculated only in specific requested directions. Fortunately, the symmetry of graphite can be applied to describe the three-dimensional shapes of the isofrequency surfaces using only this high-symmetry information.

The isofrequency surfaces of graphene at low frequencies are circular in two dimensions (or cylindrical in three-dimensions). That is, the group velocity at any particular frequency has in-plane isotropy [50, 57]. It is expected that the addition of interplanar forces in graphite should have no effect on this property. Indeed, in the limit as $\omega \rightarrow 0$, the isofrequency surfaces of graphite are ellipsoidal with in-plane isotropy [58, 59]. Figure 4.16 gives a representation of an ellipsoidal isofrequency surface in the first Brillouin zone [58]. The LO′/ZO′ Van Hove singularity represents a change in topology of the isofrequency surfaces for Z polarizations, above which the surfaces become open at the top of the first Brillouin zone and rapidly transition to the cylindrical shape for two-dimensional graphene.

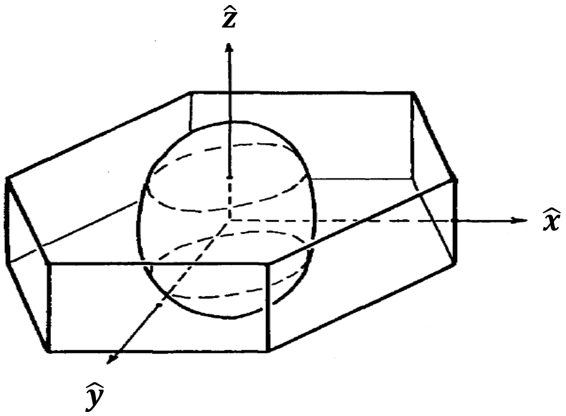

(NOT TO SCALE)

**Figure 4.16 Hexagonal first Brillouin zone for graphite with a representative ellipsoidal isofrequency surface for frequencies below the LO′/ZO′ Van Hove singularity (for Z polarizations) or below the TO′ Van Hove singularity (for in-plane polarizations) [58].**

The TO′ Van Hove singularity (near 5 meV) represents this same effect for in-plane polarizations [50, 59, 60].

The only information necessary to fully describe an ellipsoidal isofrequency surface of graphite with in-plane isotropy is its intersections with the $\overrightarrow{\Gamma A}$ and $\overrightarrow{\Gamma M}$ vectors. Figure 4.17 presents low-energy experimental dispersion data for graphite at 300 K from Mohr et al. [61] using inelastic X-ray scattering and from Nicklow et al. [51] using coherent inelastic neutron scattering, overlaid onto the reference dispersion relations generated by VASP/PHONON. It is important to note that VASP/PHONON predicts the in-plane propagation phonon modes with high accuracy. In particular, the ZA branch is a near-perfect fit to experimental data. It is also clear that the $\overrightarrow{\Gamma A}$ dispersion curves are undercalculated (in energy), which is consistent

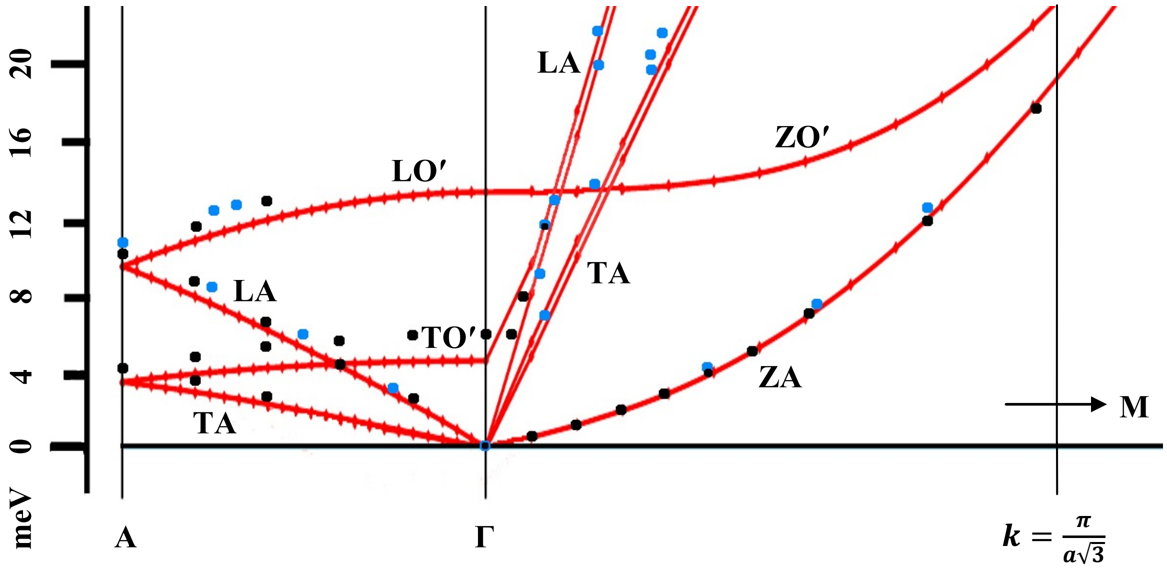

**Figure 4.17 Low-energy dispersion relations for graphite in $\overrightarrow{\Gamma A}$ and $\overrightarrow{\Gamma M}$ directions. Red lines are reference results from VASP/PHONON. Blue dots are experimental data from Mohr et al. [61] using inelastic X-ray scattering. Black dots are experimental data from Nicklow et al. [51] using coherent inelastic neutron scattering.**

with a missing interplanar force component. The goal is to compare the reference total phonon DOS calculated in this work in the region below about 13 meV to the total phonon DOS geometrically calculated from experimental dispersion data.

To geometrically calculate the phonon density of states for one polarization branch with Eq. (4.10) for ellipsoidal isofrequency surfaces, two pieces of information is required. First, the $k$-radius of the ellipsoid in reciprocal space must be described in all directions. The in-plane radius is simply the $k(\omega)$ given by the dispersion curve for a particular polarization in the $\overrightarrow{\Gamma\mathrm{M}}$ direction and the $z$-radius is the same for the $\overrightarrow{\Gamma\mathrm{A}}$ direction. For experimental data, this is determined by interpolation. The second piece of information required is the group velocity $v_{\mathrm{g}}(\omega, \boldsymbol{k})$ in a direction normal to $S(\omega)$ for every point on $S(\omega)$. This can also be mapped geometrically using the known values of $v_{\mathrm{g}}(\omega, \boldsymbol{k}) = \left|\frac{d\boldsymbol{\omega}}{dk_{\perp}}\right|$ in the $\overrightarrow{\Gamma\mathrm{M}}$ and $\overrightarrow{\Gamma\mathrm{A}}$ directions, which is simply the magnitude of the $\frac{d\omega}{dk}$ slope of a dispersion curve at a given $(\omega, k)$. For experimental data, this is also determined by interpolation. An isofrequency surface $S(\omega + \Delta\omega)$ will have $\overrightarrow{\Gamma\mathrm{M}}$ and $\overrightarrow{\Gamma\mathrm{A}}$ radii of $k_{\mathrm{M,A}}(\omega) + \Delta\omega\left(\frac{dk}{d\omega}\right)_{\mathrm{M,A}}$. For a specific small numerical value for $\Delta\omega$, the radii for $S(\omega + \Delta\omega)$ can be calculated in the $\overrightarrow{\Gamma\mathrm{M}}$ and $\overrightarrow{\Gamma\mathrm{A}}$ directions. The outer $S(\omega + \Delta\omega)$ ellipsoid can then be mapped exactly around the inner ellipsoid $S(\omega)$. Next, the normal distance from $S(\omega)$ to $S(\omega + \Delta\omega)$ can be computed for every point on $S(\omega)$, allowing the determination of the group velocity normal to $S(\omega)$ for every point on $S(\omega)$. In the limit as $\Delta\omega \longrightarrow 0$, the resulting group velocity map over $S(\omega)$ converges to the correct map and the phonon density of states for the given polarization branch can be solved. The summation over all three polarization branches (where the two in-plane partials will be identical) yields the total phonon density of states. Since the total phonon DOS is normalized, there is no need to multiply the result by four to account for each basis atom.

To verify the accuracy of the above procedure, the geometric calculation of the phonon density of states for graphite was carried out using numerical reference VASP/PHONON dispersion data in the $\overrightarrow{\Gamma M}$ and $\overrightarrow{\Gamma A}$ directions below the LO′/ZO′ Van Hove singularity and compared to the code-generated reference total phonon density of states. For the in-plane polarizations above the TO′ Van Hove singularity, a cylindrical shape was assumed for the isofrequency surfaces. Figure 4.18 compares the results of the ellipsoidal calculation to the reference VASP/PHONON direct code calculation. The amplitude of the ellipsoidal calculation was fitted to the reference VASP/PHONON calculation to determine the appropriate normalization constant. The fit is seen to be very strong.

The process is now repeated with the experimental data given in Figure 4.17. For the in-plane polarization branches, there is no experimental data from Mohr et al. [61] in the $\overrightarrow{\Gamma A}$ direction (i.e., for the TA and TO′ branches in the $\overrightarrow{\Gamma A}$ direction). Since the parallel phonon density of states is an extremely small component of the total phonon DOS in this low-energy region, the experimental data from Nicklow et al. [51] was substituted. Independent experimental data is available from Mohr at al. for the important LA and LO′ branches in the $\overrightarrow{\Gamma A}$ direction. Figure 4.19 compares both plots in Figure 4.18 to the phonon DOS geometrically calculated from each set of experimental data.

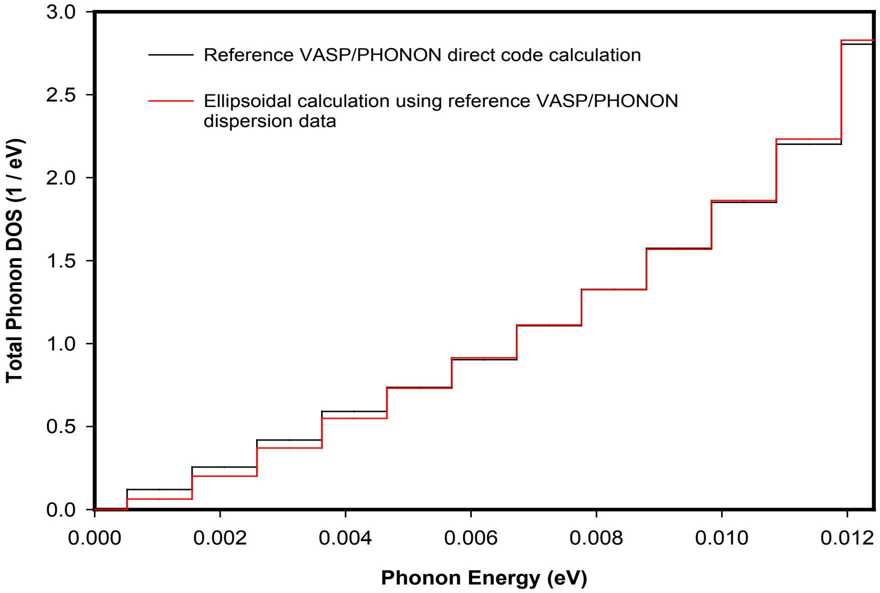

**Figure 4.18** Low-energy comparison of reference phonon DOS calculated directly by VASP/PHONON to phonon DOS calculated using ellipsoidal geometry and VASP/PHONON dispersion data. VASP/PHONON code calculation (black line), geometric calculation (red line).

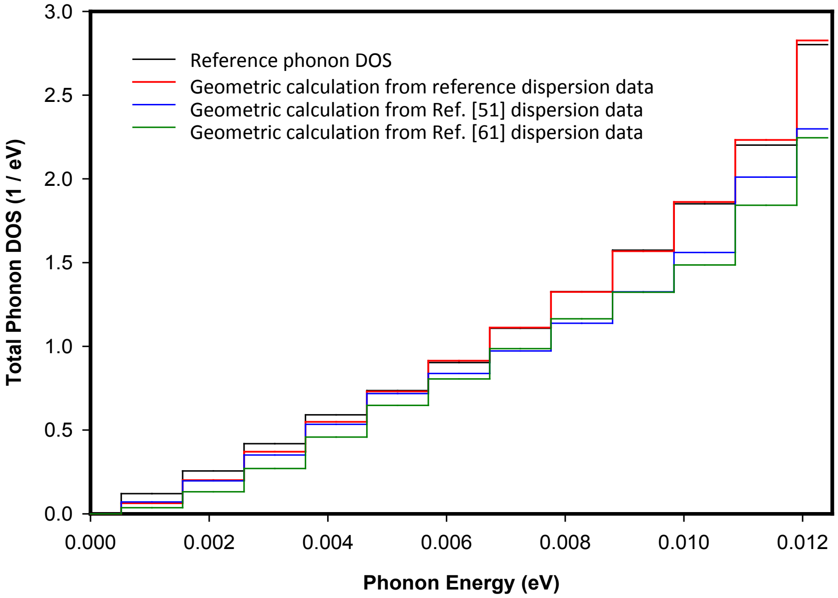

**Figure 4.19** Low-energy phonon DOS for graphite calculated by various methods. Reference VASP/PHONON code result (black line). Ellipsoidal geometry with reference VASP/PHONON dispersion data (red line). Ellipsoidal geometry with Nicklow et al. experimental dispersion data (blue line) [51]. Ellipsoidal geometry with Mohr et al. experimental data (green line) [61].

The $R_3$ function given in Section 3.4.2 (which will now be defined as $R_C$), can be used to operate on $\boldsymbol{p}$ to sample between the minimum and maximum, for each $p_d$, of each of the curves given in Figure 4.19. However, uncertainties in the experimental data must be accounted for. Mohr et al. quotes a single experimental uncertainty of 3 meV in dispersion data [61]. Nicklow et al. provides variable graphical uncertainties for a few select experimental data points [51]. Almost all are for energies above the LO′/ZO′ Van Hove singularity, but an extrapolation of trends to the low-energy region implies uncertainties that are also very close to 3 meV. Since the uncertainty information is limited in both papers, and no correlation information in provided in either case, a strict Type A point-by-point evaluation of uncertainty is not possible.

Physically, the dispersion curves under consideration originate at the Γ-point, are smooth and slowly varying, and are nearly linear or have an expected functional shape. This allows the uncertainty in the dispersion curves to be reasonably treated in terms of amplitude only. Indeed, this interpretation is consistent with the variation seen in a wide variety of experimentally and theoretically calculated dispersion data for this low-energy region. An amplitude uncertainty can now be set that is consistent with an energy uncertainty of about 3 meV over the low-energy region of concern. This is a Type B evaluation of uncertainty. The result is in an uncertainty in the geometrically calculated total phonon DOS of about 20% over the energy region examined. Therefore, in determining the bounds of each $p_d$ for $R_C$ in the Monte Carlo procedure, the two experimental geometric phonon spectra are scaled by ± 20%. Figure 4.20 gives the full region which $R_C$ will sample, accounting

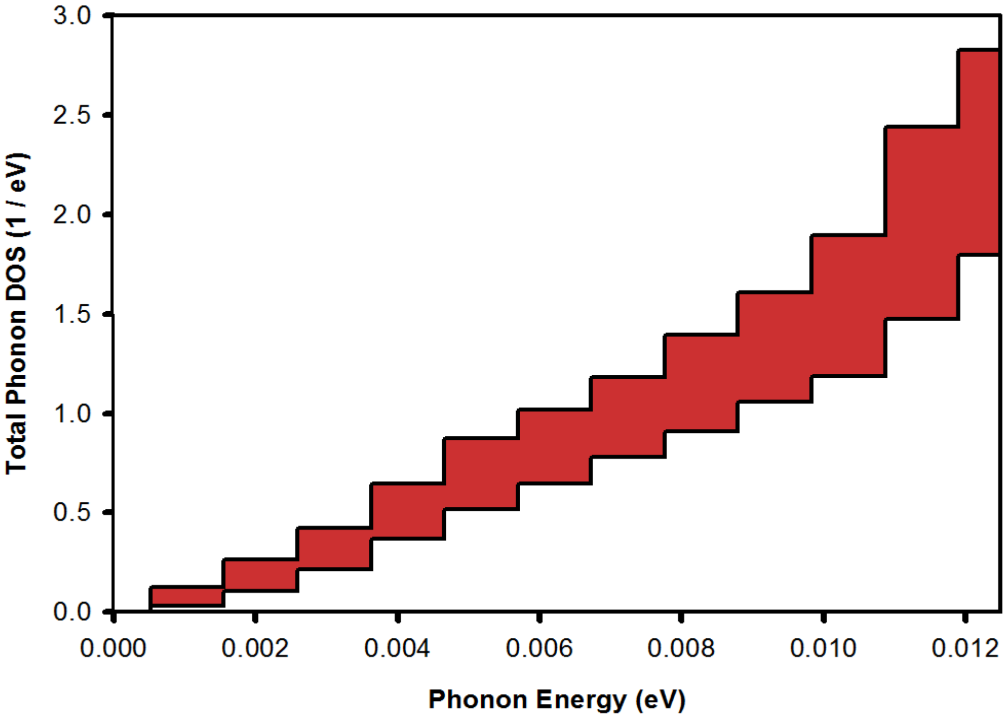

**Figure 4.20 Final region in the graphite phonon DOS below 13 meV sampled by $R_{\mathrm{C}}$, accounting for each of the curves given in Figure 4.19 as well as experimental uncertainty.**

for all of the curves in Figure 4.19 as well as experimental uncertainty. This region describes the full scope of variation determined to be possible in the total phonon density of states for graphite in the region below 13 meV.

### 4.5.4 Total Uncertainties in the Phonon Density of States

The uncertainties described in Sections 4.5.2.1 – 4.5.3.3 can now be combined to generate a perturbed total phonon DOS $\tilde{\boldsymbol{p}} = normalize[R_{\mathrm{C}}R_{\mathrm{B}}R_{\mathrm{A}}(\boldsymbol{p})]$. The order of application of the $R$-functions can be important. In this case, the Type 1 uncertainty ($R_{\mathrm{A}}$) must be modeled first since it is based directly on the reference phonon DOS. The remaining Type 2 uncertainties

($R_{\mathrm{B}}$ and $R_{\mathrm{C}}$) can be applied in either order since the $p_d$ they modify do not overlap. However, in principle, $R_{\mathrm{C}}$ should be applied last since it models uncertainty external to VASP/PHONON. After the application of all $R$-functions, the resulting spectrum is renormalized to give $\tilde{\boldsymbol{p}}$.

Figure 4.21 gives the correlation matrix $\boldsymbol{C_p}$ generated through $N = 500$ Monte Carlo samples of $\tilde{\boldsymbol{p}}$. The structure of the correlation matrix reflects that of the phonon DOS as well as the $R$-functions employed in its generation. In the upper left-hand corner, a plateau of

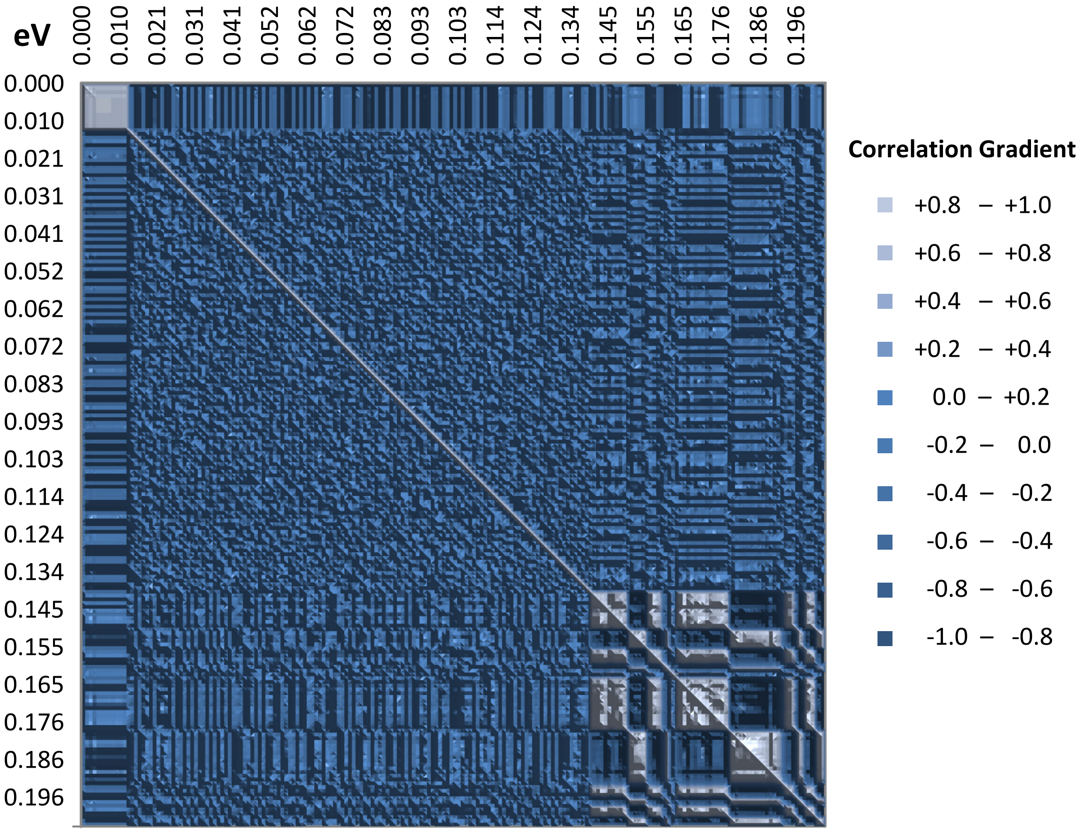

**Figure 4.21 Correlation matrix $C_p$ calculated for the graphite phonon DOS using $N = 500$ Monte Carlo samples of perturbed phonon spectra $\tilde{\boldsymbol{p}}$.**

high correlation reflects the coupling of $p_d$ when $R_\mathrm{C}$ samples within the region defined in Figure 4.20. The interior of the matrix has only random fluctuations, since only statistical uncertainties are modeled for intermediate energies. The high-correlation block structure in the lower right-hand corner is due to the large peaks present in the region above 140 meV where $R_\mathrm{B}$ is being applied.

The relative uncertainty in each $p_d$ resulting from the application of all $R$-functions and renormalization is plotted in Figure 4.22. Significant uncertainties are evident in the high-sensitivity region sampled by $R_\mathrm{C}$ below the LO′/ZO′ Van Hove singularity. The low flat uncertainties at intermediate energies are due to statistical fluctuations in $p_d$ modeled by $R_\mathrm{A}$. At the upper energy region of the DOS, the uncertainties are generally proportional to the slope of the spectrum as the features are being shifted in energy by $R_\mathrm{B}$.

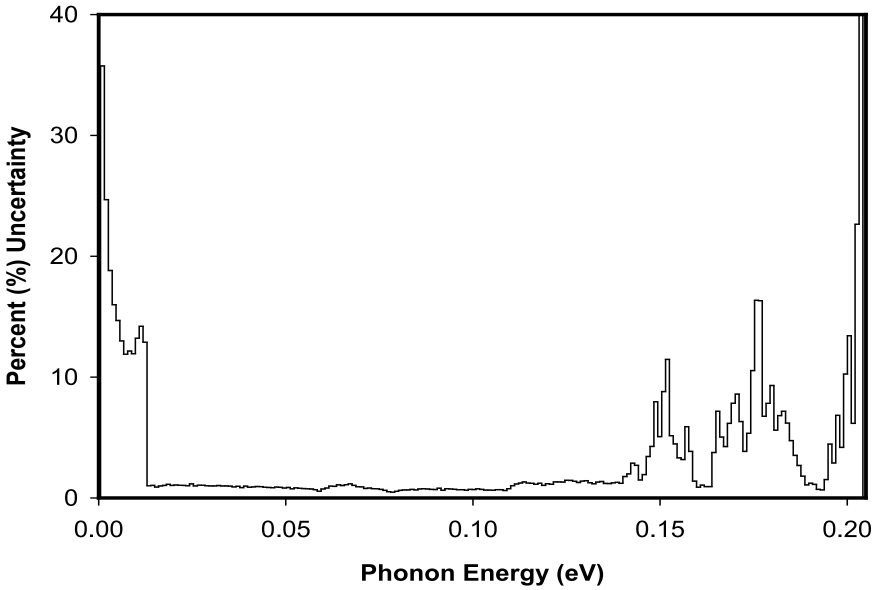

**Figure 4.22 Relative uncertainty in the graphite phonon DOS calculated using $N = 500$ Monte Carlo samples of perturbed phonon spectra $\widetilde{p}$.**

The characteristics of $\boldsymbol{C_p}$ and uncertainties in $p_d$ will be propagated and apparent in the Monte Carlo calculations of the thermal scattering law, differential cross sections and integrated inelastic cross sections. Furthermore, an uncertainty of about 10.5% in the Debye-Waller coefficient $\lambda$ will contribute broadly to propagated uncertainties.

## 4.6 Calculated Uncertainties in the Thermal Scattering Law $\boldsymbol{S_{\mathrm{sym}}(\alpha,\beta)}$

The thermal scattering law $S_{\mathrm{sym}}(\alpha,\beta)$, or $\boldsymbol{s}$, is calculated at 293.6 K for graphite as described in Section 2.2, using a 110-point $\beta$-grid and 70-point $\alpha$-grid, for each of 500 Monte Carlo trials. A phonon order of $n = 22$ (which provides convergence of the integrated inelastic cross section to within 1 millibarn for incident energies up to about 1 eV), is incorporated in the following Monte Carlo calculations to reduce the computational expense of the standard phonon order $n = 100$ (which provides the same convergence up to about 4 eV). The resulting covariance and correlation matrices each have $70^2 \times 110^2 = 5.929 \times 10^7$ elements and contain five-dimensional information (two $\alpha$-dimensions, two $\beta$-dimensions and one magnitude dimension). For better visualization, three-dimensional cross sections of $\boldsymbol{C_s}$ are plotted (instead of $\boldsymbol{V_s}$), where either the $\alpha$ or $\beta$ dimension is fixed. Covariances are set to zero when any associated $S_{\mathrm{sym}}(\alpha,\beta)$ is $< 1 \times 10^{-10}$. Therefore, the large bands of zero correlation in the $\boldsymbol{C_s}$ plots highlight where corresponding elements of $\boldsymbol{V_s}$ have extremely low importance.

Results for the correlation matrix are presented for a variety of fixed $\alpha$ and fixed $\beta$ cases to exhibit the topography and qualities of $\boldsymbol{C_s}$ (and implicitly $\boldsymbol{V_s}$) as a function of scattering probability, multiphonon scattering, and the applied $R$-functions for 500 Monte Carlo trials. Each correlation matrix cross section is followed by a plot giving a visual of the high, low and average Monte Carlo values calculated for $S_{\text{sym}}(\alpha, \beta)$, where "high" refers to the $+1\sigma$ result, "low" refers to the $-1\sigma$ result and "average" is the Monte Carlo mean. Next, the relative uncertainty for fixed $\alpha$ or $\beta$ (as appropriate) is plotted, and a short discussion of the three graphs follows. All graphs with variable $\beta$ are plotted as a function of energy transfer (eV) to facilitate comparison with the reference phonon DOS and the $R$-functions employed. The energy axes run the full length of the associated $\beta$ in the $\beta$-grid employed, where a maximum $\beta = 75$ is used (corresponding to 1.8975 eV for 293.6 K).

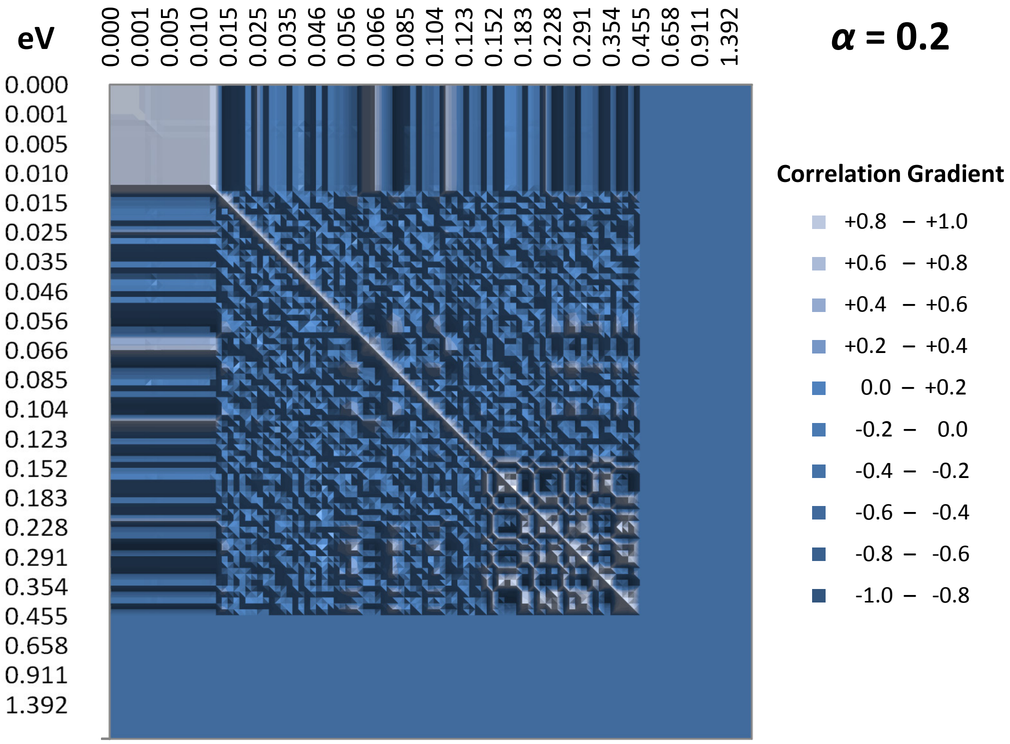

**Figure 4.23** $S_{\text{sym}}(\alpha, \beta)$ **correlation matrix for** $\alpha = 0.2$**.**

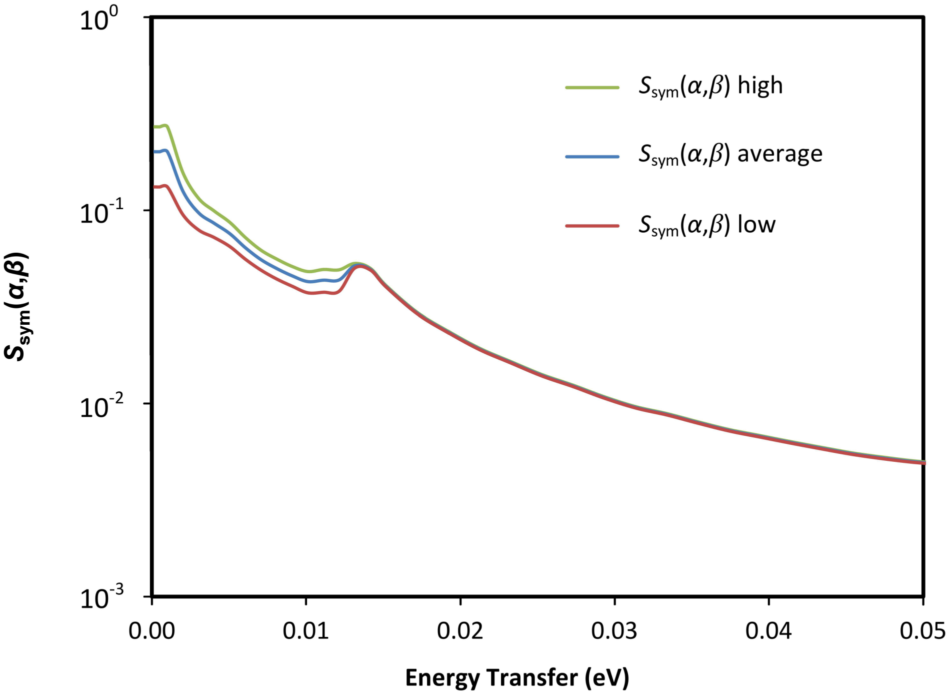

**Figure 4.24 Monte Carlo high, average and low bands for $S_{\text{sym}}(\alpha, \beta)$ for $\alpha = 0.2$.**

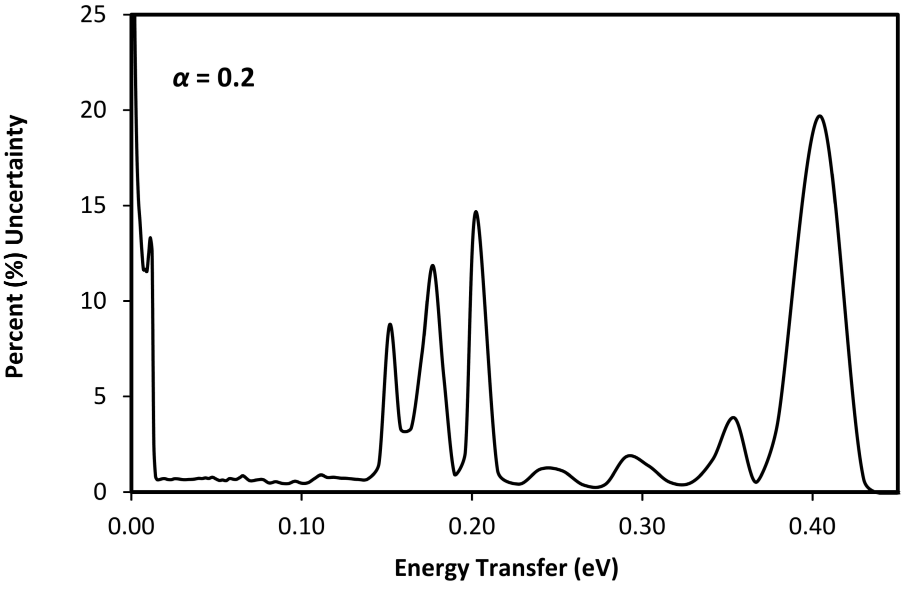

**Figure 4.25 Relative uncertainty for $S_{\text{sym}}(\alpha, \beta)$ for $\alpha = 0.2$.**

For the $\alpha = 0.2$ case given in Figures 4.23 – 4.25, $\boldsymbol{C_s}$ looks very similar to $\boldsymbol{C_p}$ since one-phonon scattering is highly dominant for low $\alpha$. The uncertainties in $S_{\mathrm{sym}}(\alpha,\beta)$ exceed 25% for low $\beta$, for which $S_{\mathrm{sym}}(\alpha,\beta)$ has the highest-valued terms. The $\alpha = 0.2$ case has the highest uncertainties in $S_{\mathrm{sym}}(\alpha,\beta)$ for the three fixed $\alpha$ examples given. Although significant uncertainties also exist in $S_{\mathrm{sym}}(\alpha,\beta)$ at higher $\beta$ (as a result of the $R_{\mathrm{B}}$ reshaping function), the magnitude of $S_{\mathrm{sym}}(\alpha,\beta)$ is quite low at these points, and the associated total uncertainty propagated to integrated inelastic cross sections will be very low.

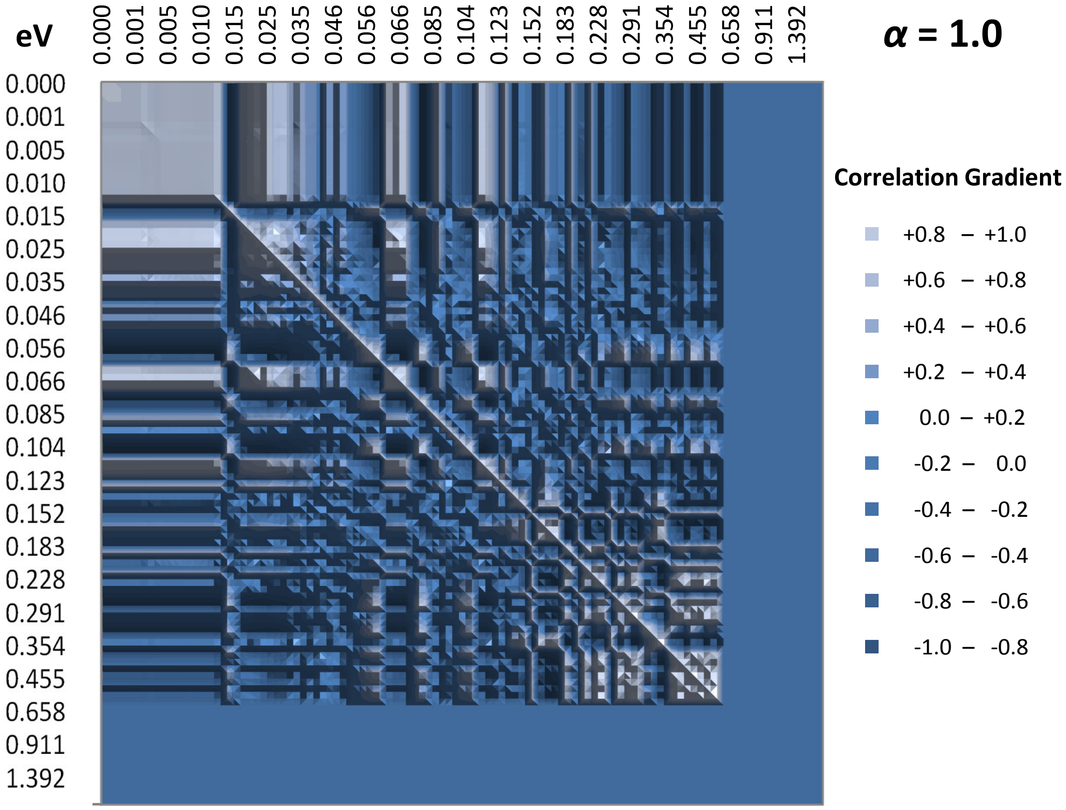

**Figure 4.26 $\boldsymbol{S_{\mathrm{sym}}(\alpha,\beta)}$ correlation matrix for $\boldsymbol{\alpha = 1.0}$.**

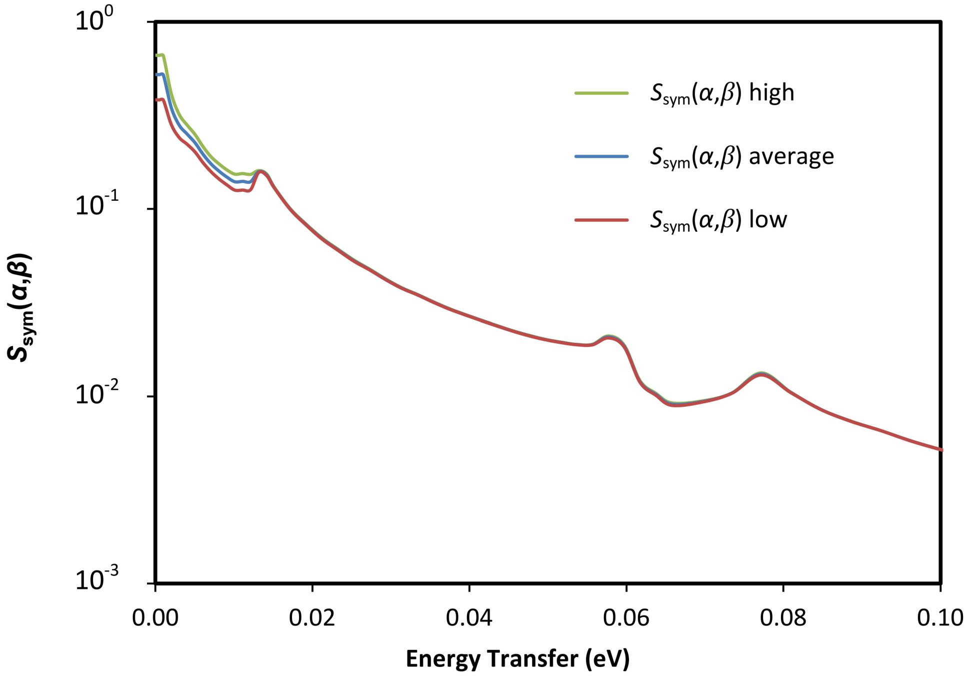

**Figure 4.27 Monte Carlo high, average and low bands for $S_{\mathbf{sym}}(\boldsymbol{\alpha},\boldsymbol{\beta})$ for $\boldsymbol{\alpha} = \mathbf{1.0}$.**

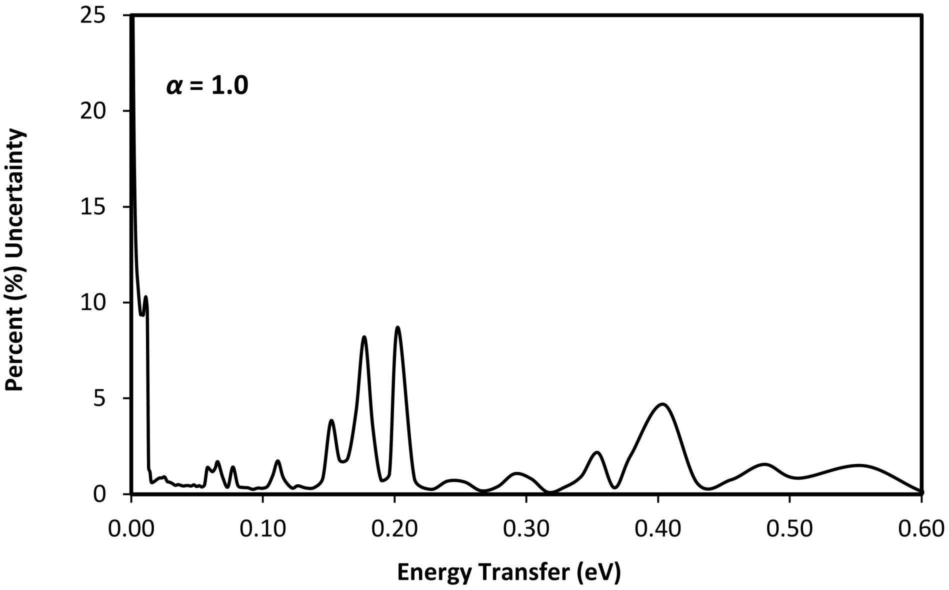

**Figure 4.28 Relative uncertainty for $S_{\mathbf{sym}}(\boldsymbol{\alpha},\boldsymbol{\beta})$ for $\boldsymbol{\alpha} = \mathbf{1.0}$.**

For the $\alpha = 1.0$ case given in Figures 4.26 – 4.28, $\boldsymbol{C_s}$ begins to acquire distinct block characteristics associated with multiphonon scattering. Combinatorial values of energy transfer may have very high or very low probability depending on the phonon occupation number and the particular structure of the phonon spectrum. The random background fluctuations due to $R_\mathrm{A}$ begin to be averaged out. The uncertainties in $S_\mathrm{sym}(\alpha, \beta)$ are slightly smaller than for $\alpha = 0.2$ and tend to be less localized at larger $\beta$. However, uncertainties at the lowest $\beta$ remain dominant due to the high uncertainty in the low-energy region of the phonon density of states modeled by $R_\mathrm{C}$.

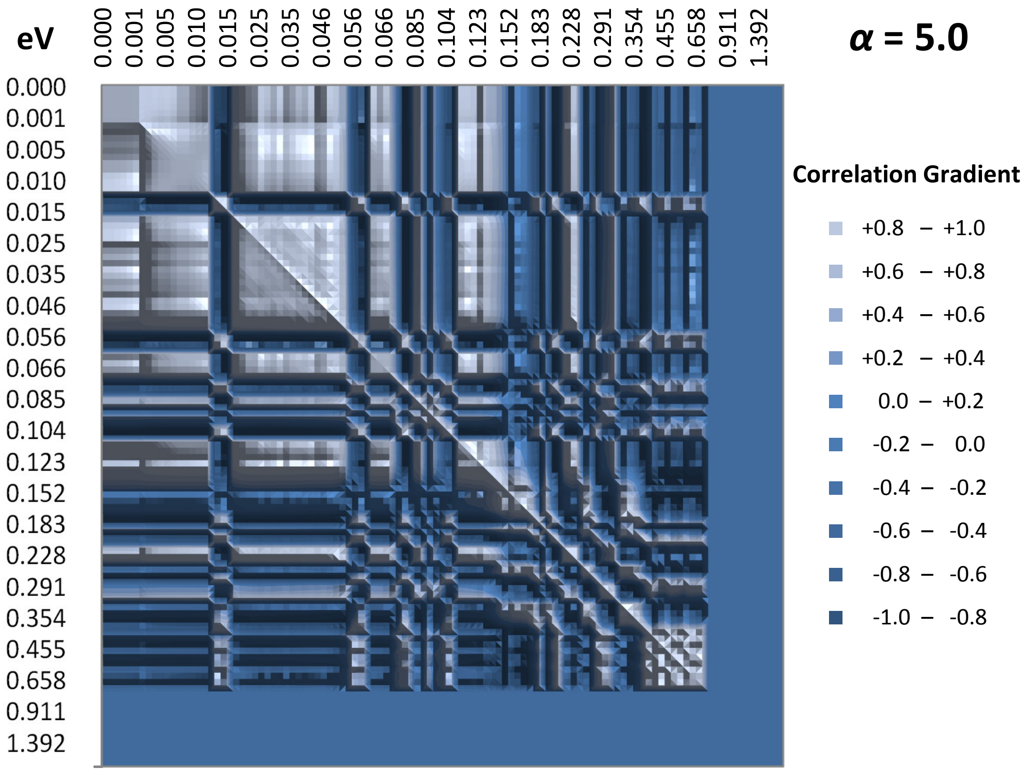

**Figure 4.29** $\boldsymbol{S_\mathrm{sym}(\alpha, \beta)}$ **correlation matrix for** $\boldsymbol{\alpha = 5.0}$**.**

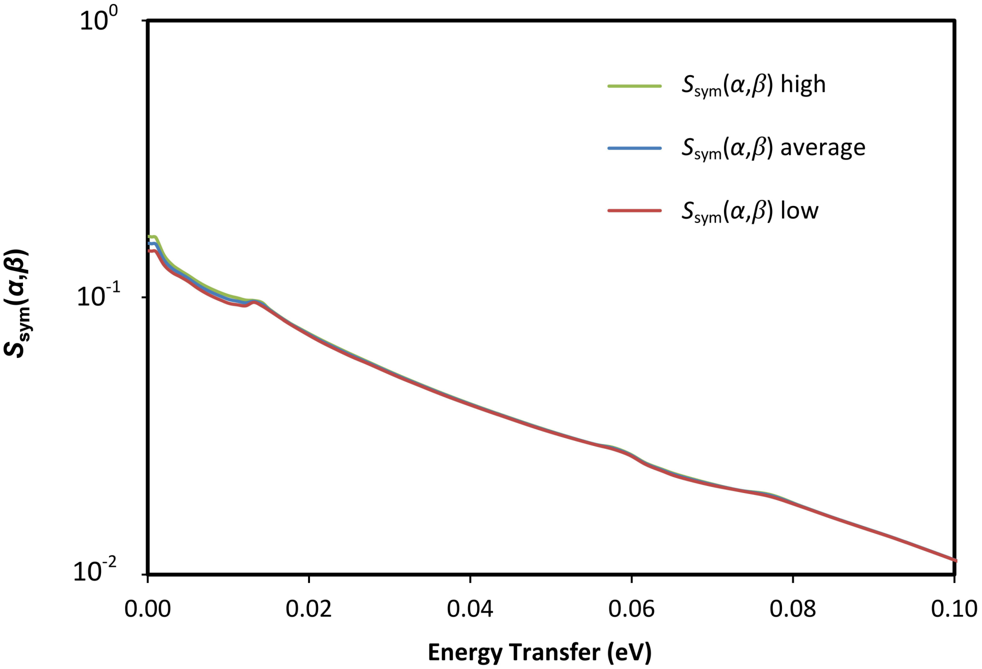

**Figure 4.30 Monte Carlo high, average and low bands for $S_{\mathrm{sym}}(\alpha, \beta)$ for $\alpha = 5.0$.**

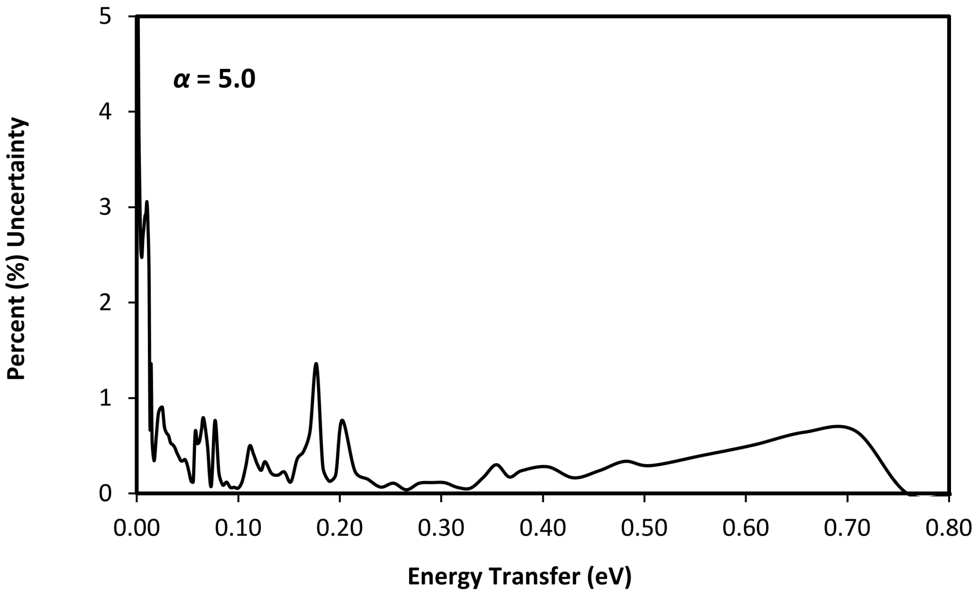

**Figure 4.31 Relative uncertainty for $S_{\mathrm{sym}}(\alpha, \beta)$ for $\alpha = 5.0$.**

For the $\alpha = 5.0$ case given in Figures 4.29 – 4.31, $\boldsymbol{C_s}$ begins to reflect the complete dominance of multiphonon scattering. The block characteristics between energy transfers of related magnitudes associated with multiphonon scattering are pronounced. The small random uncertainties imposed by $R_{\mathrm{A}}$ are no longer visible since one-phonon scattering is mostly absent and the convolutions of multiphonon scattering obscure fine features and fine perturbations of the phonon spectrum. Accordingly, the uncertainties in $S_{\mathrm{sym}}(\alpha,\beta)$ become quite small and very non-localized outside the low-energy $R_{\mathrm{C}}$ sampling region as the impact of individual $p_d$ is marginalized.

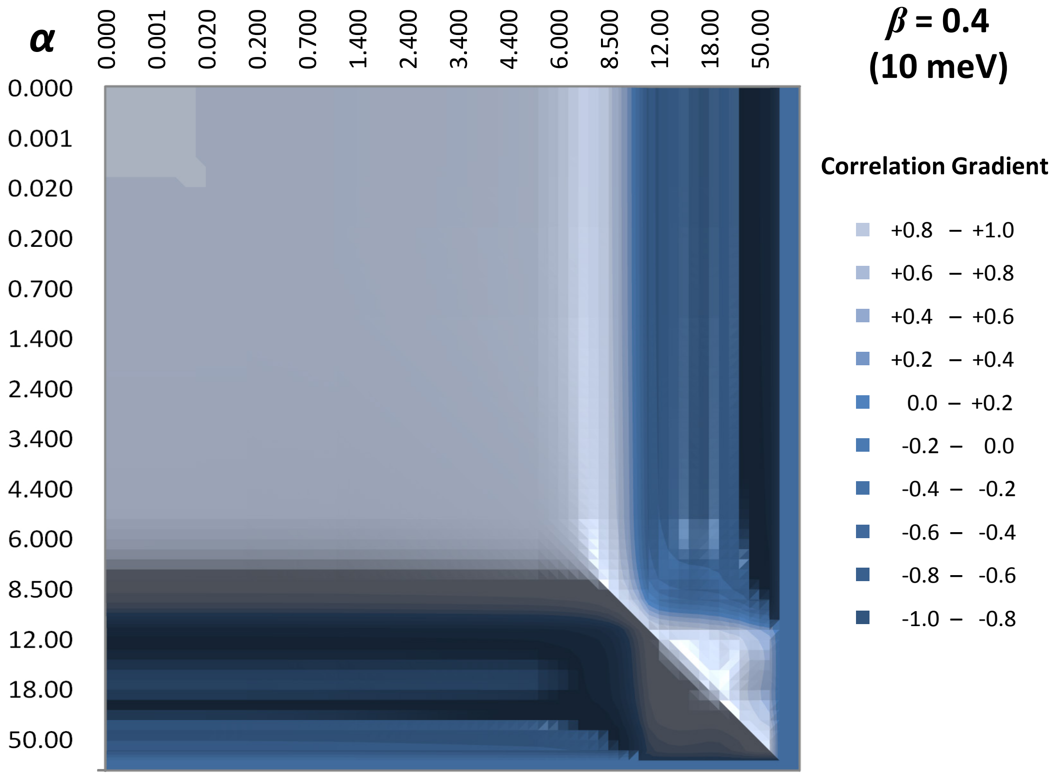

**Figure 4.32** $\boldsymbol{S_{\mathrm{sym}}(\alpha,\beta)}$ **correlation matrix for** $\boldsymbol{\beta = 0.4}$ **(10 meV).**

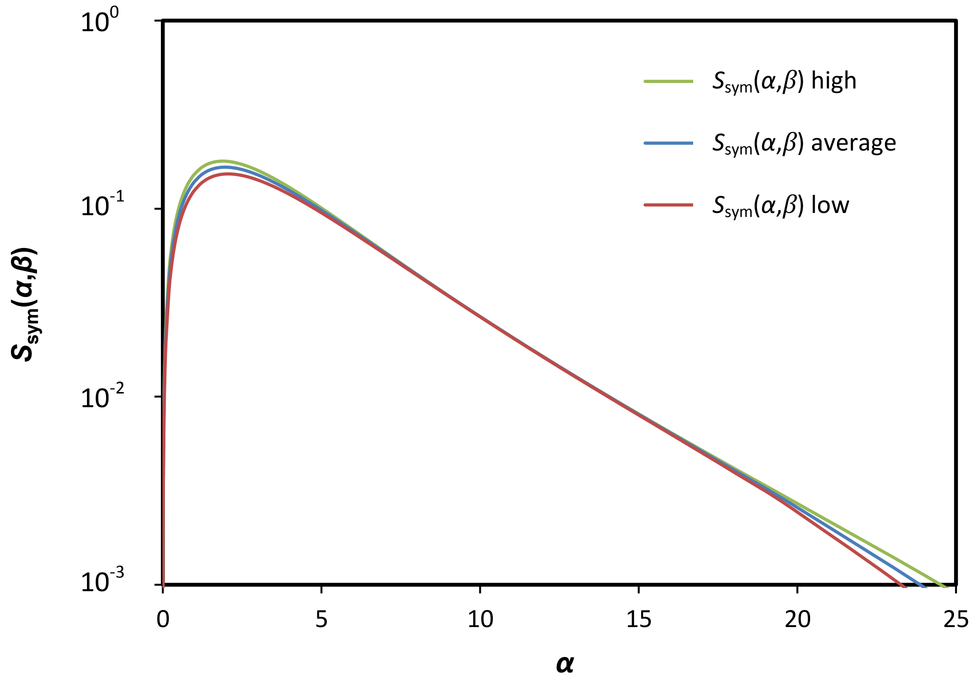

Figure 4.33 Monte Carlo high, average and low bands for $S_{\text{sym}}(\alpha,\beta)$ for $\beta = 0.4$ (10 meV).

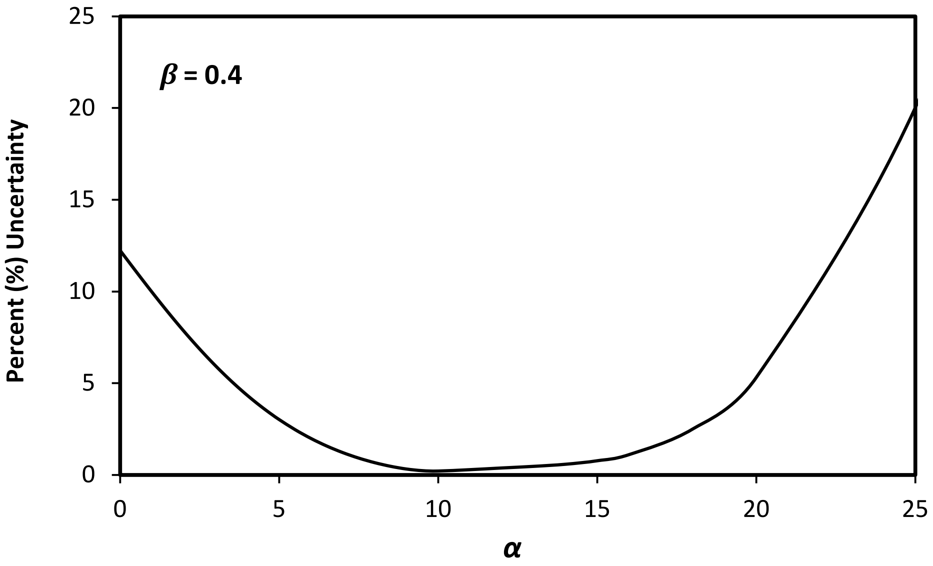

Figure 4.34 Relative uncertainty for $S_{\text{sym}}(\alpha,\beta)$ for $\beta = 0.4$ (10 meV).

For fixed $\beta$ cases, the structure of $\boldsymbol{C_s}$ reflects multiphonon scattering, the magnitude of $S_{\text{sym}}(\alpha,\beta)$ as a function of $\alpha$ and the region of the phonon DOS the $\beta$ is associated with. Individual uncertainties in $p_d$ are not represented since perturbations in the phonon DOS are sampled as a function of $\beta$ (not $\alpha$). Uncertainties in the DOS are manifested through uncertainty in the Debye-Waller factor and through uncertainties in the particular $p_d$ associated (either singly or in combination) with $E(p_d) = \beta k_{\text{B}}T$. The $S_{\text{sym}}(\alpha,\beta)$ for lower $\alpha$ tend to be correlated due to dominance of one-phonon scattering. The $\beta$ = 0.4 case (Figures 4.32 – 4.34) is associated with energy transfers of ~10 meV. The large range of near-perfect correlation is because the $p_d$ associated with many multiphonon energy combinations yielding a 10 meV energy transfer lie within the coupled sampling region for the $R_{\text{C}}$ function.

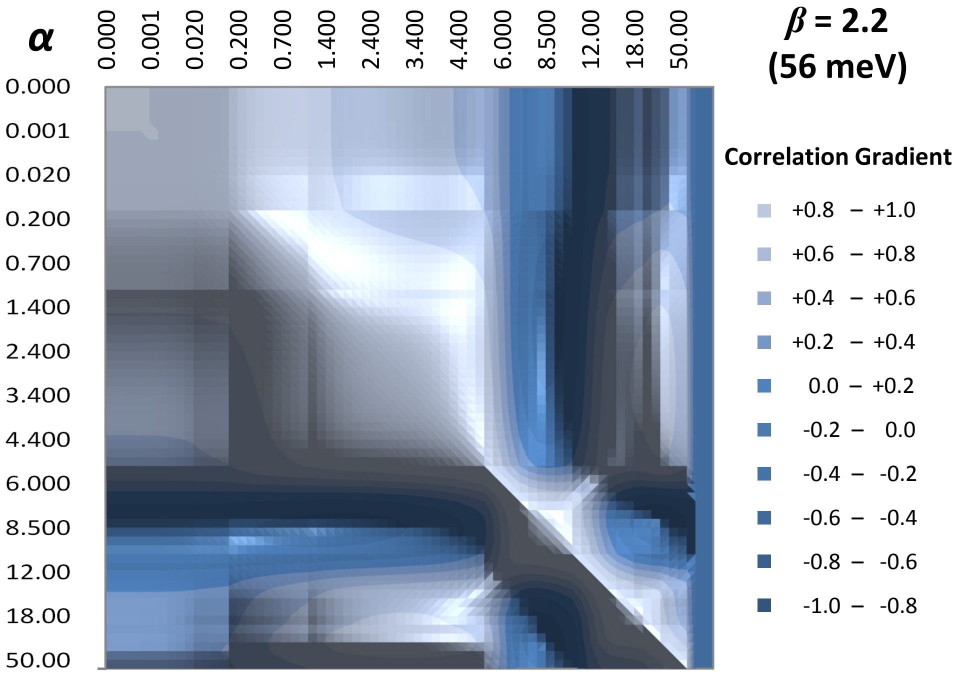

**Figure 4.35** $\boldsymbol{S_{\text{sym}}(\alpha,\beta)}$ **correlation matrix for** $\boldsymbol{\beta = 2.2}$ **(56 meV).**

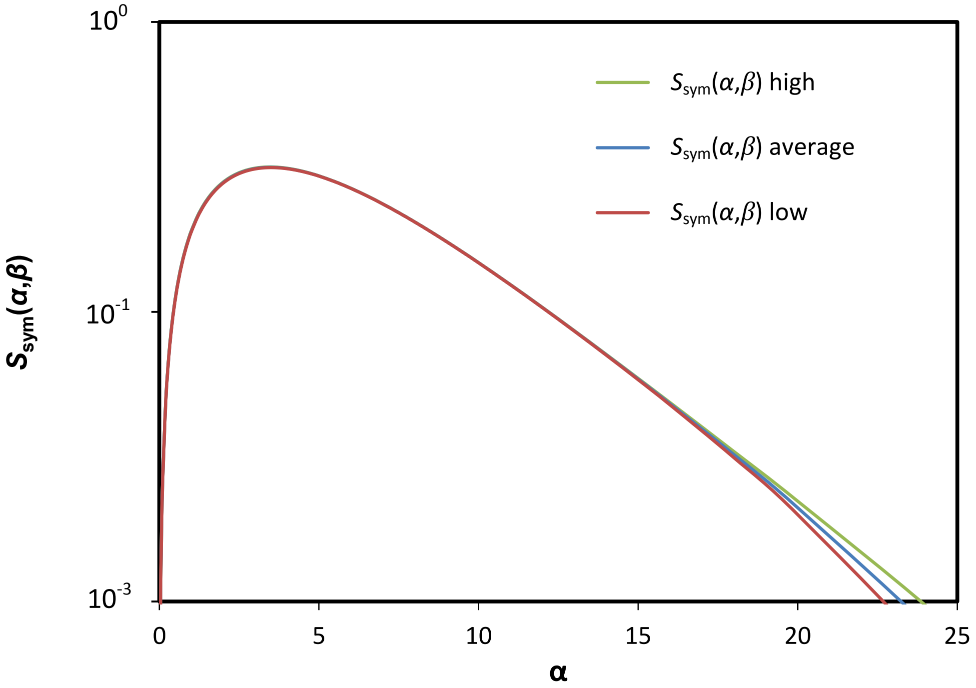

**Figure 4.36** Monte Carlo high, average and low bands for $S_{sym}(\alpha,\beta)$ for $\beta = 2.2$ (56 meV).

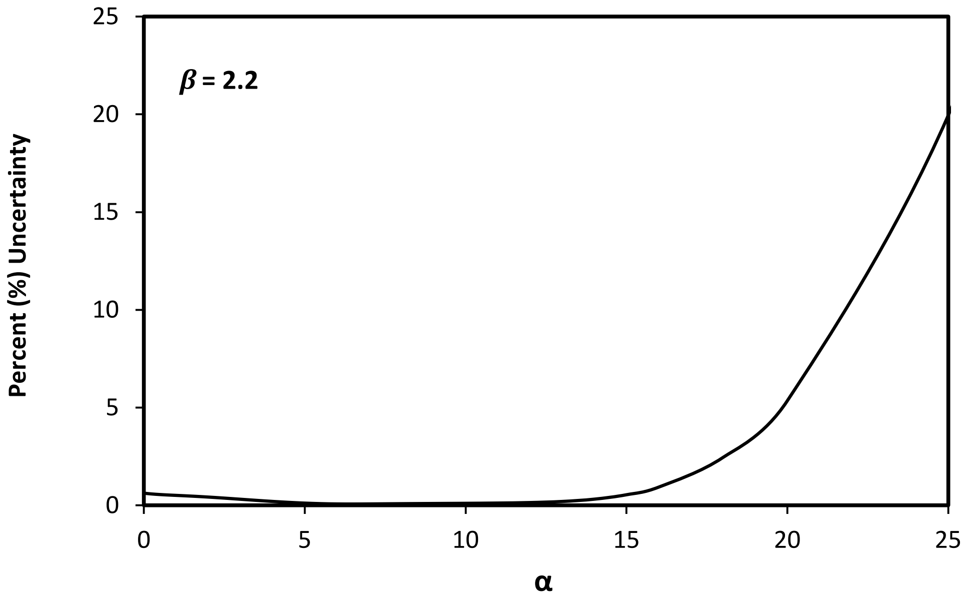

**Figure 4.37** Relative uncertainty for $S_{sym}(\alpha,\beta)$ for $\beta = 2.2$ (56 meV).

The $\beta = 2.2$ case in Figures 4.35 – 4.37 is associated with an energy transfer of ~56 meV that lies just before a Van Hove singularity (see Figure 4.7). The structure of $\boldsymbol{C_s}$ has a smaller high-correlation region than for $\beta = 0.4$ since one-phonon scattering is less probable for a given $\alpha$ for greater $\beta$ and because 56 meV is outside of any $R$-function sampling region. The uncertainty is also much lower in this region for the same reason. $S_{\mathrm{sym}}(\alpha, \beta)$ for lower $\alpha$ are of lower magnitude and correlated due to the contribution of one-phonon scattering to the energy transfer, although much less so than for the $\beta = 0.4$ case. For higher $\alpha$, the relative uncertainty in $S_{\mathrm{sym}}(\alpha, \beta)$ will rise as a function of $\alpha$ as the magnitude of $S_{\mathrm{sym}}(\alpha, \beta)$ rapidly decreases.

While the uncertainties in $S_{\mathrm{sym}}(\alpha, \beta)$ described in the set of examples given provide insight into the expected contributions to differential and integrated cross section uncertainties, the details of the $S_{\mathrm{sym}}(\alpha, \beta)$ covariance matrix will be essential in the propagation of uncertainties. In particular, the formulation given in Eq. (3.15) for directly calculating differential and integrated covariances and uncertainties depends only on the unique properties of $\boldsymbol{V_s}$ (and not on the properties of the sensitivity coefficients – which are defined constants).

## 4.7 Propagated Uncertainties in Differential Cross Sections in Energy (Secondary Neutron Distributions)

The characteristics of the secondary neutron energy distributions and their uncertainties will be similar in many respects to those for $S_{\mathrm{sym}}(\alpha, \beta)$ when mapped over fixed $\alpha$. The secondary distributions are integrated over angle, or over the momentum transfer factor $\alpha$, which is independent of the phonon energy spectrum in the incoherent approximation. Therefore, uncertainties in secondary neutron distributions will retain much of the structure seen in the thermal scattering law. The variation in uncertainties as a function of incident energy will depend on the physical $\alpha$ and $\beta$ limits for scattering, which do not apply for the general calculation of $S_{\mathrm{sym}}(\alpha,\beta)$. Finally, uncertainties in secondary neutron energy distributions will impose uncertainties in the integrated inelastic cross section as well as result in uncertainties in the downscattering to upscattering ratio. The latter can be an important consideration in predicting the equilibrium thermal neutron energy distribution of a nuclear system.

Results will be presented for the incident energies $E$ = 0.0253 eV, 0.1 eV and 0.5 eV. For each incident energy, the Monte Carlo mean differential cross sections will be given along with the relative uncertainties in the differential cross sections. All calculations are for $T$ = 293.6 K. The ranges for each graph will be selected to correspond to the highest probability secondary energies contributing the most to integrated cross sections.

The $E$ = 0.0253 eV = $k_{\mathrm{B}}T$ case in Figures 4.38 – 4.39 is associated with a neutron with incident energy near the thermal energy distribution mean in a system at a temperature of 293.6 K. Upscattering is slightly dominant since the equilibrium energy is $\frac{3}{2}k_{\mathrm{B}}T$. One-phonon scattering accounts for the great majority of the cross section, and uncertainties are almost completely restricted to the region sampled by $R_{\mathrm{C}}$. This also corresponds to the majority of the area under the curve in the distribution. Therefore, essentially all of the uncertainty will be translated to uncertainty in the integrated inelastic cross section.

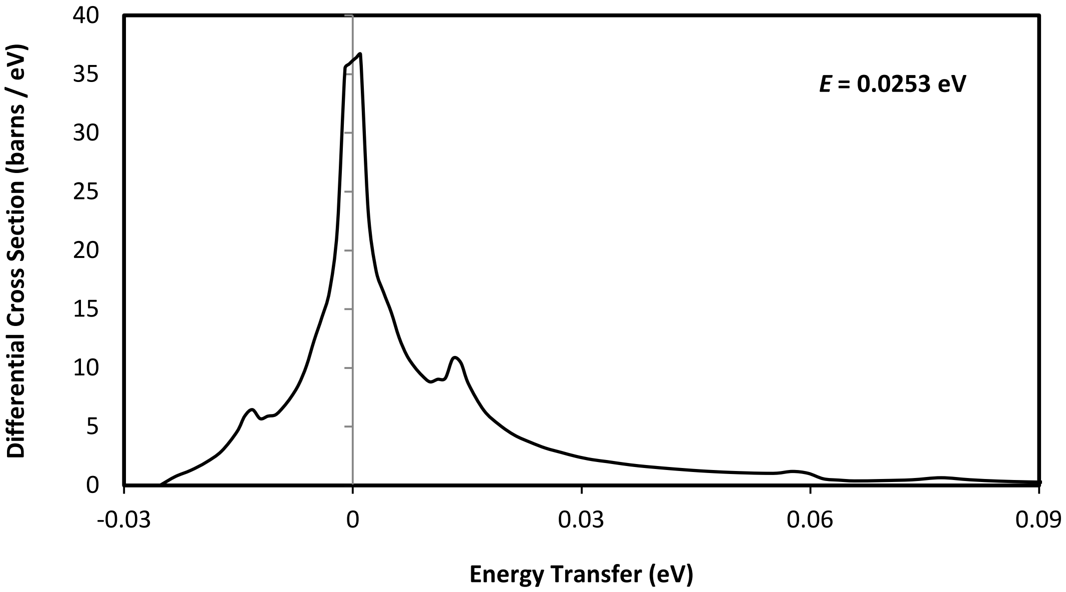

**Figure 4.38** Monte Carlo mean differential cross section in energy at $E = 0.0253$ eV.

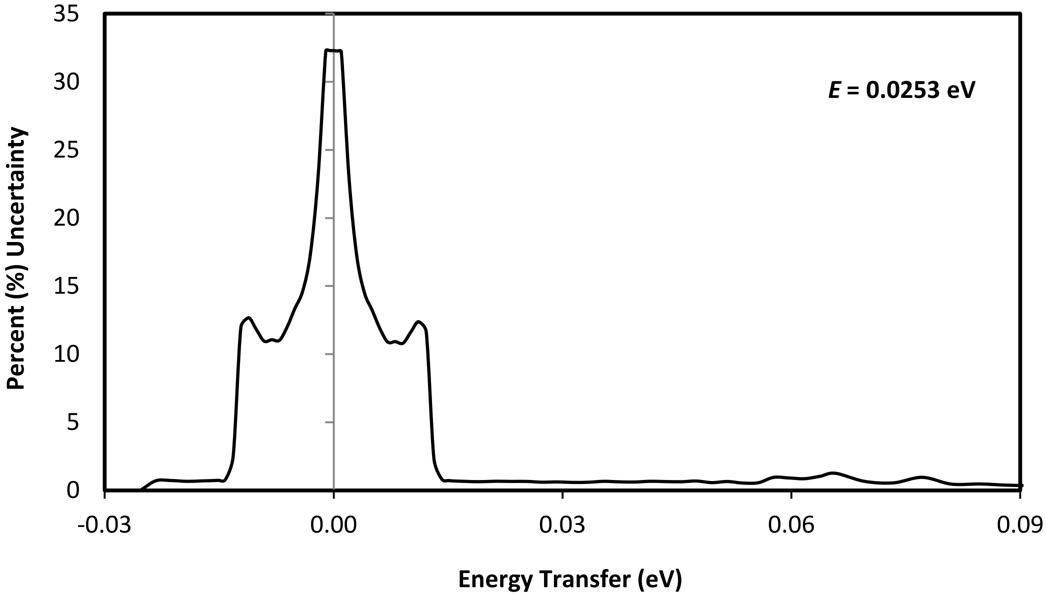

**Figure 4.39** Relative uncertainty in the differential cross section in energy at $E = 0.0253$ eV.

The $E = 0.1$ eV case in Figures 4.40 – 4.41 is similar, except downscattering is more dominant and secondary energies are more widely distributed (scaling differs for each example). Uncertainty is still heavily peaked in the region $R_C$ is sampling, which accounts for the majority of the area under the distribution curve, but a slight increase in uncertainties at higher energy transfers is seen due to multiphonon scattering with high-probability modes. In particular, small peaks near 60 meV and 80 meV are visible, although these will contribute very little to the integrated cross section uncertainty due to the low probability of the events.

The final $E = 0.5$ eV case in Figures 4.42 – 4.43 displays heavily dominant downscattering with a widely distributed secondary distribution. The uncertainties in the $R_C$ range are still peaked, but at a smaller magnitude than the previous cases. Furthermore, considerable structure is evident in the downscattering uncertainties in regions of the secondary distribution retaining significant magnitude.

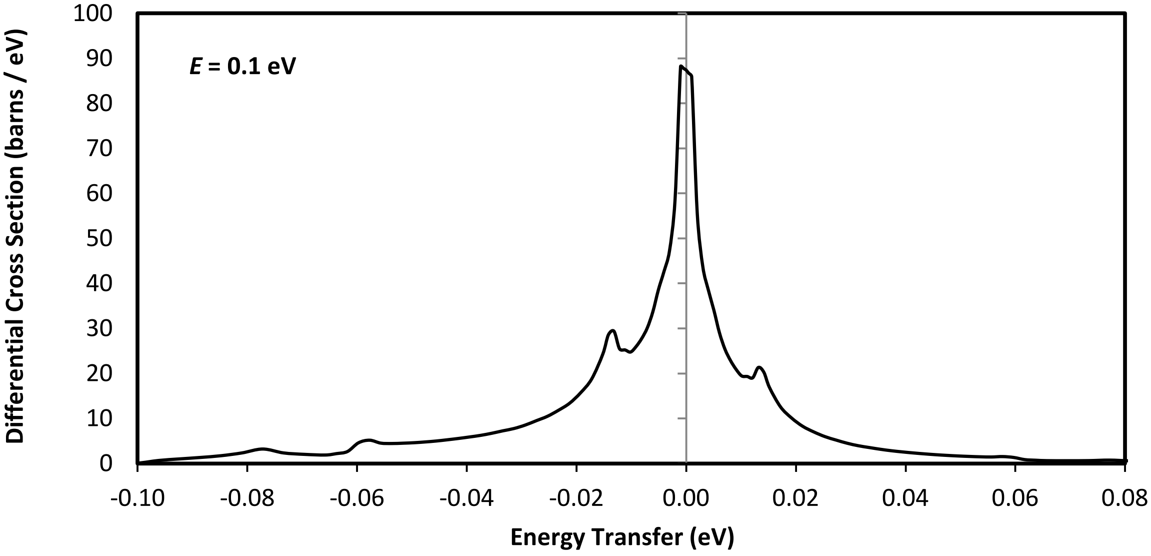

**Figure 4.40 Monte Carlo mean differential cross section in energy at $E = 0.1$ eV.**

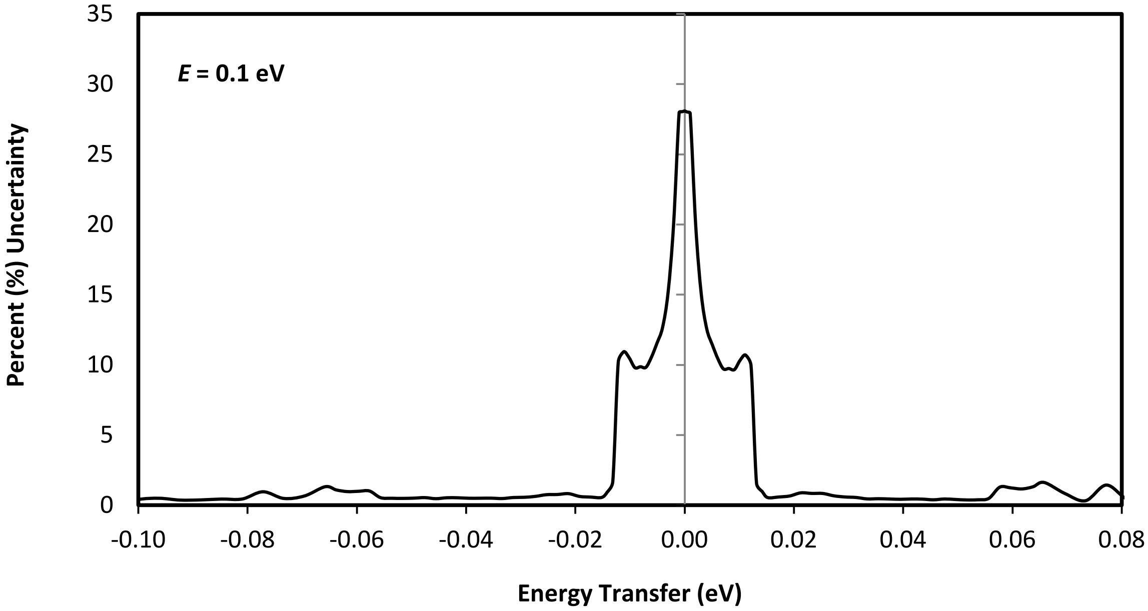

**Figure 4.41** Relative uncertainty differential cross section in energy at $E = 0.1$ eV.

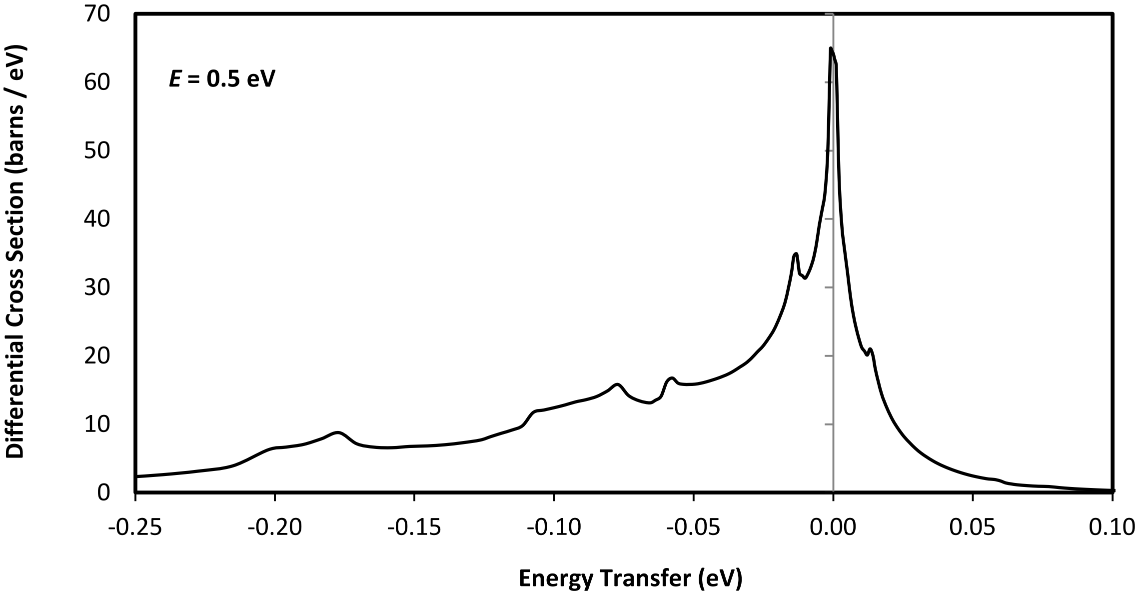

**Figure 4.42** Monte Carlo mean differential cross section in energy at $E = 0.5$ eV.

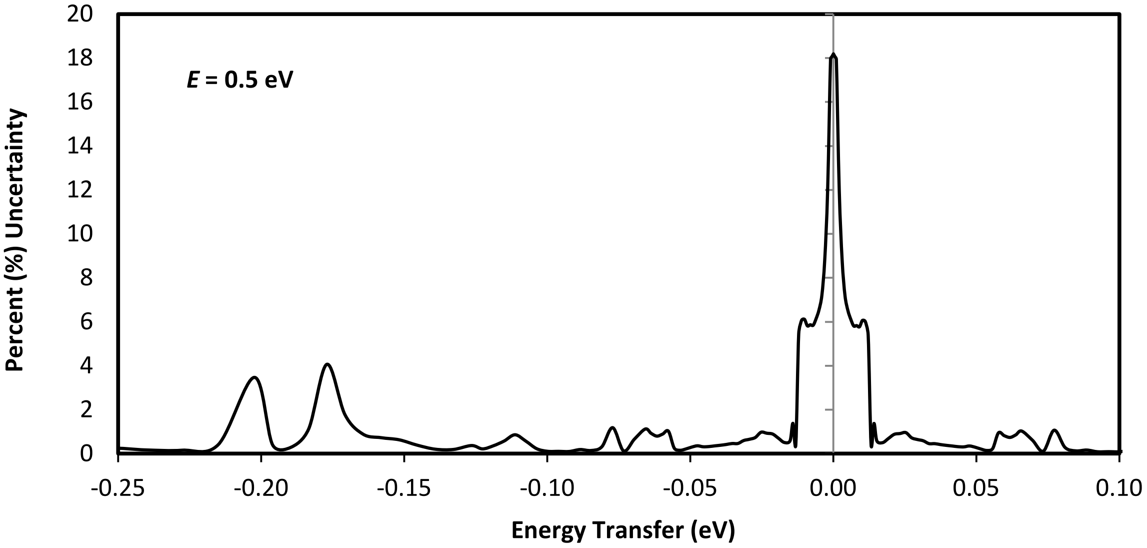

**Figure 4.43 Relative uncertainty in differential cross section in energy at $E = 0.1$ eV.**

## 4.8 Propagated Uncertainties in Integrated Inelastic Cross Sections

Uncertainties in the integrated inelastic cross sections for graphite calculated with the given $R$-function and Monte Carlo methodology are presented. These uncertainties are particular to the physics models employed in producing the phonon density of states for graphite as well as the uncertainty analyses incorporated. For example, in this work, low-energy regions of the phonon DOS are highly correlated due to the characteristics of the $R_{\mathrm{C}}$ sampling process. This property does not necessarily hold in general. Care should be exercised in drawing any general conclusions about the expected magnitudes of uncertainties in integrated cross sections.

It is usually the case that uncertainties in the integrated cross sections will be highly correlated even when individual $p_d$ in the phonon DOS are not. Physically, this is because any particular perturbation in the phonon DOS will, in general, move most or all integrated cross sections in the same direction. Clearly, any particular change in the Debye-Waller factor can only move all integrated cross sections in the same direction. In this work, correlations among all integrated cross sections are 97% or greater. For integrated cross sections theoretically calculated in the incoherent approximation with a supplied total phonon DOS, the details of their correlations may be relatively unimportant once their particular uncertainties have been described. Yet, a description of covariances (and correlations) in the double-differential thermal scattering law data is essential to accurately determining these integrated inelastic cross section uncertainties.

Figure 4.44 plots the $\pm 1\sigma$ Monte Carlo range calculated for the integrated inelastic cross section for graphite at 293.6 K and compares the results to the ENDF/B-VII evaluation [21, 22]. The Monte Carlo range gives the expected variation in the integrated cross sections based the application of the $R$-functions described in Sections 4.5.2.1 – 4.5.3.3 to the reference phonon DOS. Again, while the reference phonon DOS was the basis for the perturbations, the cross section data provided for ENDF evaluations must be the Monte Carlo mean for the quoted uncertainties to be statistically consistent.

Figure 4.45 plots the relative uncertainty in the Monte Carlo calculated integrated inelastic cross section. Note that uncertainties are highest (about 14%) in the incident energy region about $k_B T$ = 0.0253 eV associated with the 293.6 K material temperature. Therefore, the $\pm 1\sigma$ band represents a variation in the integrated cross section of about 28%. Uncertainties at high incident energies are extremely low because they only take into account uncertainties in the phonon DOS (and scattering is almost entirely multiphonon). In theory, any arbitrary

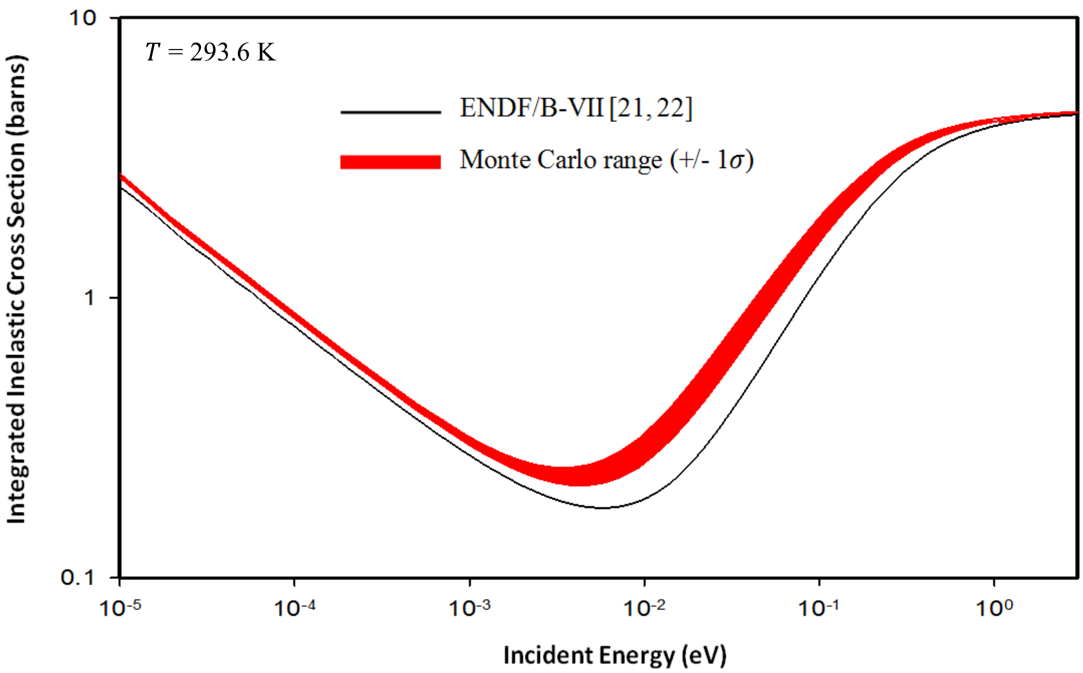

**Figure 4.44 Monte Carlo range (+/- 1$\sigma$) for the integrated inelastic cross section for graphite at compared to the ENDF/B-VII evaluation [21, 22].**

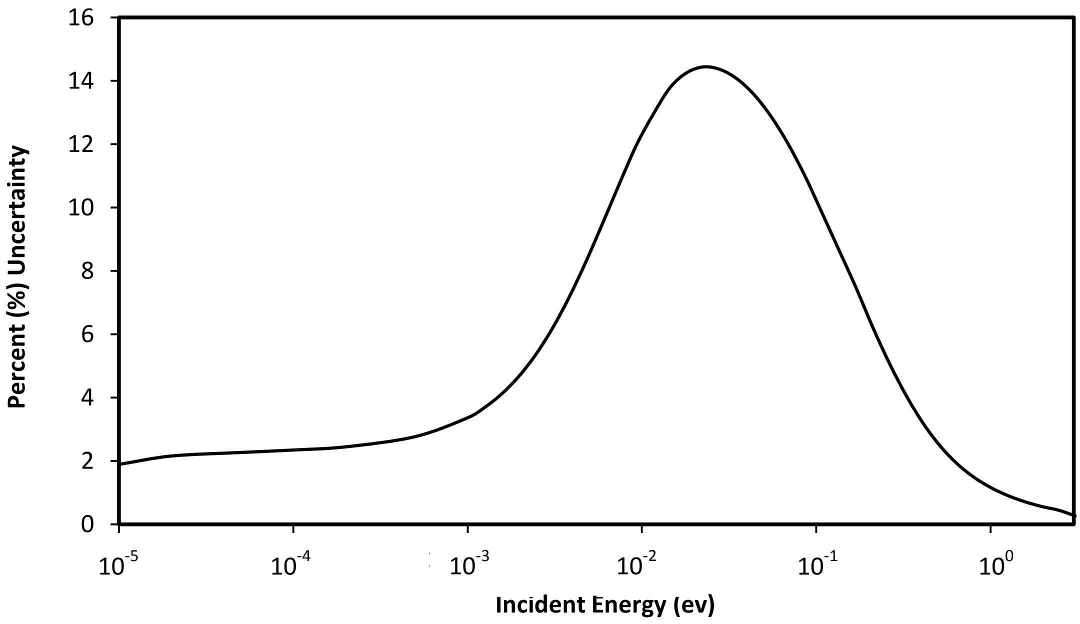

**Figure 4.45 Propagated uncertainty in the graphite integrated inelastic cross section.**

phonon DOS should yield convergence with the free cross section for a sufficiently high phonon-order calculation. However, the total uncertainty can never be reduced below the known uncertainty in the bound nuclear cross section, which is about 0.5% for C-12 [13].

Uncertainties have been calculated based on the application of three separate $R$-functions. It is instructive to examine the contributions of each $R$-function separately. Of the resulting integrated uncertainties, the $R_{\mathrm{C}}$ function sampling the low-energy region of the phonon DOS contributes approximately 92% of the magnitude. Statistical uncertainties modeled by $R_{\mathrm{A}}$ contribute about 7.5% and the systematic uncertainties in the upper-energy region modeled by $R_{\mathrm{B}}$ contribute about 0.5%. It should be pointed out that the very small energy shift imposed by $R_{\mathrm{B}}$ is not primarily responsible for the very small contribution to integrated uncertainties. As an arbitrary example, amplifying the shift by a factor of ten only increases the contribution to 2%. Any perturbations in this upper-energy region of the phonon DOS have almost no impact on propagated uncertainties. Most importantly, differential and integrated cross sections will have high sensitivity to any kind of variation in the low-energy region of the phonon DOS. Therefore, the modeling of physical phenomena that influence this low-energy region is one of the greatest potential sources of cross section uncertainty and should always be investigated carefully.

# Chapter 5

# Conclusions and Future Work

It has long been recognized that the uncertainties inherent in supplied nuclear data can contribute significantly to uncertainties in the calculated response parameters in simulated nuclear systems. The nuclear data community has been involved in data covariance evaluations for several decades. The ENDF nuclear data library format is an international standard for which formats and procedures for covariance evaluations are well established. At present, no thermal scattering covariance data exists in published ENDF evaluations. Additionally, no standard format or procedures exist for representing covariances for ENDF File 7 thermal scattering law data or for differential and integrated thermal cross section data.

In thermal reactors and other nuclear systems where thermal neutrons represent a significant fraction of the neutron population, system response parameters may be very sensitive to the thermal neutron energy distribution. Both integrated and differential thermal neutron scattering cross sections play a fundamental role in determining the characteristics of this distribution. Consequently, small changes (or uncertainties) in the cross section data can potentially impact the accurate calculation of reaction rates, design parameters and safety margins.

## 5.1 The Phonon Density of States and Monte Carlo: A Basis for Describing Describing Thermal Scattering Uncertainties

By convention, published ENDF File 7 inelastic scattering law data, $S(\alpha,\beta)$, is calculated in the incoherent approximation by phonon expansion using a single total phonon density of states (or excitation spectrum) for each chemical element in the material and for each temperature requested. Integrated and differential inelastic cross sections are determined by integration over $S(\alpha,\beta)$. For many nuclear engineering applications, this methodology is physically appropriate, and the phonon spectrum is the fundamental parameter which determines the thermal scattering law and resulting cross sections. Therefore, quantifying uncertainties in thermal scattering cross sections generated by this conventional method requires an understanding and description of uncertainties in the phonon DOS.

The phonon density of states is a dynamic property of the material structure. Its particular features depend on the interatomic potentials of the structure. There are many possible methods of determining the phonon density of states. These methods may contain both theoretical and experimental components. Any uncertainties in the phonon spectrum will be intimately tied to the particular methodology and information used in its generation.

It is of interest to have a generalized method for determining and expressing uncertainties in the phonon DOS that is independent of how it was calculated. The phonon DOS is typically defined piecewise as a probability density function describing the population of phonon modes with energies that lie within uniformly-spaced energy bins. Parameterizing the spectrum as a function of each energy bin allows uncertainties to be described in the physical context of phonon population density, rather than as a function of methodology-dependent parameters.

Particular aspects of uncertainty in a phonon density of states may be geometrically described in terms of expected variation in the spectral shape of the DOS. This allows the phonon DOS to be operated on by random reshaping functions which reflect specific physical or statistical information regarding the probable energy distribution of the phonon population. After one operation by a collection of reshaping functions followed by renormalization, a perturbed phonon DOS results that is representative of the variation in the spectrum as a function of information possessed by the evaluator. Through Monte Carlo sampling, this process may be used to estimate a joint probability density function for the constituent energy bin parameters of the phonon spectrum.

Finally, either through formal propagation of uncertainty or by continued Monte Carlo analysis, a covariance matrix for $S(\alpha,\beta)$, or $S_{\text{sym}}(\alpha,\beta)$, can be produced. With this information, it is a straightforward mathematical exercise to calculate covariances and uncertainties for differential and integrated scattering cross sections.

Like many uncertainty and covariance evaluations, the success of this procedure rests with the ability of the evaluator to make sound scientific judgments in assessing and mathematically describing the nature of uncertainties present. As with many experimental measurements, Type 2 systematic uncertainties will typically be dominant and require careful analysis to account for properly. Fundamentally, it is the physics of the molecular system that defines the phonon density of states. Therefore, the ability to accurately account for the physics (whether through first-principles calculations or through interpreting experimental measurement data) will be the fundamental source of uncertainty that must be considered.

## 5.2 A Generalized Interpretation of the Graphite Example Results

In the example analysis given for graphite, a very detailed investigation of the physics of the structure of graphite was conducted. In particular, the ability of the density functional theory and lattice dynamics methods employed to accurately model this physics was assessed in the context of calculating the phonon density of states. While the particular sources of uncertainty in the example are specific to the graphite problem, several important conclusions can be drawn that apply generally to the phonon DOS of any material produced by any method.

Most importantly, there will always be a high sensitivity of the differential and integrated cross sections to the specific features (and uncertainties in those features) of the low-energy region of the phonon spectrum, even at high temperatures. At relatively low temperatures, the practical impact of particular features of the phonon spectrum on cross sections is almost entirely restricted to the low-energy region. In general terms, the population of low-energy phonons emerges as a function of relatively weak and long-range atomic interactions and the presence of heavier nuclei. The ability to model the uncertainties involved in quantifying the low-energy region will be essential in accurately representing uncertainties in differential and integrated cross sections.

Regardless of the material or nature of uncertainties modeled, differential cross section uncertainties will always be larger than integrated cross section uncertainties. Indeed, this is typically the case for experimental measurements as well. Differential cross section uncertainties result in uncertainties in the particular distribution of scattered neutrons, in the final integrated cross sections, and in the upscattering to downscattering ratio. Uncertainties in the differential cross sections in energy will always be closely related to the specific features of the phonon density of states and their particular uncertainties. Only uncertainties for the highest-probability scattering events are significant. Generally, this corresponds to low energy-transfer events.

Uncertainties in integrated cross sections will always be peaked in the neighborhood of $E \approx k_{\mathrm{B}}T$. This is also the region in which the thermal neutron energy distribution of a physical nuclear system will be peaked. Therefore, this results in a natural amplifying effect for the propagation of nuclear data uncertainties to system response parameters. For higher incident energies, multiphonon scattering is dominant. The effect of multiphonon scattering is to “smooth out” any resolved uncertainty information for the phonon spectrum. Thus, in the limit of high energy, the uncertainty in the integrated inelastic cross section is reduced to that of the associated bound nuclear cross section.

Although the general behavior of integrated cross section uncertainty can be predicted independent of the material being examined, the magnitude of the uncertainty will be closely tied to the details of the uncertainties modeled in the phonon density of states.

## 5.3 Future Work

There are two important classes of issues which will need to be addressed to arrive at a fully comprehensive and standardized methodology for treating thermal scattering uncertainties. First, $S(\alpha,\beta)$ has historically been calculated in the incoherent approximation because this yields a very good estimate for cross sections in many practical situations. However, there are still many situations where this treatment is problematic. Second, in order for users to be able to apply uncertainty and covariance information for the thermal scattering law and cross sections, the evaluated covariance data needs to be accessible in a reasonable format. This work has focused on the theoretical generation of covariance data. From a user standpoint, it is necessary to consider the vast quantities of data involved and the need for a practical storage mechanism.

### 5.3.1 Moving Beyond the Incoherent Approximation

The ENDF File 7 format for $S(\alpha,\beta)$ is general and not specific to any method of calculating $S(\alpha,\beta)$. Therefore, the only limitation in how accurately cross sections can be calculated lies in the accuracy and resolution with which $S(\alpha,\beta)$, or $S_{\text{sym}}(\alpha,\beta)$, is tabulated. For most materials and for most applications of concern, the error introduced in the integrated inelastic cross section due to the use of the incoherent approximation is negligible. There are exceptions to this general rule – graphite is one example. In any case, the error is usually on the order of 10% or less.

As technology and computing resources have progressed, it has become more commonplace to perform detailed and sophisticated first-principles simulations of materials. As one example, the full dynamic structure factor (or the thermal scattering law) may be determined using molecular dynamics. If one assumes that even new advanced methods will always result in some significant uncertainty, the need to generalize the treatment of thermal scattering uncertainties beyond the incoherent approximation will be of interest.

Given the current ENDF File 7 format, there is no obstacle, in principle, to continuing to express thermal scattering uncertainty information in terms of an $S(\alpha,\beta)$ covariance matrix. The methodology of generating this matrix may change, but its applicability will remain. With this understanding, there are two paths possible. One is to cater the generation of an $S(\alpha,\beta)$ covariance matrix to whatever specific new method is employed to calculate $S(\alpha,\beta)$ (which may or may not involve the phonon density of states). The second path is to continue treating uncertainties in $S(\alpha,\beta)$ in terms of the phonon density of states but "add in" the missing components of $S(\alpha,\beta)$ (e.g., the one-phonon coherent interference terms).

Uncertainties and covariances associated with the added terms may be treated explicitly and combined to describe a total covariance matrix for the full thermal scattering law. Alternatively, the added components may be treated as exact. The latter method would have important practical advantages. First, it is likely that the great majority of the uncertainty in integrated cross sections would still be captured through the phonon DOS. The added components would simply serve to remove the bias on the thermal scattering law (and integrated cross sections) imposed by the incoherent approximation. Furthermore, maintaining the phonon DOS as the repository for uncertainty information could greatly reduce storage requirements (and allow a standardized format to be retained) if its covariance matrix was provided to the user instead of that for $S(\alpha,\beta)$.

### 5.3.2 Storing and Processing $S(\alpha,\beta)$ Covariance Data

In ENDF File 7 libraries, $S(\alpha,\beta)$ is tabulated over evaluator-defined $\alpha$ and $\beta$ grids. A 100 × 100 grid is of typical size, yielding $10^4$ elements per temperature requested. A covariance matrix for this information would contain $10^8$ elements. It has been stated that the $S(\alpha,\beta)$ covariance matrix represents the only information required to calculate covariances and uncertainties for any differential or integrated cross section. However, a $10^8$ element matrix directly supplied to the end-user is likely to be too large for practical use. Formats and procedures must be developed to allow for the compression and compact storage of this data while retaining sufficient information to accurately calculate differential and integrated cross section covariances.

Fortunately, the $S(\alpha,\beta)$ covariance matrix contains far more information than is required to accurately predict the uncertainties and covariances for differential and integrated cross sections which will be associated with it. Much of the thermal scattering law data itself will be of very low magnitude, especially at the outer bounds of $\alpha$ and $\beta$. These low-magnitude terms are only necessary for very accurate converged calculations, and any uncertainties in their values are of very low importance from the standpoint of integrated cross sections (as well as the most probable secondary energies for differential cross sections in energy). In terms of propagation of uncertainty, only uncertainties for the highest-valued terms of $S(\alpha,\beta)$, which represent the highest-probability scattering events and the most sensitive parameters, will be of significant consequence. One straightforward method of greatly reducing the $S(\alpha,\beta)$ covariance matrix storage requirements is to simply consider only covariances for $S(\alpha,\beta)$ above a certain threshold. A very large amount of unnecessary data could be eliminated in this fashion with very little impact on the final uncertainty quantification for cross sections.

Alternatively, the $S(\alpha,\beta)$ matrix could be subdivided into a block structure (i.e., over specific $\alpha$ and $\beta$ blocks) with resolution based on the magnitude and variation of the function. Similar to the procedures used to collapse fine energy-group cross section data (and covariances) into coarse energy-group cross section data (and covariances), a group averaging procedure may be applied where covariances are retabulated at the level of the coarse block structure. This procedure could be used in combination with a threshold cutoff to greatly reduce storage requirements without any significant loss of uncertainty information. In particular, $S(\alpha,\beta)$ varies slowly and smoothly over $\alpha$ (as does the associated correlation matrix). Therefore, averaging over $\alpha$ blocks would be quite natural.

Finally, incorporating the ENDF File 30 format, $S(\alpha,\beta)$ covariance data could be provided indirectly by supplying the user with the covariance matrix for the phonon density of states along with appropriate sensitivity matrices. Although some loss of information would be inevitable, the qualitative difference in calculated cross section uncertainties would likely be insignificant and well justified for the massive reduction in storage requirements. This procedure has particular appeal because it may allow a generalized format for expressing and storing thermal scattering covariance information to be retained even if the ENDF File 7 format is changed in the future or if coherent interference terms are added in.

# REFERENCES

[1] A. Trkov, M. Herman and D. A. Brown (Eds.), "ENDF-6 Formats Manual," CSEWG Document ENDF-102, BNL-90365-2009 Rev. 2, National Nuclear Data Center, Brookhaven National Laboratory, Upton, New York (2011).

[2] N. E. Holden, "A Short History of Nuclear Data and Its Evaluation," *Cross Section Evaluation Working Group Meeting, "A CSEWG Retrospective,"* Upton, New York (2001).

[3] S. Pearlstein, "Cross Section Evaluation Working Group History," *Cross Section Evaluation Working Group Meeting, "A CSEWG Retrospective,"* Upton, New York (2001).

[4] C. Dunford, "Some CSEWG Recollections," *Cross Section Evaluation Working Group Meeting, "A CSEWG Retrospective,"* Upton, New York (2001).

[5] F. G. Perey, "Expectations for ENDF/B-V Covariance Files: Coverage, Strength and Limitations," *A Review of the Theory and Application of Sensitivity and Uncertainty Analysis*, Oak Ridge, Tennessee (1979).

[6] E. Fort, J. Rowlands and M. Salvatores, "Covariance Data Requirements," *Proceedings of a Specialists' Meeting on Evaluation and Processing of Covariance Data*, Oak Ridge, Tennessee (1992).

[7] D. W. Muir, "The Covariance Files of ENDF/B," *Cross Section Evaluation Working Group Meeting, "A CSEWG Retrospective,"* Upton, New York (2001).

[8] S. A. W. Gerstl, "Uncertainty Analysis for Secondary Energy Distributions," *A Review of the Theory and Application of Sensitivity and Uncertainty Analysis*, Oak Ridge, Tennessee (1979).

[9] H. Vonach, "Direct Covariance Data for Coupled Energy-Angle Distributions," *Proceedings of a Specialists' Meeting on Evaluation and Processing of Covariance Data*, Oak Ridge, Tennessee (1992).

[10] M. J. Embrechts, "SENSIT-2D: A Two-Dimensional Cross-Section Sensitivity and Uncertainty Analysis Code," LA-9515-MS, Los Alamos National Laboratory, Los Alamos, New Mexico (1982).

[11] T. J. Seed, "TRIDENT-CTR User's Manual," LA-7835-M, Los Alamos Scientific Laboratory, Los Alamos, New Mexico (1979).

[12] Oak Ridge National Laboratory, "SCALE: A Comprehensive Modeling and Simulation Suite for Nuclear Safety Analysis and Design, Version 6.1," ORNL/TM-2005/39, Oak Ridge National Laboratory, Oak Ridge, Tennessee (2011).

[13] M. B. Chadwick, P. G. Young and C. Y. Fu, "ENDF/B-VII.1 MAT 600," Los Alamos National Laboratory, Los Alamos, New Mexico (2006).

[14] D. W. Muir, D. L. Smith, A. Trkov and R. Capote, "Summary of IAEA Technical Meeting on Neutron Cross-Section Covariances," *IAEA Technical Meeting on Neutron Cross-Section Covariances*, Vienna, Switzerland (2010).

[15] G. L. Squires, *Introduction to the Theory of Thermal Neutron Scattering*, Dover Publications, Mineola, New York (1996).

[16] H. Schober, "Putting Neutron Scattering Into Perspective," *European Conference on Neutron Scattering*, Grenoble, France (2013).

[17] I. I. Al-Qasir, "Thermal Neutron Scattering in Graphite," Ph.D. Dissertation, North Carolina State University, Raleigh, North Carolina (2007).

[18] A. I. Hawari, I. I. Al-Qasir, V. H. Gillette, B. W. Wehring and T. Zhou, "Ab Initio Generation of Thermal Neutron Scattering Cross Sections," *PHYSOR-2004 – The Physics of Fuel Cycles and Advanced Nuclear Systems: Global Developments*, Chicago, Illinois (2004).

[19] A. I. Hawari and I. I. Al-Qasir, "Graphite Thermal Neutron Scattering Cross Section Calculations Including Coherent 1-Phonon Effects," *PHYSOR-2008 – Nuclear Power: A Sustainable Resource*, Interlaken, Switzerland (2008).

[20] R. E. MacFarlane, D. W. Muir, R. M. Boicourt and A. C. Kahler, "The NJOY Nuclear Data Processing System, Version 2012," LA-UR-12-27079, Los Alamos National Laboratory, Los Alamos, New Mexico (2012).

[21] R. E. MacFarlane, "ENDF/B-VII.1 MAT 31," Los Alamos National Laboratory, Los Alamos, New Mexico (2006).

[22] J. A. Young and J. U. Koppel, "Phonon Spectrum of Graphite," *The Journal of Chemical Physics*, **42**, 357-364 (1965).

[23] D. L. Smith, *Probability, Statistics, and Data Uncertainties in Nuclear Science and Technology*, American Nuclear Society, LaGrange Park, Illinois (1991).

[24] B. N. Taylor and C. E. Kuyatt, "Guidelines for Evaluating and Expressing the Uncertainty of NIST Measurement Results," National Institute of Standards and Technology, Washington, D.C. (1994).

[25] D. W. Muir, "Description of Covariances of Emission Spectra Using ENDF File 30," *Proceedings of a Specialists' Meeting on Evaluation and Processing of Covariance Data*, Oak Ridge, Tennessee (1992).

[26] K. Parlinski, Z. Q. Li and Y. Kawazoe, "First-Principles Determination of the Soft Mode in Cubic $ZrO_2$," *Physical Review Letters*, **78**, 4063-4066 (1997).

[27] K. Parlinski, "Software PHONON," K. Parlinski, Cracow, Poland (2002).

[28] S. W. Lovesey, *Theory of Neutron Scattering from Condensed Matter, Volume 1: Nuclear Scattering*, Clarendon Press, Oxford, United Kingdom (1984).

[29] A. J. Koning and D. Rochman, "Towards Sustainable Nuclear Energy: Putting Nuclear Physics to Work," *Annals of Nuclear Energy*, **35**, 2024-2030 (2008).

[30] Los Alamos National Laboratory, "MCNP6.1, Monte Carlo N-Particle Transport Code," Los Alamos National Laboratory, Los Alamos, New Mexico (2013).

[31] R. Machleidt, Q. MacPherson, E. Marji, R. Winzer, C. Zeoli and D. R. Entem, "Recent Progress in the Theory of Nuclear Forces," *Few-Body Systems*, **54**, 821-826 (2013).

[32] P. Descouvemont and D. Baye, "The R-Matrix Theory," *Reports on Progress in Physics*, **73**, 419-461 (2010).

[33] C. M. Mattoon and P. Oblozinsky, "Issues in Neutron Cross Section Covariances," *Journal of the Korean Physical Society*, **59**, 847-850 (2011).

[34] D. L. Smith, "Quality Assurance for ENDF/B-VII.1 Covariances," *Cross Section Evaluation Working Group Meeting*, Santa Fe, New Mexico (2010).

[35] D. L. Smith, "Nuclear Data Uncertainties in 2010: A Perspective," *Journal of the Korean Physical Society*, **59**, 755-760 (2011).

[36] G. Audi, A. H. Wapstra and C. Thibault, "The AME2003 Atomic Mass Evaluation," *Nuclear Physics*, **729**, 337-676 (2003).

[37] M. E. Wieser, N. Holden, T. B. Coplen, J. K. Böhlke, M. Berglund, W. A. Brand, P. de Bièvre, M. Gröning, R. D. Loss, J. Meija, T. Hirata, T. Prohaska, R. Schoenberg, G. O'Connor, T. Walczyk, S. Yoneda and X. Zhu, "Atomic Weights of the Elements 2011 (IUPAC Technical Report)," *Pure and Applied Chemistry*, **85**, 1047-1078 (2013).

[38] P. J. Mohr, B. N. Taylor and D. B. Newell, "CODATA Recommended Values of the Fundamental Physical Constants: 2010," *Reviews of Modern Physics*, **84**, 1527-1605 (2012).

[39] D. L. Roach, D. K. Ross, J. D. Gale and J. W. Taylor, "The Interpretation of Polycrystalline Coherent Inelastic Neutron Scattering from Aluminum," *Journal of Applied Crystallography*, **46**, 1755-1770 (2013).

[40] C. Kittel, *Introduction to Solid State Physics*, John Wiley & Sons, Hoboken, New Jersey (2005).

[41] R. A. Cowley, "Anharmonic Crystals," *Reports on Progress in Physics*, **31**, 123-166 (1968).

[42] N. Bonini, M. Lazzeri, N. Marzari and F. Mauri, "Phonon Anharmonicities in Graphite and Graphene," *Physical Review Letters*, **99**, 176802 (2007).

[43] P. Giura, N. Bonini, G. Creff, J. B. Brubach, P. Roy and M. Lazzeri, "Temperature Evolution of Infrared- and Raman-Active Phonons in Graphite," *Physical Review B*, **86**, 121404 (2012).

[44] L. Paulatto, F. Mauri and M. Lazzeri, "Anharmonic Properties from a Generalized Third Order Ab Initio Approach: Theory and Applications to Graphite and Graphene," *Physical Review B*, **87**, 214303 (2013).

[45] C. Bernardino and L. Bonolis, *Enrico Fermi: His Work and Legacy*, Italian Physical Society, Bologna, Italy (2001).

[46] D. D. DiJulio and A. I. Hawari, "Examination of Reactor Grade Graphite Using Neutron Powder Diffraction," *Journal of Nuclear Materials*, **392**, 225-229 (2009).

[47] G. Kresse and J. Furthmüller, "Efficiency of Ab-Initio Total Energy Calculations for Metals and Semiconductors Using a Plane-Wave Basis Set," *Computational Materials Science*, **6**, 15-60 (1996).

[48] G. Kresse and J. Furthmüller, "Efficient Iterative Schemes for Ab Initio Total-Energy Calculations Using a Plane-Wave Basis Set," *Physical Review B*, **54**, 11169-11186 (1996).

[49] G. Kresse and J. Furthmüller, "Vienna Ab-Initio Simulation Package," Institute of Materials Physics, Wien, Austria (2001).

[50] I. A. Gospodarev, K. V. Kravchenko, E. S. Syrkin and S. B. Feodos'ev, "Quasi-Two-Dimensional Features in the Phonon Spectrum of Graphite," *Low Temperature Physics,* **35**, 589-595 (2009).

[51] R. Nicklow, N. Wakabayashi and H. G. Smith, "Lattice Dynamics of Pyrolytic Graphite," *Physical Review B*, **5**, 4951-4962 (1972).

[52] L. J. Karssemeijer and A. Fasolino, "Phonons of Graphene and Graphitic Materials Derived from the Empirical Potential LCBOPII," *Surface Science*, **605**, 1611-1615 (2011).

[53] L. Wirtz and A. Rubio, "The Phonon Dispersion of Graphite Revisited," *Solid State Communications*, **131**, 141-152 (2004).

[54] N. Mounet and N. Marzari, "First-Principles Determination of the Structural, Vibrational and Thermodynamic Properties of Diamond, Graphite and Derivatives," *Physical Review B*, **71**, 205214 (2005).

[55] Y. Baskin and L. Meyer, "Lattice Constants of Graphite at Low Temperatures," *Physical Review*, **100**, 544 (1955).

[56] G. Savini, Y. J. Dappe, S. Öberg, J. C. Charlier, M. I. Katsnelson and A. Fasolino, "Bending Modes, Elastic Constants and Mechanical Stability of Graphitic Systems," *Carbon*, **49**, 62-69 (2011).

[57] S. V. Dmitriev, J. A. Baimova, A. V. Savin and S. K. Yuri, "Ultimate Strength, Ripples, Sound Velocities, and Density of Phonon States of Strained Graphene," *Computational Materials Science*, **53**, 194-203 (2012).

[58] J. Krumhansl, "The Lattice Vibration Specific Heat of Graphite," *The Journal of Chemical Physics*, **21**, 1663-1669 (1953).

[59] J. Kaspar and E. H. Zehms, "Thermal Diffusivity of Carbons and Graphites in the Temperature Range from 1800 to 3300°K," TR-1001(9250-02)-2, Aerospace Corporation, El Segundo, California (1967).

[60] I. A. Gospodarev, V. I. Grishaev, O. V. Kotlyar, K. V. Kravchenko, E. V. Manchelii, E. S. Syrkin, S. B. Feodosyev, I. K. Galetich and A. V. Yeremenko, "Similarity of the Boson Peaks in Disordered Systems to the Van Hove Singularities in Regular Crystals," B. I. Verkin Institute for Low Temperature Physics and Engineering, National Academy of Sciences of Ukraine, Kharkov, Ukraine (2011).

[61] M. Mohr, J. Maultzsch, E. Dobardžić, S. Reich, I. Milošević, M. Damnjanović, A. Bosak, M. Krisch and C. Thomsen, "Phonon Dispersion of Graphite by Inelastic X-Ray Scattering," *Physical Review B*, **76**, 035439 (2007).

[62] J. Hafner, "Foundations of Density-Functional Theory," Center for Computational Materials Science, Wien, Austria (2003).

# APPENDICES

# Appendix A

## The ENDF MF = 7, MT = 4 Format for the Thermal Scattering Law

The scope of this appendix is limited to a format discussion regarding the $S(\alpha, \beta)$ data tabulated in the MT = 4 section of the ENDF File 7 library [1]. For a theory discussion of $S(\alpha, \beta)$, refer to Sections 2.1 and 2.2. For details regarding the processing of $S(\alpha, \beta)$, refer to Sections 2.2 and 3.2.2.

ENDF File 7 libraries contain thermal neutron scattering law data that depends on a material's molecular structure. There are two MT values associated with MF = 7. MT = 2 contains coherent and incoherent elastic scattering data. Although this can be considered "thermal scattering law" data, the inelastic $S(\alpha, \beta)$ definition for the thermal scattering law will be observed. MT = 4 tabulates $S(\alpha, \beta)$ for specific $T$ over $\alpha$ and $\beta$ grids defined by the evaluator. The terms $\alpha$ and $\beta$ are unitless momentum and energy transfer factors, respectively.

The title of the MT = 4 section is Incoherent Inelastic Scattering. The ENDF File 7 format does not provide any explicit means for tabulating coherent inelastic scattering data. However, the format for MT = 4 is independent of the definition of $S(\alpha, \beta)$. Therefore, the tabulated $S(\alpha, \beta)$ may include coherent one-phonon scattering without adverse effect on the storage or processing of the MT = 4 data. The MT = 4 format does not allow tabulation of the scattering law as a function of the scattering angle. The momentum transfer factor $\alpha$ is a function only of the cosine of the scattering angle in the laboratory frame. The MT = 4 format is specifically designed for randomly oriented microcrystal structure.

Unlike traditional ENDF libraries which contain many different data files for various reaction types, ENDF File 7 is a separate library entirely because it is material-specific and not nuclide-specific. For example, a File 7 library may be associated with any chosen elemental stoichiometry of a compound and with different polymorphic phases or crystal structures of the same material. A File 7 library must be used in combination with the traditional ENDF evaluations for the nuclides represented within.

There are several procedures available to address the numerical issues with handing extremely large and extremely small numbers in the calculation of $S(\alpha,\beta)$ and the issues of storing extremely small numbers or large quantities of data. These include the short collision-time (SCT) approximation for large $\alpha$, rescaling $\alpha$ and $\beta$ as a function of temperature, limiting $\alpha$ and $\beta$ grid resolution, tabulating $\ln[S(\alpha,\beta)]$, and tabulating the symmetric scattering law $S_{\text{sym}}(\alpha,\beta) = S_{\text{sym}}(\alpha,-\beta) = e^{\beta/2}S(\alpha,\beta)$ for positive $\beta$ only. These procedures can be very important when rounding errors on 32-bit or older machines can cause serious numerical problems and when storage capacity and processing power are at a premium. In the widely available 64-bit double-precision, numbers with a precision up to 16 decimal places and with an exponent greater than 300 may be stored. Additionally, storage capacity and processing speed have increased by many orders of magnitude from decades past. Therefore, many of these procedures are no longer strictly necessary and have become a matter of practical convenience.

For the purpose of the uncertainty analysis in this work, the SCT approximation is never used and all $S(\alpha,\beta)$ are computed directly as described in Section 2.2. To facilitate analysis,

$\alpha$ and $\beta$ are not scaled as a function of temperature, although scaling may be appropriate if temperature itself is being considered as an uncertainty variable. The tabulation of $\ln[S(\alpha,\beta)]$ will not be considered. However, the symmetric scattering law, $S_{\text{sym}}(\alpha,\beta)$, is tabulated since this is standard for nearly all published ENDF File 7 libraries. This quantity is the basis for the calculation of covariances.

Like traditional ENDF evaluations, the ENDF File 7 library begins with File 1, MT = 451 administrative information. Figure A.1 displays the first few lines of the published ENDF/B-VII.1 File 7 thermal library for graphite as an example [21]. The locations of the MF, MAT and MT entries are shown. The positions of these entries are universal for all ENDF file blocks. MAT = 31 is the material number for graphite. For thermal moderators, MAT is typically assigned a value between 1 and 99 depending on the material category.

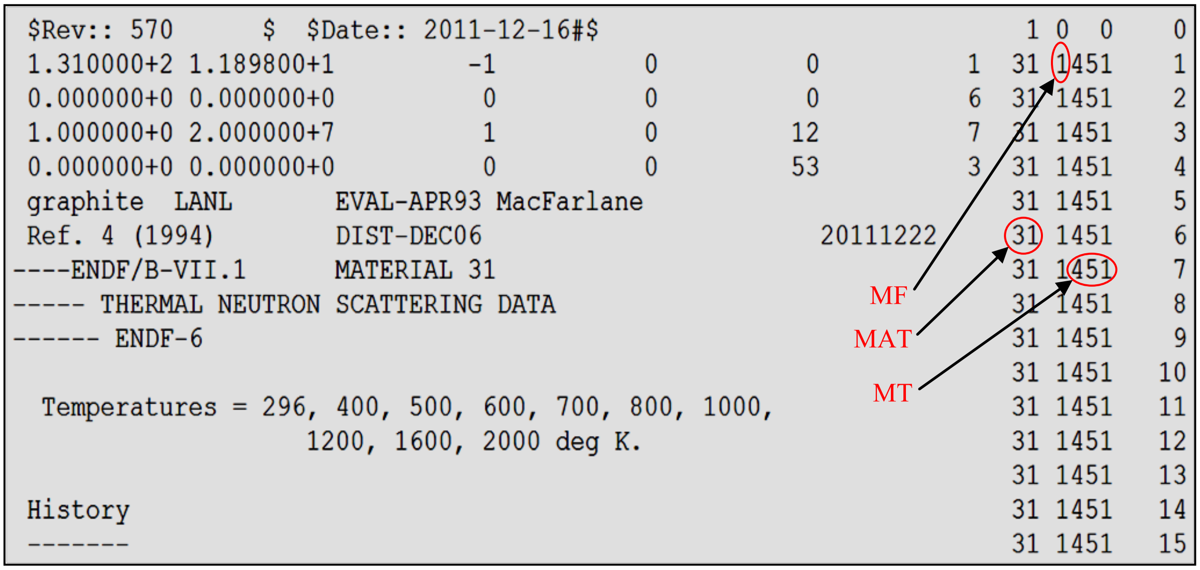

```
 $Rev:: 570      $  $Date:: 2011-12-16#$                         1 0  0    0
 1.310000+2 1.189800+1         -1          0          0          1  31 1451    1
 0.000000+0 0.000000+0          0          0          0          6  31 1451    2
 1.000000+0 2.000000+7          1          0         12          7  31 1451    3
 0.000000+0 0.000000+0          0          0         53          3  31 1451    4
 graphite  LANL       EVAL-APR93 MacFarlane                         31 1451    5
 Ref. 4 (1994)        DIST-DEC06                       20111222     31 1451    6
----ENDF/B-VII.1      MATERIAL 31                                   31 1451    7
----- THERMAL NEUTRON SCATTERING DATA                               31 1451    8
------ ENDF-6                                                       31 1451    9
                                                                    31 1451   10
  Temperatures = 296, 400, 500, 600, 700, 800, 1000,                31 1451   11
                 1200, 1600, 2000 deg K.                            31 1451   12
                                                                    31 1451   13
 History                                                            31 1451   14
 -------                                                            31 1451   15
```

**Figure A.1 First 16 lines of ENDF/B-VII.1 File 7 thermal library for graphite with arrows indicating the location of MF, MAT and MT entries [21].**

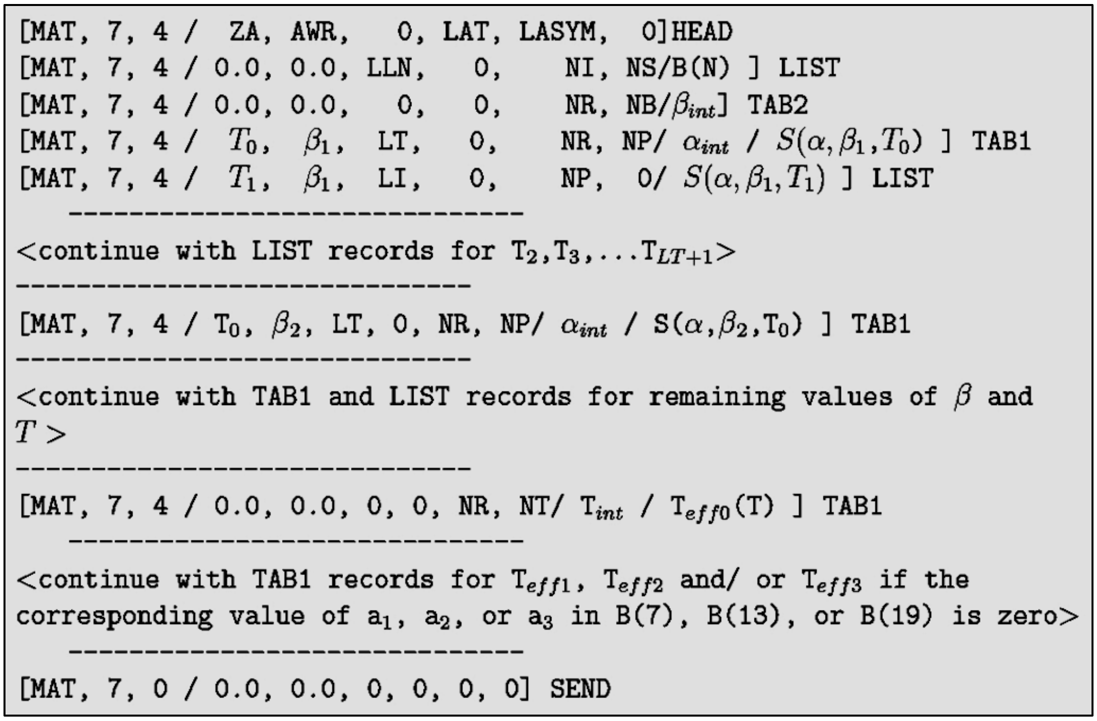

```
[MAT, 7, 4 /  ZA, AWR,   0, LAT, LASYM,   0]HEAD
[MAT, 7, 4 / 0.0, 0.0, LLN,   0,    NI, NS/B(N) ] LIST
[MAT, 7, 4 / 0.0, 0.0,   0,   0,    NR, NB/$\beta_{int}$] TAB2
[MAT, 7, 4 /  $T_0$,  $\beta_1$,  LT,   0,    NR, NP/ $\alpha_{int}$ / $S(\alpha,\beta_1,T_0)$ ] TAB1
[MAT, 7, 4 /  $T_1$,  $\beta_1$,  LI,   0,    NP,  0/ $S(\alpha,\beta_1,T_1)$ ] LIST
    ------------------------------
<continue with LIST records for $T_2$,$T_3$,...$T_{LT+1}$>
------------------------------
[MAT, 7, 4 / $T_0$, $\beta_2$, LT, 0, NR, NP/ $\alpha_{int}$ / S($\alpha$,$\beta_2$,$T_0$) ] TAB1
------------------------------
<continue with TAB1 and LIST records for remaining values of $\beta$ and
$T$ >
------------------------------
[MAT, 7, 4 / 0.0, 0.0, 0, 0, NR, NT/ $T_{int}$ / $T_{eff0}$(T) ] TAB1
    ------------------------------
<continue with TAB1 records for $T_{eff1}$, $T_{eff2}$ and/ or $T_{eff3}$ if the
corresponding value of $a_1$, $a_2$, or $a_3$ in B(7), B(13), or B(19) is zero>
    ------------------------------
[MAT, 7, 0 / 0.0, 0.0, 0, 0, 0, 0] SEND
```

**Figure A.2 Format structure for ENDF File 7, MT = 4, from the ENDF-6 Formats Manual [1].**

The specific structure of the ENDF File 7, MT = 4 format is given in Figure A.2 [1]. Note that the actual printing of lines in the library begins *after* the leftmost slash marks and then cycles back. Selected entries are identified. See Ref. [1] for a full description.

In traditional ENDF evaluations, ZA depends on the atomic number. For File 7, ZA is arbitrary and will typically be assigned the value ZA = 100 + MAT. The quantity AWR is the nuclide to neutron mass ratio for the nuclide that the calculated $S_{\mathrm{sym}}(\alpha,\beta)$ is referenced to. Note that even when $S_{\mathrm{sym}}(\alpha,\beta)$ is calculated for an entire stoichiometric unit, the thermal scattering law must be normalized to one specific nuclide to allow the library to be used in conjunction with traditional ENDF evaluations. The entries NP and NB indicate the number of points in the $\alpha$ and $\beta$ grids, respectively. For each $\beta$, $S_{\text{sym}}(\alpha,\beta)$ is tabulated for every specified temperature sequentially. For the first temperature, the pair $[\alpha,\ S_{\text{sym}}(\alpha,\beta)]$ is tabulated sequentially for each $\alpha$ point. For the LT following temperatures, $S_{\text{sym}}(\alpha,\beta)$ alone is tabulated sequentially for each $\alpha$ point. This process is then repeated for all $\beta$. The first few lines of the published ENDF/B-VII.1 File 7, MT = 4 section for graphite are displayed in Figure A.3 as an example [21]. The locations of important entries are shown. In this example, NP = 72, NB = 96 and LT = 9. Therefore, there will be NP × NB × $(\text{LT} + 1) = 69120$ entries for $S_{\text{sym}}(\alpha,\beta)$ in the File 7 library.

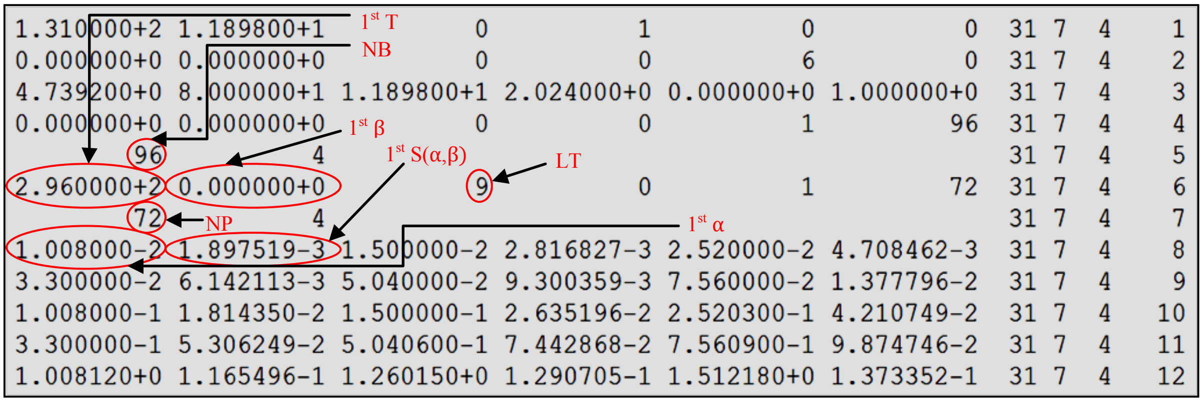

```
1.310000+2 1.189800+1          0          1          0          0 31 7  4    1
0.000000+0 0.000000+0          0          0          6          0 31 7  4    2
4.739200+0 8.000000+1 1.189800+1 2.024000+0 0.000000+0 1.000000+0 31 7  4    3
0.000000+0 0.000000+0          0          0          1         96 31 7  4    4
        96          4                                             31 7  4    5
2.960000+2 0.000000+0          9          0          1         72 31 7  4    6
        72          4                                             31 7  4    7
1.008000-2 1.897519-3 1.500000-2 2.816827-3 2.520000-2 4.708462-3 31 7  4    8
3.300000-2 6.142113-3 5.040000-2 9.300359-3 7.560000-2 1.377796-2 31 7  4    9
1.008000-1 1.814350-2 1.500000-1 2.635196-2 2.520300-1 4.210749-2 31 7  4   10
3.300000-1 5.306249-2 5.040600-1 7.442868-2 7.560900-1 9.874746-2 31 7  4   11
1.008120+0 1.165496-1 1.260150+0 1.290705-1 1.512180+0 1.373352-1 31 7  4   12
```

**Figure A.3 First 12 lines of ENDF/B-VII.1 File 7, MT = 4 section for graphite with arrows indicating the locations of the 1st T, LT, 1st $\boldsymbol{\beta}$, NB, 1st $\boldsymbol{\alpha}$, NP, and the 1st $\boldsymbol{S(\alpha,\beta)}$ entries [21].**

# Appendix B

## The ${}^1\boldsymbol{S}_{\mathbf{s}}(\boldsymbol{Q},\boldsymbol{\omega}) \rightarrow \boldsymbol{S}_{\mathbf{1}}(\boldsymbol{\alpha},\boldsymbol{\beta})$ Expression Transformation

Beginning with the given expression for ${}^1S_s(Q,\omega)$ from Eq. (2.11),

$$ {}^1S_s(Q,\omega) = \frac{e^{-2W}Q^2\rho(\omega)\left[\coth\left(\frac{\hbar|\omega|}{2k_BT}\right)\pm 1\right]}{4M|\omega|}, \tag{B.1}$$

the absolute value signs may be dropped to yield the equivalent expression

$$ {}^1S_s(Q,\omega) = \frac{e^{-2W}Q^2\rho(\omega)\left[\coth\left(\frac{\hbar\omega}{2k_BT}\right)+1\right]}{4M\omega}. \tag{B.2}$$

The ± is eliminated since the sign of both the denominator and the coth argument can now change. A dimensionless momentum transfer factor $\alpha$ can be defined in terms of $Q^2$. With

$$\alpha = \frac{\hbar^2Q^2}{2Mk_BT}, \tag{B.3}$$

Eq. (B.2) is rewritten as

$$ {}^1S_s(\alpha,\omega) = \frac{\alpha k_BTe^{-2W}\rho(\omega)\left[\coth\left(\frac{\hbar\omega}{2k_BT}\right)+1\right]}{2\omega\hbar^2}. \tag{B.4}$$

Applying Eq. (B.3) to Eq. (2.12) yields

$$2W = \frac{\alpha k_BT}{\hbar}\int_0^\infty \frac{\coth\left(\frac{\hbar\omega}{2k_BT}\right)\rho(\omega)}{\omega}d\omega. \tag{B.5}$$

For clarity, the coth expression is expanded to its exponential form to give

$$ {}^1S_s(\alpha,\omega) = \frac{\alpha k_BTe^{-2W}\rho(\omega)\left[\frac{\exp\left(\frac{\hbar\omega}{k_BT}\right)+1}{\exp\left(\frac{\hbar\omega}{k_BT}\right)-1}+1\right]}{2\omega\hbar^2} = \frac{\alpha k_BTe^{-2W}\rho(\omega)\left[\frac{\exp\left(\frac{\hbar\omega}{k_BT}\right)+1}{\exp\left(\frac{\hbar\omega}{k_BT}\right)-1}+\frac{\exp\left(\frac{\hbar\omega}{k_BT}\right)-1}{\exp\left(\frac{\hbar\omega}{k_BT}\right)-1}\right]}{2\omega\hbar^2} = $$
$$\frac{\alpha k_BTe^{-2W}\rho(\omega)\left[\frac{2\exp\left(\frac{\hbar\omega}{k_BT}\right)}{\exp\left(\frac{\hbar\omega}{k_BT}\right)-1}\right]}{2\omega\hbar^2} \tag{B.6}$$

and

$$2W = \frac{\alpha k_{\mathrm{B}} T}{\hbar} \int_0^{\infty} \frac{\left[\frac{\exp\left(\frac{\hbar\omega}{k_{\mathrm{B}}T}\right)+1}{\exp\left(\frac{\hbar\omega}{k_{\mathrm{B}}T}\right)-1}\right]\rho(\omega)}{\omega} d\omega. \tag{B.7}$$

Substituting $\omega = \frac{-\beta k_{\mathrm{B}} T}{\hbar}$ in Eqs. (B.6) and (B.7), where

$$\beta = \frac{E' - E}{k_{\mathrm{B}} T} \tag{B.8}$$

is a dimensionless energy transfer factor, and defining

$$S_1(\alpha, \beta) = k_{\mathrm{B}} T \times {}^{1}S_{\mathrm{s}}(Q, \omega) \tag{B.9}$$

results in the expressions

$$S_1(\alpha, \beta) = \frac{-\alpha k_{\mathrm{B}} T e^{-2W} \rho\left(\frac{-\beta k_{\mathrm{B}} T}{\hbar}\right)\left(\frac{2\, e^{-\beta}}{e^{-\beta} - 1}\right)}{2\beta\hbar} \tag{B.10}$$

and

$$2W = \frac{-\alpha k_{\mathrm{B}} T}{\hbar} \int_{-\infty}^{0} \frac{\left(\frac{e^{-\beta}+1}{e^{-\beta}-1}\right)\rho\left(\frac{-\beta k_{\mathrm{B}} T}{\hbar}\right)}{\beta} d\beta. \tag{B.11}$$

Applying

$$\rho\left(\frac{-\beta k_{\mathrm{B}} T}{\hbar}\right) = \frac{\hbar}{k_{\mathrm{B}} T} \rho(-\beta) \tag{B.12}$$

and the even property of $\rho(\beta)$, plus modifying the limits of integration in Eq. (B.11), $S_1(\alpha, \beta)$ and $\lambda$ can be reformulated as

$$S_1(\alpha, \beta) = \frac{-\alpha e^{-\alpha\lambda} \rho(\beta)\left(\frac{2\, e^{-\beta}}{e^{-\beta} - 1}\right)}{2\beta} = \frac{\alpha e^{-\alpha\lambda} \rho(\beta)}{2\beta\left(\frac{1 - e^{-\beta}}{2e^{-\beta}}\right)} = \frac{\alpha e^{-\alpha\lambda} e^{-\beta/2} \rho(\beta)}{2\beta\left(\frac{1 - e^{-\beta}}{2e^{-\beta/2}}\right)} = \frac{\alpha e^{-\alpha\lambda} e^{-\beta/2} \rho(\beta)}{2\beta \sinh(\beta/2)} \tag{B.13}$$

and

$$\lambda = \frac{2W}{\alpha} = \int_0^\infty \frac{\left(\frac{e^\beta+1}{e^\beta-1}\right)\rho(\beta)}{\beta} d\beta. \tag{B.14}$$

From Eq. (B.14), $\frac{e^\beta+1}{\beta(e^\beta-1)} = \frac{e^\beta}{\beta(e^\beta-1)} + \frac{1}{\beta(e^\beta-1)} = \frac{e^\beta}{\beta(e^\beta-1)} + \frac{e^{-\beta}}{\beta(1-e^{-\beta})} = \frac{e^\beta}{\beta(e^\beta-1)} + \frac{e^{-\beta}}{-\beta(e^{-\beta}-1)}$. Therefore, it is clear that by extending the limits of integration, Eq. (B.14) can be equivalently written as

$$\lambda = \int_{-\infty}^{\infty} \frac{\left(\frac{e^{-\beta}}{e^{-\beta}-1}\right)\rho(\beta)}{-\beta} d\beta = \int_{-\infty}^{\infty} \frac{\left(\frac{2e^{-\beta}}{1-e^{-\beta}}\right)\rho(\beta)}{2\beta} d\beta =$$

$$\int_{-\infty}^{\infty} \frac{e^{-\beta/2}\rho(\beta)}{2\beta\left(\frac{1-e^{-\beta}}{2e^{-\beta/2}}\right)} d\beta = \int_{-\infty}^{\infty} \frac{e^{-\beta/2}\rho(\beta)}{2\beta \sinh(\beta/2)} d\beta. \tag{B.15}$$

The final results of Eqs. (B.13) and (B.15) give the LEAPR form of $S_1(\alpha,\beta)$ and $\lambda$, respectively. The LEAPR form of $\alpha$ can be derived by the following argument, where $\mu$ is the scattering angle cosine in the laboratory frame and $m$ is the mass of a neutron.

$$Q^2 = |\boldsymbol{k} - \boldsymbol{k}'|^2 \;\; => \tag{B.16}$$

$$Q^2 = (k - \mu k')^2 + \left(k'\sqrt{1-\mu^2}\right)^2 \;\; => \tag{B.17}$$

$$Q^2 = \left(\frac{\sqrt{2mE}}{\hbar} - \mu\frac{\sqrt{2mE'}}{\hbar}\right)^2 + \left(\frac{\sqrt{2mE'}}{\hbar}\sqrt{1-\mu^2}\right)^2 \;\; => \tag{B.18}$$

$$Q^2 = \frac{2m}{\hbar^2}\left(E + E' - 2\sqrt{EE'}\mu\right). \tag{B.19}$$

Now, applying Eq. (B.3) to Eq. (B.19) and defining $A$ as the nuclide to neutron mass ratio,

$$\alpha = \frac{E' + E - 2\mu\sqrt{EE'}}{A k_{\mathrm{B}} T}. \tag{B.20}$$

See Refs. [15, 20] for additional details.

# Appendix C

## Analytical Solution for the Covariance Matrix of $\boldsymbol{S}_{\text{sym},1}(\boldsymbol{\alpha}, \boldsymbol{\beta})$

First, Eq. (2.14) is restated in terms of $S_{\text{sym},1}(\alpha, \beta)$, or

$$S_{\text{sym},1}(\alpha, \beta) = \frac{\alpha\, e^{-\alpha\lambda} \rho(\beta)}{2\beta \sinh(\beta/2)}. \tag{C.1}$$

Now,

$$S_{\text{sym},1}(\alpha, \beta) = f_1(\alpha) g_{\text{sym},1}(\beta) = f_1(\alpha) h(\beta) \rho(\beta). \tag{C.2}$$

Here, $f_1(\alpha) = \alpha\, e^{-\alpha\lambda}$ and

$$h(\beta) = \frac{1}{2\beta \sinh(\beta/2)}. \tag{C.3}$$

The column vectors $\boldsymbol{p}$, $\boldsymbol{h}$ and $\boldsymbol{W}_a$ are defined as

$$\boldsymbol{p} = (k_{\text{B}}T)^{-1} \rho(\beta_d),\ \text{for } d = 1 \dots D, \tag{C.4}$$

$$\boldsymbol{h} = h(\beta_b),\ \text{for } b = 1 \dots B, \tag{C.5}$$

and

$$\boldsymbol{W}_a = S_{\text{sym},1}(\alpha_a\,, \beta_b),\ \text{for } b = 1 \dots B. \tag{C.6}$$

For $d = 1 \dots D$, $d$ corresponds to the energy grid points of the phonon DOS. For $a = 1 \dots A$ and $b = 1 \dots B$, $a$ and $b$ correspond to $\alpha$ and $\beta$ grid points, respectively, in $S_{\text{sym},1}(\alpha, \beta)$. The parameter $b$ is also considered to correspond to the energy grid point $\beta_b k_{\text{B}} T$. The vector $\boldsymbol{p}$ defines the phonon DOS. It is in vector space $R$, and $R$ has dimension $D$ with standard basis $\boldsymbol{R}$. The vectors $\boldsymbol{h}$ and $\boldsymbol{W}_a$ are in vector space $U$, and $U$ has dimension $B$ with standard basis $\boldsymbol{U}$. Now, $\boldsymbol{W}_a$ can be written as

$$\boldsymbol{W}_a = \boldsymbol{h} \circ [\boldsymbol{T}(a)\boldsymbol{p}], \tag{C.7}$$

where

$$\boldsymbol{T}(a) = k_{\mathrm{B}} T f_1(\alpha_a)\boldsymbol{I},\ \text{if } D = B \text{ and } E(d) = E(b) \text{ for all } d = b, \tag{C.8}$$

or

$$\boldsymbol{T}(a) = k_{\mathrm{B}} T f_1(\alpha_a)\boldsymbol{L},\ \text{if } D \neq B \text{ and/or } E(d) \neq E(b) \text{ for any } d = b. \tag{C.9}$$

The notation ∘ represents the Hadamard product. $\boldsymbol{T}(a)$ is a linear transformation matrix given by either Eq. (C.8) or (C.9). Under the condition given in Eq. (C.8), $\boldsymbol{I}$ is the $D \times D$ identity matrix. Under the condition given in Eq. (C.9), $\boldsymbol{L}$ is a non-diagonal interpolation matrix of dimension $B \times D$. The matrix $\boldsymbol{L}$ will have either one or two non-zero entries in each row depending on the discrete distribution of $E(d)$ and $E(b)$. The columns of $\boldsymbol{T}(a)$ represent the linear transformation of the $d^{\text{th}}$ vector of $\boldsymbol{R}$, for $d = 1 \ldots D$, in terms of each of the $B$ vectors in $\boldsymbol{U}$. Thus, any vector in $R$ may be mapped by $\boldsymbol{T}(a)$ to a vector in $U$. The following is a basic example of the linear mapping process:

Example

Given: $E(b) = \{0.05, 0.1, 0.2, 0.4, 0.8\}, E(d) = \{0.0, 0.2, 0.4, 0.6, 0.8, 1.0\}$

$$\boldsymbol{T}(a) = k_{\mathrm{B}} T f_1(\alpha_a)\boldsymbol{L} = k_{\mathrm{B}} T f_1(\alpha_a) \begin{bmatrix} 3/4 & 1/4 & 0 & 0 & 0 & 0 \\ 1/2 & 1/2 & 0 & 0 & 0 & 0 \\ 0 & 1 & 0 & 0 & 0 & 0 \\ 0 & 0 & 1 & 0 & 0 & 0 \\ 0 & 0 & 0 & 0 & 1 & 0 \end{bmatrix}.$$

$$\text{Therefore, } \boldsymbol{W}_a = k_{\mathrm{B}} T f_1(\alpha_a)\boldsymbol{h} \circ \begin{bmatrix} 3/4 & 1/4 & 0 & 0 & 0 & 0 \\ 1/2 & 1/2 & 0 & 0 & 0 & 0 \\ 0 & 1 & 0 & 0 & 0 & 0 \\ 0 & 0 & 1 & 0 & 0 & 0 \\ 0 & 0 & 0 & 0 & 1 & 0 \end{bmatrix} \boldsymbol{p}.$$

Let $\boldsymbol{W}$ and $\boldsymbol{H}$ be the column vectors with dimension $AB$ that are constructed by successively appending $\boldsymbol{W}_a$ and $\boldsymbol{h}$, respectively, for $a = 1 \dots A$. Let $\boldsymbol{T}$ be the matrix with dimension $AB \times D$ that is constructed by successively appending the matrices $\boldsymbol{T}(a)$ for $a = 1 \dots A$. This results in

$$\boldsymbol{W} = \boldsymbol{H} \circ [\boldsymbol{Tp}], \tag{C.10}$$

and it is clear that $\boldsymbol{M_{pW}} = \boldsymbol{M_{ps_1}}$ will have the form

$$(\boldsymbol{M_{pW}})_{ij} = H_j \boldsymbol{T}_j \boldsymbol{p}_i = f_{ij}, \text{ for } i = 1 \dots D \text{ and } j = 1 \dots AB. \tag{C.11}$$

In Eq. (C.11), $\boldsymbol{T}_j$ is the $j^{th}$ *row* vector of $\boldsymbol{T}$, and $\boldsymbol{p}_i$ is the *column* vector given by substituting $p_d = 0$ for all $d \neq i$ in $\boldsymbol{p}$. The index $j$ is associated with a particular $(a, b)$ pair. Hence, $\boldsymbol{M_{pW}}$ has the same dimensions ($D \times AB$) and entry definitions as $\boldsymbol{M_{ps}}$, except $\boldsymbol{M_{pW}}$ is analytically solved for one-phonon scattering while $\boldsymbol{M_{ps}}$ must be numerically solved for the full scattering law. The elements in $\boldsymbol{V_W} = \boldsymbol{M}_{\boldsymbol{pW}}^{\mathrm{T}} \boldsymbol{V_p} \boldsymbol{M_{pW}} = \boldsymbol{V_{s_1}}$ can now be expressed as

$$\mathrm{COV}(\boldsymbol{W}_k, \boldsymbol{W}_l) = \textstyle\sum_{q,r} f_{qk} f_{rl} \mathrm{COV}(p_q, p_r), q = 1 \dots D, r = 1 \dots D. \tag{C.12}$$

In Eq. (C.12), $q$ and $r$ are indices that increment the rows and columns of $\boldsymbol{V_p}$ to calculate the covariance associated with the $k^{\text{th}}$ and $l^{\text{th}}$ elements of the column vector $\boldsymbol{W}$. Note that the units are consistent, where $\boldsymbol{V_{s_1}}$ is unitless, $\boldsymbol{M_{pW}}$ and $\boldsymbol{M}_{\boldsymbol{pW}}^{\mathrm{T}}$ (or $\boldsymbol{M_{ps_1}}$ and $\boldsymbol{M}_{\boldsymbol{ps_1}}^{\mathrm{T}}$) have units of $k_{\mathrm{B}}T$ and $\boldsymbol{V_p}$ has units of $(k_{\mathrm{B}}T)^{-2}$.

In the one-phonon analytical calculation it has been assumed that $\lambda$ in the Debye-Waller factor is independent of the individual parameters $p_d$. While this is not strictly true, $\lambda$ is highly insensitive to any perturbation of a single $p_d$. A straightforward approach to account for the dependence of $\lambda$ on the individual parameters $p_d$ is to treat $\lambda$ as a parameter itself, along with all $p_d$. In this case, $\lambda$ may be included in the covariance matrix $\boldsymbol{V_p}$ which is calculated by the Monte Carlo process. To add the appropriate terms to the sensitivity matrix $\boldsymbol{M_{pW}}$, note that

$$\frac{\partial S_{\mathrm{sym},1}(\alpha_a,\beta_b)}{\partial\lambda} = -\alpha_a \lambda H_j \boldsymbol{T}_j \boldsymbol{p}. \tag{C.13}$$

Linear mapping of the phonon DOS to the one-phonon scattering law allows for a simple analytic formulation of $\boldsymbol{M_{ps_1}}$ and, consequently, for $\boldsymbol{V_{s_1}}$ in terms of $\boldsymbol{M_{ps_1}}$ and a given $\boldsymbol{V_p}$. For higher-order phonon processes, direct linear mapping is not possible. Alternatively for the one-phonon case, $\boldsymbol{V_W} = \boldsymbol{V_{s_1}}$ may be calculated through the Monte Carlo generation of a large set of $\widetilde{\boldsymbol{W}}$ vectors. Since $\boldsymbol{W}$ is nearly linearly proportional to the parameters $p_d$ (with $\lambda$ being a very limited source of nonlinearity), the results for $\boldsymbol{V_W}$ may be quite similar using the two methods of calculation, although nonlinearities in the functional dependence among the $p_d$ could have some effect. However, the point of the above analytical procedure is to be able to express each term of $\sigma(\boldsymbol{s}_1)$ in the context of at most two $\sigma(p_d)$ values as an aid in assessing the specific uncertainties in a $\rho(\varepsilon)$ spectrum calculated from $S_1(\alpha,\beta)$ extracted from experimental measurements.

# Appendix D

## A Review of the VASP and PHONON Code Methodologies for Modeling the Graphite System

### D.1 Density Functional Theory

Density functional theory (DFT) is a quantum mechanical simulation methodology for describing the electronic structure of periodic crystal systems. In particular, DFT is used to calculate the ground state of a many-bodied system by minimizing the total energy functional $E[n(\boldsymbol{r})]$ with respect to the electron density function $n(\boldsymbol{r})$. The ground state is equivalent to relaxing the system to its 0 K state.

The graphite system is defined in the *ab initio* DFT code VASP [47, 48, 49] by supplying the crystal structure parameters and symmetry. The total energy functional is defined as

$$E[n(\boldsymbol{r})] = T[n(\boldsymbol{r})] + R[n(\boldsymbol{r})] + V[n(\boldsymbol{r})] + X[n(\boldsymbol{r})], \tag{D.1}$$

and it is calculated using an electron plane-wave basis set with a specified electron cutoff energy. In this work, an energy cutoff of 800 eV in VASP is used to relax the graphite system. The electronic kinetic energy is given by $T[n(\boldsymbol{r})]$, which is calculated for a non-interacting homogeneous electron gas of density $n(\boldsymbol{r})$. The electron-electron Coulomb repulsion term is given by $R[n(\boldsymbol{r})]$. The external potential term is given by $V[n(\boldsymbol{r})]$ and is calculated with native VASP pseudopotentials. These pseudopotentials account for nuclei and core (non-valence) electrons in the system. The final $X[n(\boldsymbol{r})]$ term is the exchange-correlation energy. It is the result of non-classical interactions between identical particles (i.e., electrons). The local density approximation (LDA) is used to calculate $X[n(\boldsymbol{r})]$ and was found to produce much more accurate results for the relaxed lattice constants of graphite than the generalized gradient approximation (GGA). Since Van der Waals forces arise from long-range correlated polarizations of atoms, they are not included in the total energy functional of VASP [62].

The total energy functional is solved by integrating over points in reciprocal space. A $k$-mesh represents the resolution of a grid of $k$-points in reciprocal space with respect to crystallographic directions. An 11 × 11 × 5 $k$-mesh with automatically generated $k$-points was found to yield good convergence in minimizing the total energy per unit cell. The equilibrium lattice constants calculated after relaxing the system without constraints were $a = 2.45$ Å and $c = 6.59$ Å. From Baskin and Meyer [55], the $c$ lattice constant for graphite at 4.2 K was experimentally measured to be 6.67 Å, while no statistically significant change in the $a$ lattice constant from 2.46 Å at 297 K was detectable upon cooling. The slightly inaccurate calculation of the relaxed lattice constant $c$ by VASP may be related to the absence of Van der Waals forces. Noting that the relaxed $c/a$ ratio also differs somewhat from the experimental ratio, the constraint can be imposed in VASP that the unit cell $c/a$ ratio remains fixed to the experimental ratio. This has been demonstrated to give better agreement with experimentally measured dispersion relations and elastic properties for graphite [17, 54]. In this case, the total energy functional is minimized with lattice constants of $a = b = 2.45$ Å and $c = 6.64$ Å. This represents a reduction from the 300 K lattice constants of about 0.6% in-plane and 1.0% out-of-plane.

## D.2 Lattice Dynamics and the Dynamical Matrix

Once the lowest-energy equilibrium state of the graphite system has been determined by VASP, this serves as a reference structure for the determination of interatomic forces. These forces are employed in a lattice dynamics model in the harmonic approximation to calculate the phonon density of states by solving a dynamical matrix. Starting with a relaxed system is a requirement for solving the dynamical matrix in the harmonic approximation since anharmonicities in the interatomic forces are assumed to be zero.

Interatomic Hellmann-Feynman forces are calculated in VASP by individually perturbing the basis set of atoms from their equilibrium positions with respect to each coordinate axis and then taking the first derivative of the ground-state potential function. A perturbation of 0.055 Å was determined to be appropriate. A 6 × 6 × 1 supercell (containing 144 carbon atoms) with a 3 × 3 × 4 $k$-mesh and 500 eV plane-wave cutoff energy were determined to provide good convergence in capturing the interatomic forces of the graphite system [17]. Assuming the potential is harmonic for small perturbations, the harmonic force constants (FCs) are extracted from the Hellmann-Feynman forces by PHONON to yield a force constant matrix $\boldsymbol{\Phi}_{u\eta,v\chi}$ associated with each pair of atoms $\eta$ and $\chi$, where $\eta$ is a particular basis set carbon atom and $\chi$ can be any other carbon atom in the supercell. For the indices $u$ and $v$, values of 1, 2 or 3 correspond to perturbations in the direction of the Cartesian vectors $\hat{\boldsymbol{x}}$, $\hat{\boldsymbol{y}}$ or $\hat{\boldsymbol{z}}$. For each $\eta$, an extended supercell is defined which relocates $\eta$ to the center of the supercell such that force constants are calculated with respect to all symmetric neighbors of each coordination shell residing in the supercell. Therefore, for each $(\eta, \chi)$ pair, there are six non-degenerate FCs.

In the harmonic approximation, the equations of motion for a basis atom $\eta$ in the crystal are described by

$$\omega^2(\boldsymbol{q})\boldsymbol{e}(\boldsymbol{q}) = \boldsymbol{D}_{\eta,uv}(\boldsymbol{q})\boldsymbol{e}(\boldsymbol{q}), \tag{D.2}$$

where

$$\boldsymbol{D}_{\eta,uv}(\boldsymbol{q}) = \sum_{\chi} \frac{1}{\sqrt{M_\eta M_\chi}} \boldsymbol{\Phi}_{u\eta,v\chi} e^{i\boldsymbol{q}\cdot[\boldsymbol{r}(\chi)-\boldsymbol{r}(\boldsymbol{\eta})]} \tag{D.3}$$

is known as the dynamical matrix [18, 39]. Essentially, the dynamical matrix describes the motion of each basis atom as if it were attached by springs to every other atom in the supercell. Larger force constants allow for higher-frequency phonons and smaller force constants influence the population of lower-frequency phonons. The polarization vectors $\boldsymbol{e}_j$ and the Cartesian vectors are usually held to be synonymous. Atomic vibrations in the $\hat{\boldsymbol{x}}$ direction can be considered to be associated with $j = 1$, atomic vibrations in the $\hat{\boldsymbol{y}}$ direction with $j = 2$, and atomic vibrations in the $\hat{\boldsymbol{z}}$ direction with $j = 3$. Eq. (D.2) can be solved by diagonalizing the matrix $\boldsymbol{D}_{\eta,uv}(\boldsymbol{q}) - \omega^2(\boldsymbol{q})\boldsymbol{I}$, where $\boldsymbol{I}$ is the identity matrix, since

$$\det\left[\boldsymbol{D}_{\eta,uv}(\boldsymbol{q}) - \omega^2(\boldsymbol{q})\boldsymbol{I}\right] = 0. \tag{D.4}$$

The phonon frequencies are the square roots of the eigenvalues and there are $3H$ eigenvalues associated with each $\boldsymbol{q}$, where $H$ is the number of atoms in the unit cell basis. There will also be a corresponding eigenvector (or polarization vector) for each eigenvalue (or frequency) of $\boldsymbol{q}$. Consequently, there are $3H$ branches of the $\omega(\boldsymbol{q})$ dispersion relations. Of these, three are acoustic branches where all basis atoms vibrate in phase, and the remainder are optical branches representing the different possible out-of-phase vibrations among the basis atoms. There are twelve dispersion branches for graphite, though many of these are degenerate, or nearly degenerate, due to the layered structure of graphite.

The dispersion relations for any single $\boldsymbol{q}$ vector corresponding to any basis atom $\eta$ may be solved using the dynamical matrix. Through Monte Carlo sampling of phonon wave vectors in the first Brillouin zone, PHONON produces the unnormalized partial phonon DOS $\rho(\omega)$ for each coordinate vector and for every basis position. Sampling within the first Brillouin zone captures all of the physics of the crystal. A user-specified number of $\boldsymbol{q}$-points are randomly generated and, for each trial, the twelve associated phonon frequencies and polarization vectors are determined. The results are collected, separated by coordinate vector and basis position, and placed in frequency bins of user-defined resolution. This methodology is detailed in Ref. [17] and in Ref. [18].

In some cases, the calculated phonon frequencies will include a narrow band of negative frequencies. These are non-physical and can arise for several reasons. Some examples are that the optimization (relaxation) process for computing the system ground state may not have been carried out with sufficient accuracy, localized anharmonicities may be present in the potential function, or atomic perturbations from the equilibrium state may be too small (yielding poor numerics for the $k$-mesh) or too large (introducing excessive anharmonicities). As long as these imaginary frequencies collectively make up a negligible fraction of the phonon DOS, they may be safely truncated. In the reference total phonon DOS calculated in this work, given in Section 4.3.1, imaginary frequencies are associated with less than 0.04% of the phonon population. In cases where the imaginary frequencies are significant, there may be serious problems with the simulation process or the system may be thermodynamically unstable.

A flowchart summarizing the procedures used to calculate the reference total phonon density of states $\rho(\varepsilon)$ in this work is given in Figure D.1.

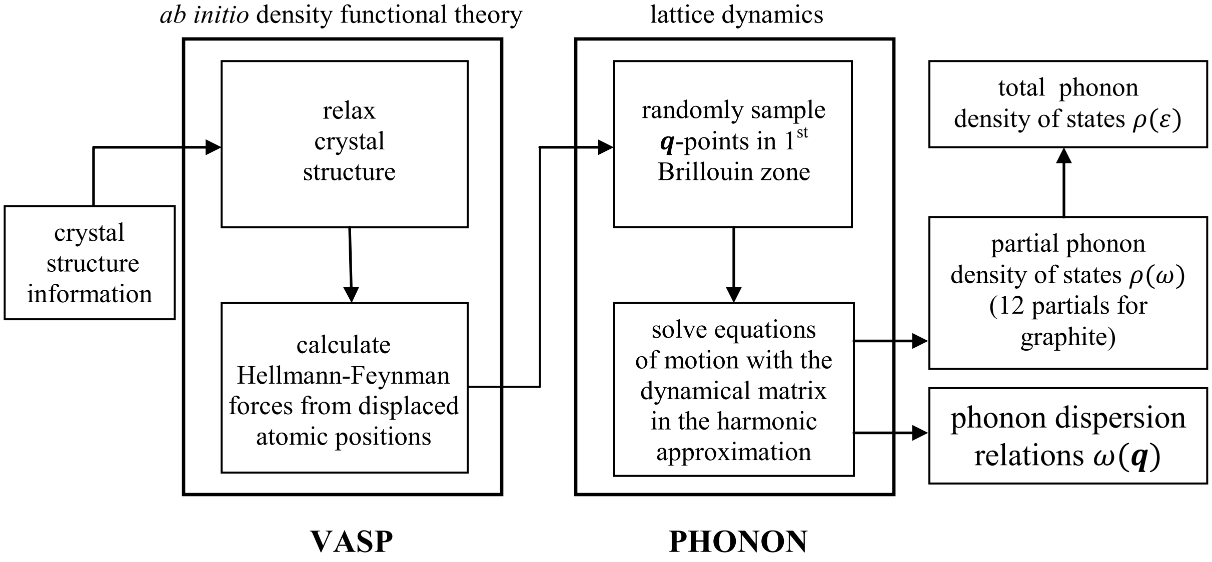

**Figure D.1 Flowchart demonstrating the sequence of calculation procedures employed in generating the reference total phonon density of states $\boldsymbol{\rho(\varepsilon)}$.**